TABLE OF CONTENTS

SECTION A

CHAPTER 1

INTRODUCTION

CHAPTER 2

EXPERIMENTAL

SECTION B

CHAPTER 3

RESULTS AND DISCUSSION

SPECTROSCOPIC , MICROSCOPIC AND ELECTROCHEMICAL PROPERTIES OF IRON-PHTHALOCYANINE SINGLE-WALLED CARBON NANOTUBE BASED ELECTRODES

CHAPTER 4

ELECTROCATALYTIC PROPERTIES OF IRON-PHTHALOCYANINE-SWCNT BASED ELECTRODES:THIOCYANATE AS A MODEL ANALYTE

CHAPTER 5

MICROSCOPIC AND ELECTROCHEMICAL PROPERTIES OF FERROCENE SINGLE-WALLED CARBON NANOTUBES BASED ELECTRODES

CHAPTER 6

ELECTROCATALYTIC PROPERTIES OF FERROCENE SINGLE-WALLED CARBON NANOTUBES BASED ELECTRODES: THIOCYANATE AS A MODEL ANALYTE

ABBREVIATIONS

A	Electrode surface area (cm^2)
AFM	Atomic force microscopy
Ag	Silver wire pseudo-reference electrode
AglAgCl	Silver/silver chloride reference electrode
CME	Chemically modified electrode
C.E.	Counter electrode
CMEs	Chemically modified electrodes
CV	Cyclic voltammetry
Cys	Cysteamine
CV	Cyclic voltammogram
D	Diffusion coefficient (cm^2s^{-1})
DCC	Dicyclohexylcarbodiimide
DMF	Dimethylformamide
EIS	Electrochemical impedance spectroscopy
E_p	Peak potential
E_{pa}	Anodic peak potential
E_{pc}	Cathodic peak potential
E^o	Standard potential
$E^{o'}$ or $E_{1/2}$	Formal redox potential
F	Faraday’s constant
FeOHETPc	Iron-octahydroxyethylthiophthalocyanine

$Fe(CN)_6^{4-}$	Hexacyanoferrate(II)
$Fe(CN)_6^{3-}$	Hexacyanoferrate(III)
i_{for}	Forward current
i_{rev}	Reverse current
I_{pa}	Anodic peak current
I_{pc}	Cathodic peak current
ITO	Indium tin oxide
LoD	Limit of detection
MPc	Metallophthalocyanine
MPc-SAM	Metallophthalocyanine-self assembled monolayer
Pc	Phthalocyanine
R	Gas constant
R.E.	Reference electrode
R_s	Solution resistance
SAM	Self-assembled monolayer
SEM	Scanning electron microscopy
SWCNTs	Single-walled carbon nanotubes
SWV	Square wave voltammetry
T	Temperature (K)
t	Time(s)
W.E.	Working electrode
XPS	X-ray photoelectron spectroscopy

LIST OF SYMBOLS

α	Transfer coefficient
ω	Angular velocity
ε	Extinction coefficient
Γ	Surface coverage or concentration
π	Pi bonding
λ	Wavelength
γ	kinematic viscosity
C	Molar concentration of analyte
c	Speed of light
C	Capacitance
C_{dl}	Double-layer capacitance
CPE	Constant phase electrode
C_m	Monolayer capacitance
C_{ox}	Concentration of the oxidised form of an analyte
C_{red}	Concentration of the reduced form of an analyte
D	Diameter
D	Diffusion coefficient
E_{pa}	Anodic peak potential
E_{pc}	Cathodic peak potential
E	Potential
E^o	Standard potential

$E_{1/2}$	Half-wave potential
ΔE_{p}	Anodic-to-cathodic peak potential separation
f	Frequency
F	Faraday’s constant
h	Plank’s constant
Hz	Hertz
i_{pa}	Anodic peak current
i_{pc}	Cathodic peak current
k	Heterogeneous electron transfer coefficient
k_{et}	Electron transfter rate constant
k_{f}	Rate of forward reaction
k_{r}	Rate of reverse/backward reaction
k_{obs}	Observed rate constant
K	Kelvin
K	Equilibrium constant
K_{a}	Dissociation constant
K_{aap}	Electron transfer rate constant
n	Number of electron
$\mathrm{N_A}$	Avogadro’s constant
q	Electrical charge
Q	Electrical charge (C)
r	Radius of electrode

R	Universal gas constant
R_{ct}	Charge transfer resistance
R_s	Resistance of electrolyte
Sub	Substrate
$Sub_{(ox)}$	Oxidised substrate
v	Scan rate
V	Volts
Z_{im}	Imaginary impedance
Z_{re}	Real impedance
Z_w	Warburg impedance

LIST OF FIGURES

LIST OF SCHEMES

LIST OF TABLES

SECTION A

CHAPTER 1

INTRODUCTION

1.1. General Overview of Thesis: Problem Statement

1.1.1. Self-assembly in electrode fabrication

Self-assembly is simply the term used to describe a spontaneous organization process of molecular units into ordered structures on metallic surfaces. The interaction responsible for the formation of the self-assembled system acts directly on the nanostructure architecture. Self-assembly can be classified as either static or dynamic. However, there are three distinctive features that make self-assembly a distinct concept, namely order, interactions and building blocks. Self-assembled monolayer (SAM) modified electrodes represent a modern approach to electrode systems. Presently, self-assembly technique is used to modify electrodes by anchoring inorganic or organic entities onto the electrode surface.

These electrodes rely on the placement of a molecular reagent onto the surface, to impart the behavior of that reagent to the modified surface. Such deliberate alteration of electrode surface can thus meet the needs of many electroanalytical problems and may form the basis for new analytical applications and different sensing devices. SAM technique has a number of advantages over other monolayer formation techniques which include simplicity, reproducibility and formation of highly ordered and stable monolayer which are chemically bound onto solid surface. The use of SAM for the fabrication of electrodes with redox-active materials such as SWCNT and phthalocyanine is hugely unexplored.

1.1.2. Carbon nanotubes as electron-conducting nanowires

Since the re-discovery of carbon nanotubes in 1991 by Iijima [1], following the original discovery by Wiles and Abrahamson in 1978 [2], carbon nanotubes (CNT) have become an increasingly important group of nanomaterials with unique properties such as geometry, electronic, mechanical and chemical properties. Over the years, new discoveries have led to new applications, often taking advantage of these unique properties in different fields such as nanotechnology, electronics, optics and material science.

CNTs were first applied in electrochemical sensing in 1996 by Britto and co-workers [3], and since then research on their potential applications in electrochemistry has continued to grow in leaps and bounds. These potential applications in electrochemistry are made possible by the high electrochemically accessible surface area of porous nanotube arrays, combined with their high electronic conductivity and useful mechanical properties. Carbon nanotubes display metallic, semiconductive and superconducting electron transport, thus provide direct electrical communication between the underlying electrode and the redox active species with no need for redox mediators [4,5]. Despite the excellent physico-chemical properties of CNTs, their immobilization onto electrode surfaces via SAM is hugely unexplored. Carbon nanotubes were used in this project as electron-conducting nanowires to enhance the electrochemical performance of organo-iron electrocatalyst (iron containing complexes).

1.1.3. Metallophthalocyanines as electrocatalysts

Metallophthalocyanines (MPcs) are metal N4-macrocyclic organometallic complexes that have found applications in a plethora of area. Most of the applications of MPc complexes arise from their diverse chemical, structural, electronic and optical properties. This is mainly because of their chemical stability [6].

Electroanalytical characterization of MPc and transition metal phthalocyanine (MPc) complexes has been an area of intense research. These complexes are well known robust and versatile electrocatalysts for the reduction and oxidation of a number of molecules of biological, biomedical clinical, pharmaceutical, industrial and environmental importance [6]. Their electrocatalytic activity lies in their ability to easily bind one or two axial ligands, especially analytes and undergo either metal-centered, ring-centered or axial ligand-centered redox reactions [6-11]. Research has revealed that chemically modified electrode improves catalytic current necessary for sensitive detection of target analytes. As a result, the MPc based modified electrodes have exhibited enhanced sensitivity and selectivity of analytes [12]. Thus, this thesis focuses on the applications of modified electrodes fabricated with MPc, notably iron(II)Pc (FePc) complexes as well as ferrocenes. The co-intergration of MPc and CNTs as electrode modifiers is rarely reported and the electron transport is almost unknown.

1.1.4. Carboxylated ferrocenes as electrocatalysts

Ferrocene (Fc) is a coordination compound which falls under the supramolecular chemistry and its applications permitted their fast and spontaneous incorporation to nanosystems [13]. Building coordination compound on solid surfaces has made the preparation of nanoscaled devices with new properties possible. Ferrocene-terminated self-assembled monolayers are redox-active two dimensional aggregates on metal surfaces. These SAMs have been used as convenient, robust and well-reproducible surface self-assemblies for the kinetic and thermodynamic studies of electron transfer [14,15] and the influence of the redox environment on electron transfer kinetics [16,17]. Gooding *et al*. [18] have measured the electrochemical characteristics of ferrocenemethylamine modified single-walled carbon nanotubes immobilized to a self-assembled monolayer of mercaptoethylamine on gold electrode. However, the co-assembling of SWCNTs and ferrocenes are not known. This work also examines for the first time the electrochemical and electrocatalytic properties of mixed SAMs of SWCNTs and Fcs.

1.1.5. Aim of thesis

Self-assembled monolayer (SAM) technique is well recognized as an efficient electrode fabrication strategy for forming stable, well-organised, ultrathin films of thiol-derived molecular species. Stable immobilization of redox-active materials, such as carbon nanotubes, transition metallophthalocyanines and ferrocenes, as ultrathin films on solid substrate is important for the development of several technological devices such as sensors, electronic device, catalyst, etc.

The development of chemical sensors is currently one of the most active areas of analytical research. Electrochemical sensors represent an important subclass of chemical sensors in which an electrode is used as the transduction element. Such device hold a leading position among sensors presently available, have reached a commercial stage (i.e screen printed electrodes) Despite the excellent physico-electrochemical properties of carbon nanotubes, metallophthalocyanines and ferrocenes in the literature, their immobilization onto electrodes via SAM process is virtually unknown.

The main objectives of this project therefore are:

(a) To integrate the redox-active species (i.e., carbon nanotubes, iron-phthalocyanines and ferrocenes) as ultrathin films on electrodes using SAM technique.

(b) Interrogate the integrity of such CNT-FePc or CNT/Fc hybrid in terms of:

  (i) Heterogeneous electron transfer dynamics, and

  (ii) Electrocatalysis of biologically and environmentally important analytes (thiocyanate).

In this introductory chapter, I will give a general overview of electrochemistry, electrochemical techniques, electrode modification processes, carbon nanotubes, phthalocyanine complexes, ferrocene complexes, analytes (thiocyanate and epinephrine) used in this work as analytical probes. Chapter two provides the procedures adopted for the experiments. Finally, chapters three to six will discuss the results obtained.

1.2. **Overview *of Electrochemistry***

1.2.1. Basic concepts

Electrochemistry is the branch of chemistry that studies the interplay between chemical reactions and electricity. The fundamental process in electrochemical reactions is the transfer of electrons between the electrode surface and molecules in the interfacial region, either in solution or immobilized at the electrode surface. Therefore, electrochemistry is one effective technique to study electron transfer properties. When electron transfer is between a solid substrate and a solution species, it is termed heterogeneous process. Inversely, if electron transfer reaction occurs between two species, both of which are in solution, the reaction is homogeneous.

Electrochemistry involves the measurement of potential (potentiometry) or current response (voltammetry) [19]. The work described in this thesis involves current measurement, voltammetry and a number of voltammetric techniques, namely, cyclic voltammetry (CV), square wave voltammetry (SWV), chronoamperometry (CA) and linear sweep voltammetry (LSV).

1.2.2. The electrode-solution interface

Charged particles exist at every material interface called the *electrical double layer*. In electrochemistry, this layer reflects the ionic zones formed in the solution to compensate for the excess of charge on the electrode. The model produced by stern [20] which describes double layer is made up of several layers, when the electrode is immersed in solution as illustrated in figure1.1. Whether the charge on the metal is negative or positive with respect to the solution depends on the potential across the interface and the composition of the solution. A positively charged electrode thus attracts a layer of negative ions and vice versa. The inner layer closest to the electrode contains solvent molecules that are specifically adsorbed on the electrode. This layer is called the *Inner Helmholtz Plane* (IHP) or *compact layer* [21]. The outer layer called the *Outer Helmholtz Plane* (OHP) is the imaginary plane passing through the solvated cations. These planes cannot be measured nor do they exist so it can be assumed that the distance from the electrode to the IHP indicated as x_1 will be the radius of the ion and the solvated ions can approach the metal only at a distance x_2. The layer which extends from the OHP into the bulk solution is a three dimensional region of scattered ions called the diffuse or Gouy layer.

The IHP and OHP represent the layer of charges which is strongly held by the electrode and can survive even when the electrode is pulled out of the solution [21,22].

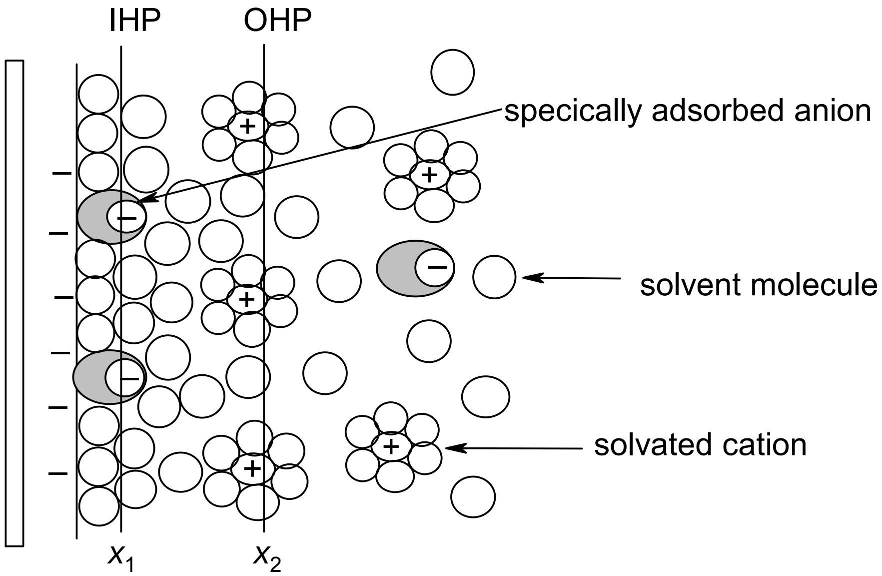

Figure 1.1: Model of the electrode-solution double layer regions in a case of a negatively charged electrode.

1.2.3. Faradaic and Non-Faradaic process

Oxidation and reduction processes are governed by Faraday's law which states that the amount of chemical reaction caused by the flow of current is proportional to the amount of electricity passed.

These reactions are called Faradaic processes as electrons are transferred across the metal-solution interface. Non-Faradaic process arise when an electrode-solution interface shows a range of potentials where no charge-transfer reactions occur. However, processes such as adsorption and desorption can occur, and the structure of the electrode-solution interface can change with changing potential or solution composition. Although charge does not cross the interface, external currents can flow (at least transiently) when the potential, electrode area, or solution composition changes.

1.2.4. Mass transport processes

Mass transport is a process which governs the movement of charged or neutral species and contributes to the flow of electricity through an electrolyte solution in an electrochemical cell. This movement is considered as mass transfer of an electroactive species near the electrode by using a supporting electrolyte and operating in a quiescent solution. **Migration**, **diffusion** and **convection** are the three possible mass transport processes accompanying an electrode reaction.

(a) Migration

Migration is the type of charge transport that is related to the movement of ions and the existence of potential gradient between two electrodes in solution [23]. Controlled-potential experiments require a supporting electrolyte to decrease the resistance of a solution and eliminate electromigration effects to maintain a constant ionic strength. To eliminate or suppress electromigration, addition of excess or large concentration of inert salt such as KCl is used in this work. In analytical applications, the presence of a high concentration of supporting electrolyte which is hundred times higher than the concentration of electroactive ions means that the contribution of examined ions to the migrational transport is less than one percent. Then it can be assumed that the transport of the examined species towards the working electrode is by diffusion only. Migration of electroactive species can either enhance or diminish the current flowing at the electrode during reduction or oxidation of cations. It helps reduce the electrical field by increasing the solution conductivity, and serves to decrease or eliminate sample matrix effects. The supporting electrolyte ensures that the double layer remains thin with respect to the diffusion layer, and it establishes a uniform ionic strength throughout the solution. However, measuring the current under mixed migration-diffusion conditions may be an advantage in particular electrochemical and electroanalytical situations [24].

(b) Diffusion

Diffusion is the transport of particles as a result of local difference in the chemical potential [25]. Diffusion is simply the movement of material from a high concentration region of the solution to a low concentration region. If the potential at an electrode oxidizes or reduces the analyte, its concentration at the electrode surface will be lowered, and therefore, more analyte moves to the electrode from the bulk of the solution, which makes it the main current-limiting factor in voltammetric process.

Although migration carries the current in the bulk solution during electrolysis, diffusion should also be considered because, as the reagent is consumed or the product is formed at the electrode, concentration gradient between the vicinity of the electrodes and the electroactive species arise. Indeed, under some circumstances, the flux of electroactive species to the electrode is due almost completely to diffusion.

(c) Convection

Convection is one of the modes of mass transport which involves the movement of the whole solution carrying the charged particles. Forced convection, which can also occur, may be unintentional and occurs as a result of vibrating building but usually, stirring is applied to enhance the rate of mass transport process [26]. Stirring can be achieved by stirring the solution with the help of a separate stirrer or most conveniently, the use of rotating disk electrode is used for the purpose of convection. In voltammetry, convection is eliminated by maintaining the cell under quiet and stable condition.

1.3. Voltammetric techniques

As already stated, voltammetry alone was employed in this project, namely, Cyclic voltammetry (CV), Square wave voltammetry (SWV), Chronoamperometry (CA) and linear sweep voltammetry (LSV). This section gives the basic theoretical background underlying these techniques.

1.3.1. Cyclic voltammetry

Cyclic voltammetry (CV) is often the first experiment performed in an electroanalytical study, particularly due to its ability to rapidly provide considerable information on the thermodynamics of redox processes and the kinetics of heterogeneous electron transfer reactions. It offers a rapid location of redox potentials of the electroactive species and convenient evaluation of the effect of electrolyte on the redox process. There are three cyclic voltammetric processes that could take place, namely, reversible, irreversible and quasi-reversible.

1.3.1.1 Reversible process

The amount of the oxidized species at the electrode surface become reduced by the reduction process and replaced by the reduced species, which diffuses away into the solution. If we reverse the potential sweep process from the positive side, the reverse effect is observed. As the potential sweeps reverses back towards the redox potential, then the reduced species will start to be re-oxidized. The current will then increase in the negative direction until an oxidation peak is reach. Figure 1.2 indicates the resulting scan of potential against time, scanning linearly the potential of a stationary working electrode in an unstirred solution, using a triangular potential waveform. The potentiostat measures current resulting from the applied potential.

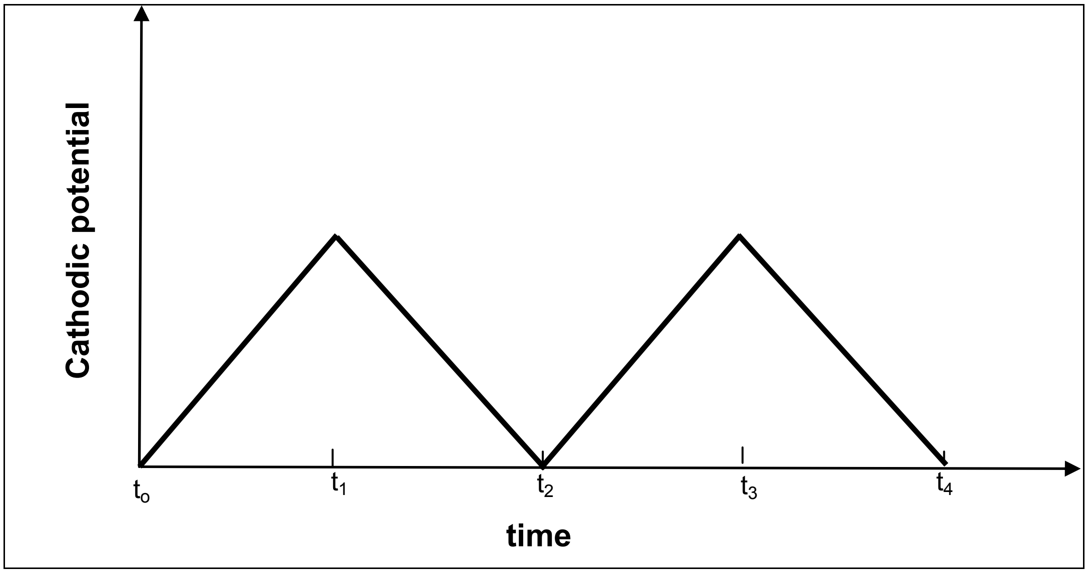

Figure 1.2: The potential waveform applied to W.E in the cyclic voltammetry experiment.

The potentiostat is controlled by a computer which enables one to analyze the current-potential plot called cyclic voltammogram. The expected cyclic voltammogram of a reversible redox couple for a single potential cycle is illustrated in Figure 1.3.

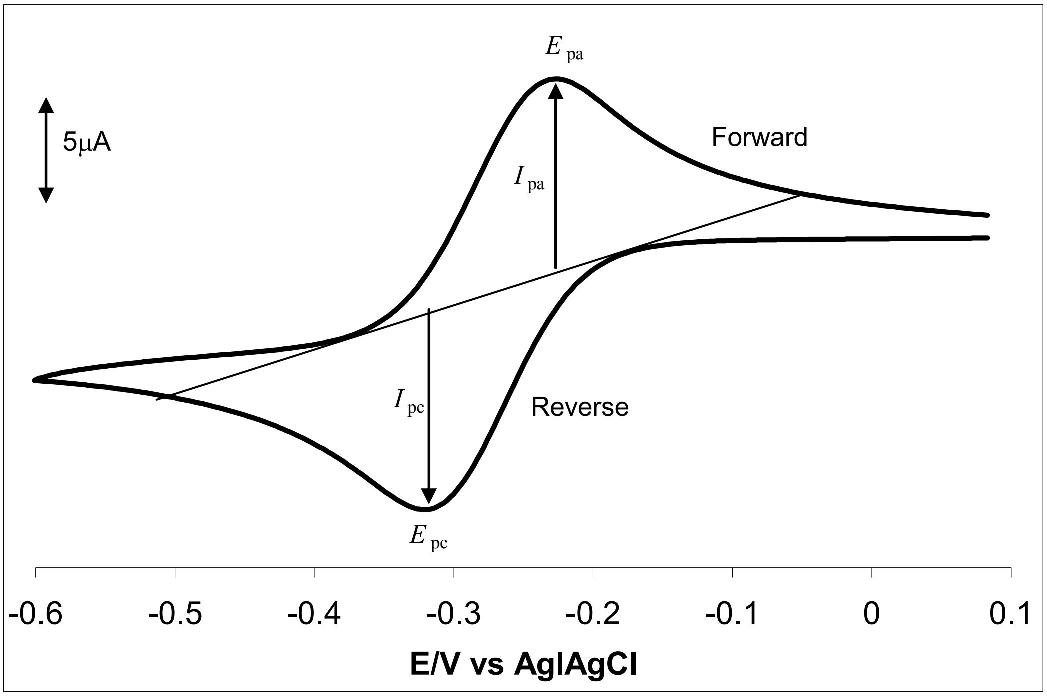

Figure 1.3: Typical cyclic voltammogram for a reversible redox process.

Closer look at figure 1.3, it is assumed that only the oxidized form (analyte or electrolyte) is initially present, therefore a potential scan in the negative direction is chosen for the first half-cycle, starting from a point where no reduction occurs. As the applied potential approaches E^o, the standard potential, for a redox process, a cathodic current begins to increase until a peak reaches maximum. The potential at which the peak current occurs is known as the peak potential, E_p. At this potential, the redox species has been depleted at the electrode surface and the current is diffusion limited. After potential region in which the reduction process takes place, the direction of the potential scan is reversed. During this scan, the R molecules generated in the forward half-cycle and accumulated near the surface, are reoxidized back to O, resulting in the anodic peak. The magnitude of the Faradaic current, called the anodic peak current, I_{pa}, or cathodic peak current, I_{pc}, is indicative of rate of electron transfer between the electrode and the redox species. The electrical signal is related to the recognition process and is proportional to the concentration of the analyte. To clearly simplify the direction undertaken by the electron, Bard and Faulkner [24] explained that by driving the electrode to negative potentials, the energy of the electrons is raised high enough to transfer into the vacant electronic state on species in the electrolyte i.e the reduction current, thus a flow of electrons from electrode to solution occurs. Similarly, by imposing a more positive potential, the energy of the electrons is lowered and electrons in the electrolyte will transfer to the electrode i.e oxidation current. The flow of the electrons to and from the electrode surface is governed by mass transport.

For a reversible process, the Nernst equation is obeyed in which the electron transfer is fast, allowing the assumption that the concentration of both the oxidized, O and reduced, R species are in a state of equilibrium, equation 1.1.

$$O + ne^{-} \leftrightarrows R \tag{1.1}$$

The electroactive species are stable thus the magnitude of the reverse-to-forward peak current ratio is unity for a simple reversible couple. The peak-to-peak separation (ΔE_p) should be independent of the scan rate, v, but in practice it slightly increase with v, this is due to the solution resistance, R_s, between the reference and working electrode [27]. The peak current, I_p of a reversible process is given by the Randles-Sevčik equation 1.2 [24]:

$$I_p = (2.69 \ x \ 10^{5}) \, n^{3/2} A \, D^{1/2} C \, v^{1/2} \tag{1.2}$$

where n is the number of electrons, A the area of the electrode in cm^2, C the concentration in $mol.cm^{-3}$, D the diffusion coefficient in cm^2s^{-1} and v the potential scan rate in Vs^{-1}. The current I_p, is directly proportional to concentration of the analyte [5] and increases with the square root of the scan rate. The dependence of current on the scan rate is indicative of electrode reaction controlled by diffusion [28-30], using equation 1.2 a linear plot of I_p vs. $\nu^{1/2}$ is obtained. Deviation from linearity indicates the presence of chemical reaction involving either the oxidized, reduced or both species.

For a reversible process, the half-wave potential, $E_{1/2}$, equals the formal potential $E^{o'}$ and are related to the standard potential (E^{o}) as in equation 1.3:

$$E_{1/2} = E^{o'} = E^{o} + \frac{RT}{2nF}\ln\frac{[O]}{[R]} \qquad (1.3)$$

where R is the gas constant, T the temperature in Kelvin, F the Faraday's constant and [**O**] is the concentration of oxidised species, [**R**] is the concentration of reduced species in mol l^{-1}, respectively. The formal redox potential, $E^{o'}$ can be calculated from equation 1.4:

$$E_{1/2} \text{ or } E^{o'} = \frac{E_{pa} + E_{pc}}{2} \qquad (1.4)$$

where E_{pa} is the anodic peak potential and E_{pc} is the cathodic peak potential. The number of electrons transferred in a reversible process can be calculated from equation 1.5:

$$\Delta E = E_{pc} - E_{pa} = \frac{RT}{nF}, \text{ at } 25^{0}\text{C}$$

$$\Delta E = \frac{0.059\ V}{n} \qquad (1.5)$$

where n is the number of electrons transferred, other symbols have their usual meaning. The peak-to-peak separation is approximately 59 mV at 298 K and is independent of scan rate.

1.3.1.2 *Irreversible process*

Totally irreversible processes usually are due to slow electron exchange or slow chemical reaction at the electrode surface [31]. These processes are characterized by a shift of the peak potential with the scan rate and ΔE can be calculated from equation 1.6:

$$\Delta E = E^o - \frac{RT}{\alpha n_a F}\left[0.78 - \ln\frac{k^o}{D^{1/2}} + \ln\left(\frac{\alpha n_a F v}{RT}\right)^{1/2}\right] \qquad (1.6)$$

where α is the rate of electron transfer and n_a is the number of electrons involved in the charge transfer step and k^o is the heterogeneous electron transfer coefficient in cms^{-1}. The other symbols are listed in the list of symbols. At 25°C, the peak potential and the half-peak potential differ by 0.048 Vαn. Hence, the voltammogram becomes more drawn-out as αn decreases. In an irreversible process, only forward for oxidation or reverse reduction peak is observed, see Figure 1.4. It is common to observe a weak reverse peak at increased scan rates during forward oxidation at times, because of sluggish electron exchange as mentioned above. The

Nernst equation is not applicable in the case of irreversible process. This is due to the rate of electron transfer insufficient to maintain surface equilibrium and thus the oxidized and reduced species are not at equilibrium.

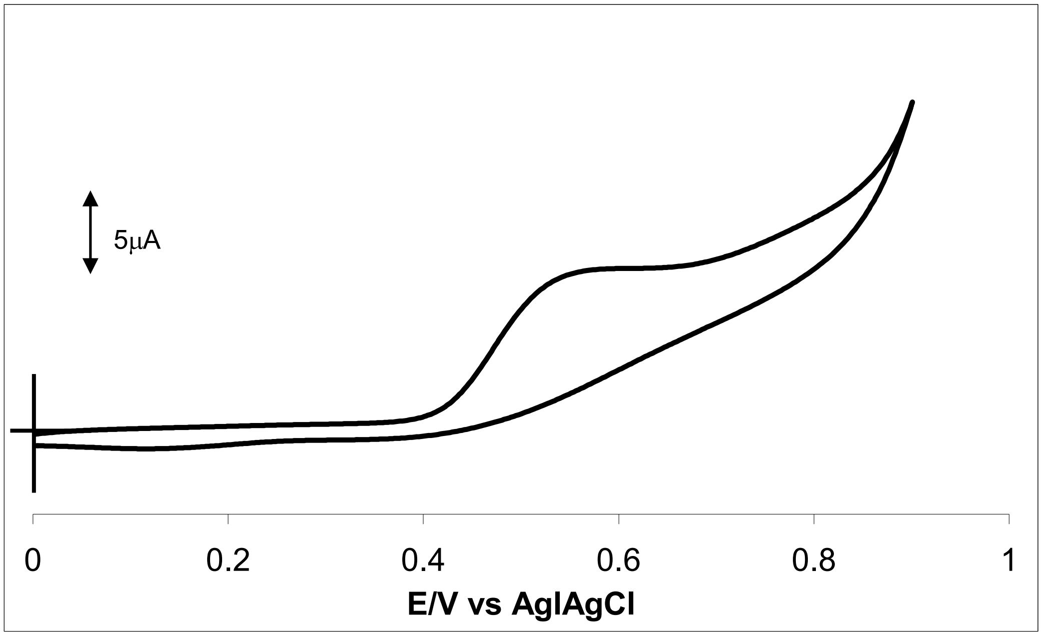

Figure 1.4: Typical cyclic voltammogram for an irreversible process.

The peak current, I_p for an irreversible process can be calculated from equation 1.7:

$$I_p = \left(2.99x10^5\right) n\left[\left(1-\alpha\right)n\right]^{1/2} ACD^{1/2} v^{1/2} \qquad (1.7)$$

The peak current is proportional to the bulk concentration but is lowered in height by the value of α, which is assumed to be 0.5.

Overall the cyclic voltammetric set up consist of the working electrode (W.E.), a counter electrode (C.E.) and a reference electrode (R.E.) immersed in a quiescent solution. The solution is kept stationary to avoid movement of ions to the electrode by mechanical means.

1.3.1.3 Quasi-reversible process

Mass transport plays a major role in controlling the concentration of the redox couple and the expressions for reversible processes also apply for quasi-reversible processes. The voltammograms of a quasi-reversible process exhibit a large peak-to-peak separation compared to reversible processes. The peak current increase with $v^{1/2}$ but is not linear and ΔE is greater than 0.0059/n V. In reversible process, current is controlled purely by mass transport but in quasi-reversible process, current is controlled by both the mass transport and charge transfer kinetics [31,32]. Table 1.1 summarizes the slight differences in cyclic voltammetric processes.

Table 1.1: The diagnostic criteria for reversible, irreversible and quasi-reversible cyclic voltammetric processes [24,28,33].

Parameters	Cyclic Voltammetry Process		
	Reversible	Irreversible	Quasi-reversible
E_p	Independent of v	Shift cathodically by 30/αn mV for 10-fold increase in V	shift with v
E_{pc} - E_{pa}	≈ 59/n mV at 25^0C and independent of v	_	May approach 60/n mV at low v but increase as v increases
$\frac{i_p}{v^{1/2}}$	Constant	Constant	Virtually independent of v
$\frac{i_{pa}}{i_{pc}}$	Equals 1and independent of v	no current on the reverse side	Equals 1 only for α = 0.5

1.3.2. Square wave voltammetry

Square wave voltammetry (SWV) is a further improvement of staircase voltammetry, which is itself a derivative of linear sweep voltammetry. In linear sweep voltammetry the current at a working electrode is measured while the potential between the working electrode and the reference electrode is swept linearly with time.

Oxidation or reduction of species is recorded as a peak or trough in the current signal at the potential window. The potential waveform composed of a symmetrical square wave of constant amplitude is superimposed on a base potential staircase sweep [34,35] as illustrated in figure 1.5. The current is measured at the end of each wave just prior to potential change. The differential current is then plotted as a function of potential.

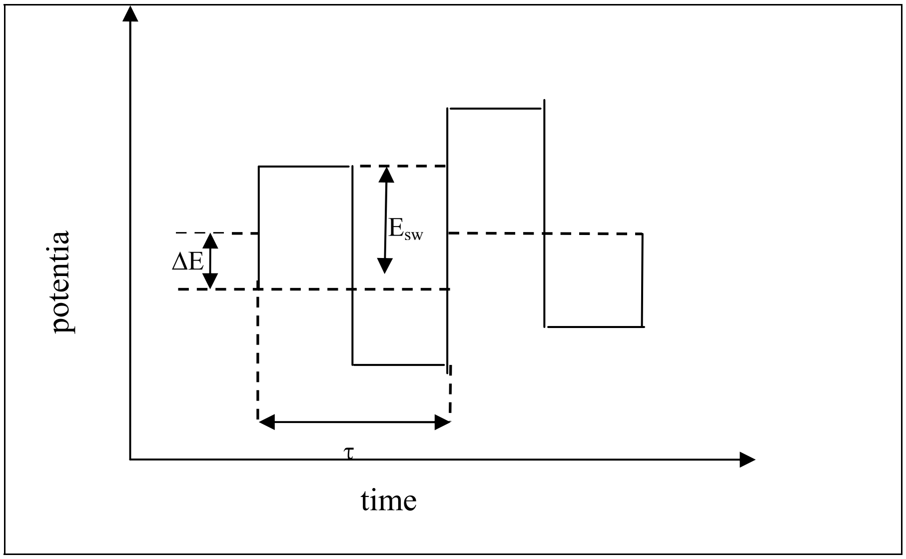

Figure 1.5: Square wave waveform potential sweep.

The excitation signal in SWV consists of a symmetrical square wave pulse of amplitude E_{sw} superimposed on a staircase waveform of step height ΔE, where the forward pulse of the square wave coincides with the staircase step. The net current, i_{net}, is obtained by taking the difference between the forward and reverse currents ($i_{for} - i_{rev}$) and is centered on the redox potential. This speed, coupled with computer control and signal averaging, allows for experiments to be performed repetitively and increases the signal-to-noise ratio.

In this technique, a peak is a square wave which occurs at the $E_{1/2}$ of the redox couple because the current function is symmetrical around that potential [36,37]. Square wave voltammetry has several advantages, among these are its speed and excellent sensitivity partly because of its ability to discriminate against charging current [38-39] or to separate a capacitive current from a so called pseudocapacitance [40]. The peak height is directly proportional to the concentration of the electroactive species and direct detection limit as low as 10^{-8} mol.L^{-1} is possible. This technique includes the use of faster scan rates compared to conventional differential pulse voltammetry. Applications of square-wave voltammetry include the study of electrode kinetics with regard to catalytic homogeneous chemical reactions, determination of some species at trace levels. In this research, a computer-controlled square wave voltammetry was employed.

1.3.3. Chronoamperometry

Chronoamperometry belongs to the family of step techniques [41-44], which is a potential-controlled technique where the basis is the measure of current response to an applied potential as a function of time. If the potential is stepped from E_1, where no current flows (i.e., the oxidation or reduction of the electrochemically active species does not take place) to E_2 where the current belongs to the electrode reaction, is limited by diffusion. The current flows at any time after the application of the potential step, (figure 1.6(a)). As with all step techniques, this one however, generates high charging currents which decay exponentially with time. It is most commonly investigated with a three electrode system. The resulting current-time dependence is monitored (figure 1.6(b)).

The current-time curve reflects the change in the concentration gradient in the vicinity of the surface which involves gradual expansion of the diffusion layer associated with the depletion of the reactant, thus the slope of the concentration profile decreases as time progresses. Accordingly, the current decays with time as given by the Cottrell equation, (equation 1.8).

$$I = \frac{nFAD^{1/2}C}{\pi^{1/2}t^{1/2}} \qquad (1.8)$$

where n, F, A, D, C, and t are number of electrons, Faraday constant, the surface area of the electrode, the diffusion coefficient, the concentration of analyte and time, respectively.

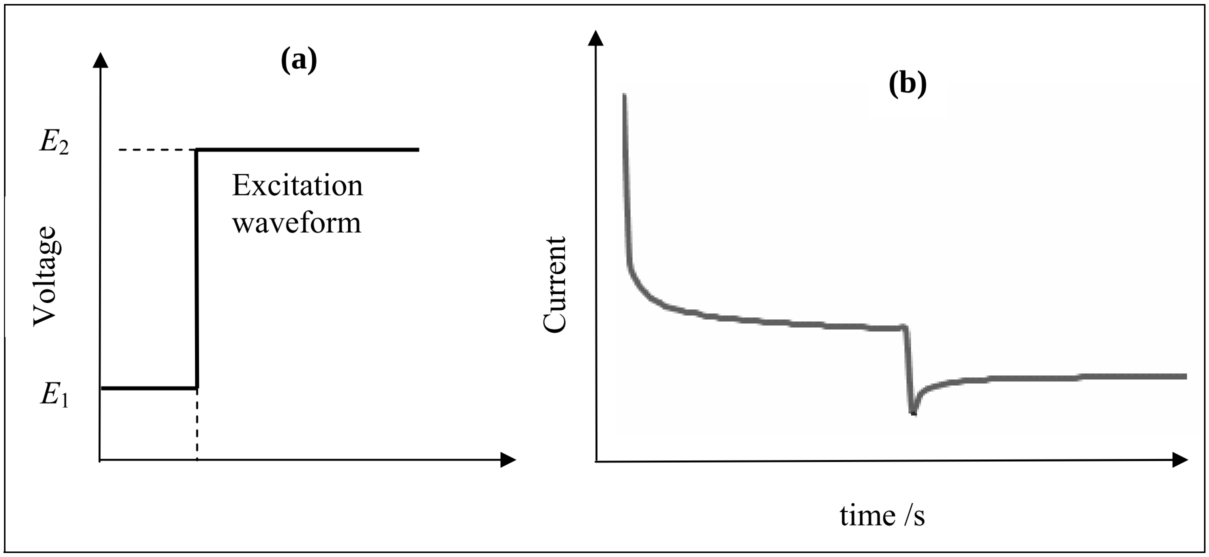

Figure 1.6 (a) Waveform of the potential step and (b) Chronoamperometric response.

1.3.4. Linear sweep voltammetry

Linear sweep voltammetry (LSV) is a method where the electrode potential is varied linearly with time with the scan rate ν = dE/dt and current versus potential is recorded. In LSV essentially only the first half-cycle of a cyclic voltammogram is executed and the rotating disk electrode is used in this experiment.

The rotating disk electrode is rotated in the solution under study and the current depends on the solution flow rate. For the rotating disk electrode, the time dependence is in the rotation rate of the disk, which in turn controls the solution velocity near the electrode. The rate of mass transport at the rotating disk electrode is varied by altering the disk rotation speed [45]. The rotating electrode is mounted vertically to a controllable-speed motor and rotated with constant angular velocity. The components of the fluid velocity depends on this angular velocity of the disk, which is given by $\omega = 2\pi f$, where f is the rotation speed in revolutions per minutes (rpm) or rotation frequency in hertz. It depends on other factors such as the radial distance from the center of the disk (r), the coefficient of kinematic viscosity of the fluid (γ) and on the axial distance from the surface of the disk [46].

The diffusion-limited current at the rotating disk electrode is given by the Levich [47] equation based totally on mass-transfer limited conditions. The disk current I_k in the absence of diffusion control, that is, solely in the case of electron transfer controlled process is given by

$$I_k = FAK(E)C \tag{1.9}$$

with the surface area A of the electrode, the catalytic rate constant k as a function of the electrode potential E and the concentration C. A general equation of the disk current, taking into account both mass transport and electron transfer kinetics can thus be given as the Koutečky-Levich [48] equation:

$$\frac{1}{I} = \frac{1}{I_k} + \frac{1}{I_{\lim}} = \frac{1}{I_k} + \frac{1}{0.62nFAD^{\frac{2}{3}}\omega^{\frac{1}{2}}\gamma^{\frac{1}{6}}} \tag{1.10}$$

where I is the measured current, I_k and I_{lim} are the kinetic and diffusion-limited currents, respectively, n is the number of electrons transferred per molecule, F is the Faraday constant, A is the geometric electrode area, D is the diffusion coefficient ω is the rotation rate in rad.s^{-1}, and γ is the kinematic viscosity of the solution.

1.4. Chemically modified electrodes

A chemically modified electrode (CME) is an electrode surface coated with a thin film of selected conducting materials for the purpose of improving the chemical, electrochemical, optical, electrical and electron transfer properties of the film in a rational, chemically designed manner [49]. The modified electrode can thereby exhibit properties related to those of the modifying substance, e.g., electron-transfer mediation; acceleration or inhibition of electrode reactions; chemical, electrostatic, or steric selectivity; photosensitivity; and so on. Such method of construction which involves incorporating an electroactive substance onto a solid surface such as gold [50], carbon paste matrix [51], glassy carbon [52], pyrolytic graphite electrodes [53] has been applied until recently for a number of purposes such as the determination of trace amounts of some substances [54,55], electrocatalysis [56,57] and electrochemical sensors for the analysis of biologically important compounds [58]. CMEs may contain more than one modifying substance or more than one layer.

1.4.1. Methods of modifying electrode surface

A number of methods have been used to fabricate chemically modified electrodes. Such methods occur as a results of attaching molecules of modifying species by valence forces, covalent bonding, coating by polymer (organic) or inorganic polynuclear, mixed films such as composites, hybrid organic-inorganic, or by mixing the modifier with electrode matrix material [58]. Several types of ring-substituted and unsubstituted MPcs and other organometallic complexes have been employed in the construction of electrochemical sensors using methods which do not require special equipment.

Confinement of these catalysts to the electrode surface is clearly advantageous from economic standpoint and improves the flexibility of the system by providing an option for reagentless sensing, stability and well-defined or sizeable electrochemical responses. Fabrication techniques of electroactive materials on conductive solid substrates that have attracted attention of researchers are described below.

1.4.1.1 Self-Assembly/chemisorption

The formation of self-assembled monolayers (SAMs) has attracted considerable attention since the late 1980s because of its potential use in many scientific and technological applications such as chemical sensors, biosensors and information storage devices [59]. SAMs provides means to controlling the chemical nature of the electrode-solution interface [60].

Spontaneous, chemically adsorbed monolayers of alkanethiols on gold substrate is based on the strong interaction between gold and sulphur which are well suited for controlling and manipulating the reactivity at the interface. The thiol molecules adsorb readily from solution onto the gold, creating a dense monolayer with the tail group pointing outwards from the surface. If the molecule does not contain sulphur, for example carboxylated SWCNT, the use of a different substrate like silicon [61] can be used. One of the simplest ways of forming these ultrathin films is by mere immersion of the noble metal surface in a dilute millimolar solution of organic molecule for a specified time [62]. It is also possible to chemically functionalize the tail groups by performing reactions after assembly of the thiol SAM. The Au-thiolate bond is a strong, homolytic bond strength of 44 kcal/mol [63,64]. These alkanethiols are known to form densely packed crystalline or liquid crystalline material on gold with attractive Van der Waal forces between the alkyl chains that enhances the stability and order of the SAMs. The latter forces add up to strength for alkyl chains and plays an important role in aligning the alkyl chains parallel to each other. Such a self-assembly process results in a well organized and stable monolayers with hydrocarbon tails packed parallel to each other, tilted slightly relative to the substrate. The packing and order of monolayers are influenced by factors such as chain length, head group, solvent, immersion time and substrate morphology.

Research has shown that SAMs formed with longer alkane thiol chain lengths of carbon atom greater than 10, favour a more ordered packing and higher monomer density [59,61]. Electron transfer kinetics is also dependent on the carbon chain length of thiol molecules. Griveau and co-workers [65] reported that electrodes modified with thiols like cysteine, glutathione and 2-mercapoethanol are not stable over long period of time associated with the loss of the catalyst from the surface linked to passivation complications that are endemic to organosulphur compounds. To overcome this problem the use of SAM comes as an advantage where straight alkanethiol chain and macrocyclic complexes such as phthalocyanines or nanomaterials such as carbon nanotubes can be attached and form conductive and stable films.

The structure in Figure 1.7(a) could arise, for example, with an assembly in which the substrate imposes a head-group spacing leading to lower density than a closest packed arrangement. Generally, the greater the mismatch between the van der Waals radii of the tail groups and the head groups and between these quantities and the substrate lattice parameters, the greater the tendency for the monolayer to deviate from well-arranged structures such as in Figures l.7(b) and l.7(c) and to exhibit structural disorder and defects.

In this case, a final structure could arise as a compromise between a tendency for tails to pack parallel to one another and be oriented perpendicular to the surface (in order to maximize interlocking interactions of CH_2 groups in an alkyl chain) and a tendency for the head groups to maintain an open structure for which parallel, tilted tails (i.e figure 1.7(b)) do not pack optimally.

The word SAM, simple mean a monomolecular thin film of organic compound on flat conducting metal. Cyclic voltammetry and impedance spectroscopy are important techniques which provide useful information about redox properties of attached groups, distribution of defects like pinholes, kinetics and mechanism of monolayer formation.

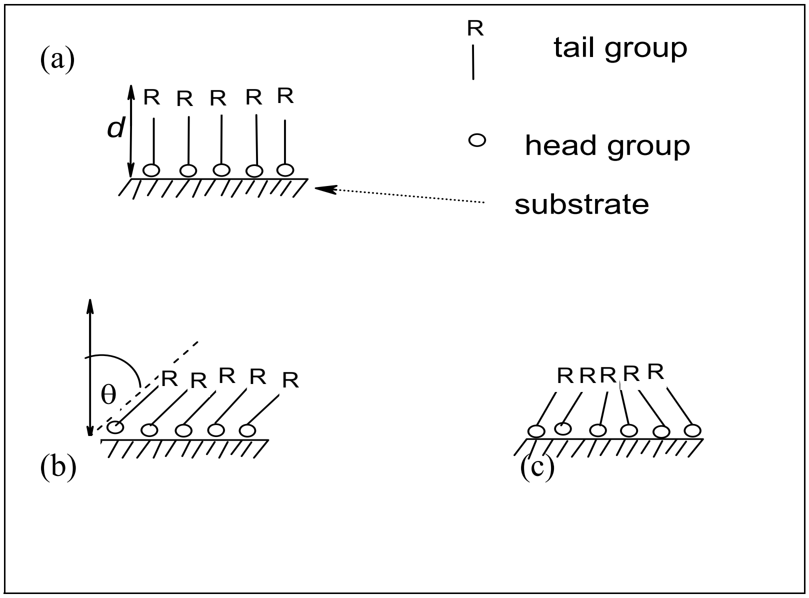

Figure 1.7: Models of an organized monolayer.

The redox activity of the SAM is obtained by using an external redox probe and voltammetry can provide additional information about the mode of surface confinement. One advantage of using SAM modified electrodes is that they are very stable and can form a highly ordered ultrathin films on solid surfaces [66]

Self-assembly can be devided into four main types. *Static*, *dynamic*, *biological* and *templated* self-assembly [67] Systems that are at global equilibrium and do not give off energy, for example molecular crystals [68,69] and globular proteins, are formed by static self-assembly.

Alkanethiol monolayers can also be assembled on gold nanoparticles confined to indium tin oxide. Alternatively, mixing two different hydrocarbons which are carboxyl group terminated in the preparation solution, the mixed SAMs can be prepared. The relative proportion of the two functionalities in the assembled SAM will then depend upon several parameters, like the mixing ratio in solution, the solubilities of the hydrocarbon in the solvent used, and the properties of the terminating groups. The main focus in this work was on the mixture of ferrocenes and carbon nanotubes, since they both contain the same carboxyl functional groups.

Although SAMs are stable in a wide range of potential, the layer is desorbed from the surface at very cathodic potentials [70]. Wang *et* *al*. [71] has reported that carboxylic acid, (COOH) and amine (NH_2) terminated SAMs are used to mimic negatively and positively charged surfaces, respectively.

1.4.1.1.1 Characterization of SAM-modified electrodes

A list of non-electrochemical analytical methods for characterisation of SAM-modified electrodes includes infra red spectroscopy, X-ray photoelectron spectroscopy and scanning probe microscopy. Electrochemical techniques especially, cyclic voltammetry (CV) [72,73], have proven to be effective for SAM characterisation. Other methods can be used for the determination of surface concentration, electron-transfer kinetics, sensitivity and electrode's limit of detection, such as the method used in this work, namely impedance spectroscopy and chronoamperometry.

The surface roughness of gold electrode surface plays a crucial role in determining whether or not the SAMs formed will have pinholes and defects or not. Increase in surface roughness usually increases the chances of having pinholes and defects because it leads to formation of SAMs with poor uniformity [74-77].

It has been reported that an MPc species that is surface confined with flat orientation has a surface coverage concentration of approximately 10^{-10} mol cm^{-2}, free of pinholes and defects. Nirmalya *et* *al*. [78] reported that if a decrease by one order of magnitude in double layer capacitance is observed, confirms SAM formation on the solid surface while lack of redox behaviour indicates surface passivation.

1.4.1.1.2 Application of SAM modified electrodes

Self-assembly technique offers several number of advantages over other film formation techniques. These advantages include spontaneous adsorption to the electrode surface, resulting in thermodynamically equilibrated thin film structures. Despite the popularity of the MPcs as efficient electrocatalysts for analysis of a variety of molecules, their use as electroactive SAMs still remain largely unexplored. However, considerable interest has been placed on SAMs of organothiol on gold surfaces. Analytical application of these SAMs is the fabrication of a number of biosensors and immunosensors [79], enzyme biosensors [80], DNA hybridization biosensors [81] and metal ion sensors [82]. The fundamental application of SAM modified electrodes is used in the study of heterogeneous electron transfer [83,84].

1.4.1.2 Electrodeposition

This is a process used in electroplating in which the current is used to reduce cations of a desired material from a solution and coat a conductive metal with a thin layer of the material. To acquire this, the electrode is immersed in an electrolyte solution containing one or more dissolved salts as well as other ions that permit the flow of electricity, followed by repetitive voltammetric scanning within a specified potential window [85].

1.4.1.3 Drop-dry method

This method involves drop-coating the electrode with small droplets of the desired solution of volatile solvent such as dimethylformamide and then allowed to dry out [87-89]. The films prepared in this way are usually non-uniform. However, the morphology of the film depends on the concentration of the casting solution, rate of solvent evaporation, nature of the solvent and the roughness of the electrode surface.

1.4.1.4. *Dip-dry coating*

Dip-dry coating involves immersion of the electrode in a solution for a period sufficient for spontaneous film formation to occur by adsorption. Then the electrode is withdrawn from the solution and the solvent is allowed to dry out [90,91].

1.4.1.5 *Spin coating*

Spin-coating also known as spin casting is a procedure in which the excess amount of a solution is placed on the substrate and rotated at high speed in order to spread the fluid by centrifugal force. Rotation is continued while the fluid spins off the edges of the substrate, until the desired thickness of the film is achieved. The solvent used is usually volatile and simultaneously evaporates. As a result, the higher the angular speed of spinning, the thinner the film. However, the thickness of the film depends on the concentration of the solution and the solvent. Spin coating is widely used in microfabrication and photolithography and the film may show lower percentage coverage of crystallites than a simple evaporated film [92,93].

1.4.1.6 Vapour deposition

This process is also known as the chemical vapour deposition (CVD). It is used to produce high-purity and high performance thin films. In a typical CVD process the substrate is exposed to one or more volatile precursors which react and decompose on the substrate surface to produce the desired deposit.

1.4.1.7 Langmuir-Blodgett

In 1930, Langmuir and blodgett invented the technique that involves forming an ordered monolayer or multilayer films at the air-water interface and then transfer the film to the electrode surface by immersing the solid substrate into or from the liquid. A monolayer is added with each immersion step thus films with accurate thickness can be formed and can be repeated with several layers, if desired, of different properties [94].

1.4.1.8 Electropolymerisation

In this method the electrode is immersed in an approximately 1 mM concentrated solution of the modifier followed by repetitive voltammetric scanning within a specified potential window. The resulting voltammogram of the first scan is different from the subsequent scans indicative of the formation of the new species on the electrode surface. Li and Guarr [95] reported that very thin films of cobalt and nickel phthlocyanine complexes can be easily prepare using electropolymerization method and the polymeric coating produced exhibit electronic conductivity over a wide potential range. Kang *et al*. [86] developed a potentiometric pH sensor prepared by electropolymerization of a number of monomers on glassy carbon electrode.

1.5. Organo-iron complexes and carbon nanotubes

1.5.1. Metallophthalocyanine modified electrodes

Phthalocyanine was discovered during the industrial production of phthalimide at the Grangemouth plant, Scottish Dye Ltd in 1928 [96,97]. Phthalocyanine (Pc) complex (Figure 1.8) is a macrocyclic compound having an alternating nitrogen carbon atom ring structure and has been the most studied classes of organic functional materials. The diverse functionality of this macrocyle originates from its 18 π-electron aromatic system which closely resembles the naturally occuring porphyrin systems. Recently, More than seventy MPc complexes are known [98].

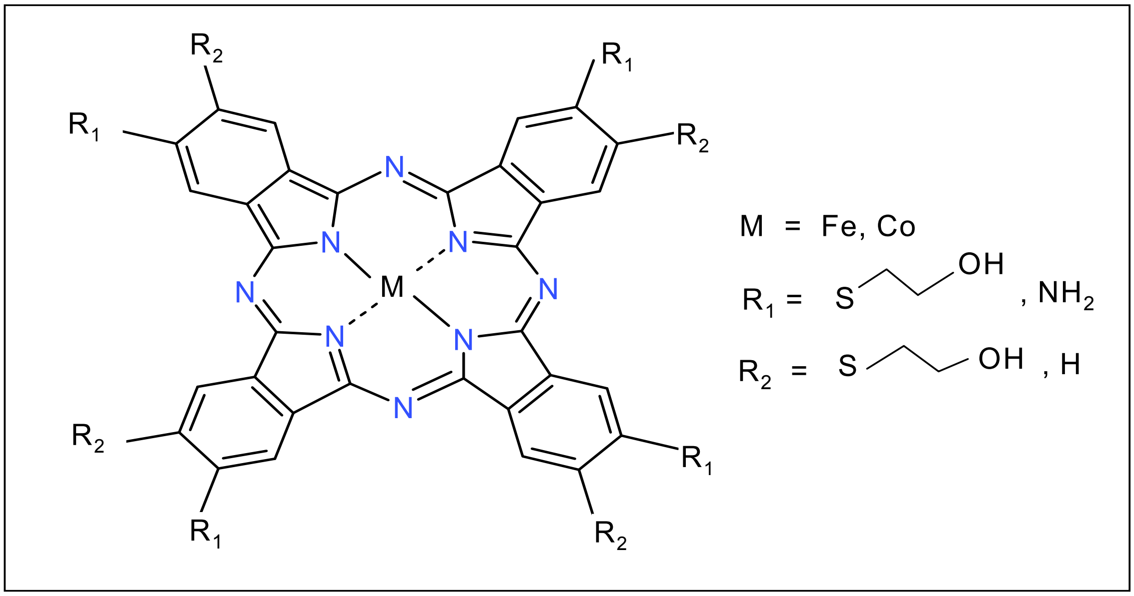

Figure 1.8: Geometric structure of metallophthalocyanines.

Like the porphyrins, the Pc macrocycle can play host to a number of different metal ions in its central cavity by coordinate bonds with the four isoindole subunits linked together by aza nitrogen atoms [98] to form metallophthalocyanines (MPcs). Incorporation of different ring substituents in the peripheral and non peripheral positions is also possible. The central atoms of MPc can carry additional ligands.

The name, Phthalocyanine, was conceived in the 1900's as a combination of prefix *phthal*, originally from the greek word naphtha meaning rock oil and *cyanine* is a synthetic dye. Many of Pc properties, for example, solubility can be varied by changing the central metal ions, axial ligands and ring substituents [99,100].

Phthalocyanines are beautiful bright blue to green coloured [99,100] that have found applications in almost every area of modern science and technology. Their bright colours have found extensive use as colorant in various areas of spin dyeing, textile dyeing and paper industry [97]. More recently they have been employed in several applications such as the photoconducting material in laser printers [97,101] and the light absorbing layer in re-writable compact disks [102-104]. They are also used as photosensitisers in laser cancer therapy [105-109], as nonlinear optical materials and as industrial catalysts, fuel cells [110] and electrochemical sensors [111-113].

MPc complexes have also established themselves as powerful electrocatalysts [102-104] when used to modify electrode materials for developing electrocatalysts and electrochemical sensors for different potential technologically important applications [114,115]. MPc complexes are readily available since they are relatively easier to synthesize and are produced in large amounts for industrial applications, less expensive and more stable to degradation than the porphyrin complexes. In this work, metallophthalocyanine together with single-walled carbon nanotubes are used as modifier in the SAM formation for detections of biological substances such as thiocynate, epinephrine and dopamine. In this work, FePc complexes were studied with a view to establish their SAM properties.

1.5.2. General overview on ferrocene-derivatised self-assembled monolayers

Ferrocene is the organometallic compound, a prototypical metallocene compound consisting of two cyclopentadienyl rings bound on opposite sides of the central metal with the five carbon atoms of each ring forming a pentahapto (η^5) arrangement (Figure 1.9).

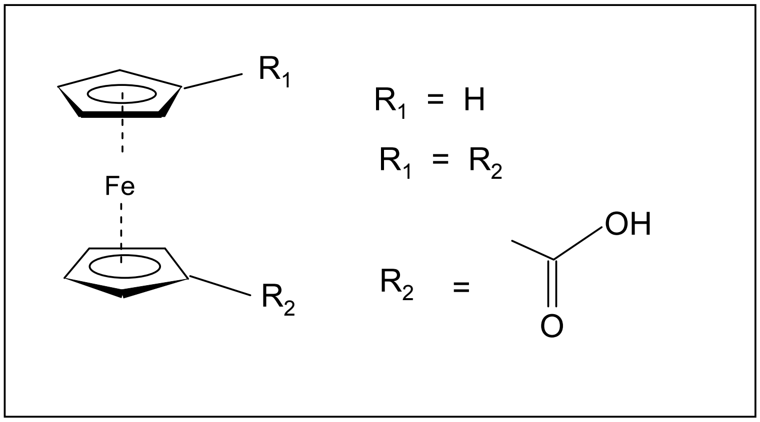

Figure 1.9: The structure of ferrocenemonocarboxylic acid (FMCA) and ferrocenedicarboxylic acid (FDCA). Both FMCA and FDCA were studied in this work.

Ferrocene undergoes a one-electron oxidation at a low potential and substituents on the cyclopentadienyl ligands alters the redox potential as expected. Electron-withdrawing groups, such as carboxylic acid, shift the potential in the anodic direction (more positive). Ferrocene and its derivatives are antiknock agents used in fuel for petrol engines and are safer than tetraethyl lead which was used previously [116]. It has no large scale applications but has found broad applications as outer sphere redox mediators, ligand scaffolds and phamarceutical candidates which exhibit anticancer activity [116]. Electron properties of a series of ester-protected amino acids coupled to ferrocenecarboxylic acid were studied by Kraatz *et al*. [117] and they showed that the redox potential of the ferrocenyl group is influenced by the amino acid substituents [118]. Ferrocene can be used to deposit certain kind of fullerenes, especially carbon nanotubes. Many organic reactions can be used to modify ferrocenes, and in this work ferrocenemonocarboxylic acid and ferrocenedicarboxylic acid were used as a mixture with carboxylated carbon nanotubes immobilized on gold surface via self-assembly technique, to investigate their joint electrochemical behavior.

1.5.3. Introduction to carbon nanotubes

Cage-like fullerenes molecules were discovered by a team headed by Harry Kroto [119], in 1985. In 1990, a team at the Max Plank institute showed that fullerenes could be mass-produced by passing a spark of electric current between two touching graphite electrodes surrounded by helium. The heat produced vaporizes the graphite and fullerenes form as the gaseous carbon cools. Iijima [1], who was then studying carbon-nanofibre and its production, which uses similar method, but decided to keep the two electrodes a short distance apart. To his surprise, he found carbon needle-like material growing on the negative electrode. It was carbon nanotubes. The introduction of catalytic plasma-enhanced chemical vapor deposition (C-PECVD) in the 1900s provided additional control mechanism over the growth of carbon nanostructures.

CNTs are divided into two main types. Figure 1.10 shows the distinct two types of carbon nanotubes. Single-walled nanotubes (SWCNTs) consist of a single graphite sheet seamlessly wrapped into a cylindrical tube that run the full length of the nanostructure. Malechko *et al.* [2] made a clear distinguishing characteristic between nanotubes and nanofibres in terms of the different chemical properties since defect-free nanotube walls do not contain the exposed edges and unsaturated bonds of graphene planes, and therefore makes the nanofibers to be more reactive than nanotubes.

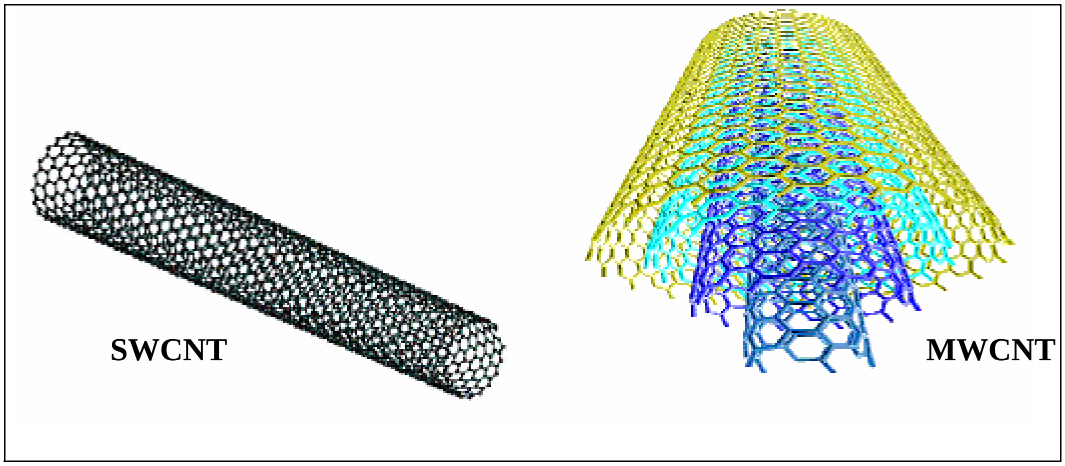

Figure 1.10: Graphical representation of SWCNT and MWCNT.

To expose the defect sites of nanotube, the harsh acid treatment of these materials was done in this work. Multiwalled nanotubes (MWCNTs) comprise an array of such nanotubes that are concentrically nested like rings of a tree trunk. Nanotube diameters range from ~0.4

to >3 nm for SWCNTs and from ~1.4 to at least 100 nm for MWCNTs [2,120]. CNTs form the basis for nanoscale tweezers that can pick-up and move tiny particles [121,122]. SWCNTs and MWCNTs are usually made by carbon-arc discharge, laser ablation of carbon, or chemical vapor deposition [120]. Synthesis of boron and/or nitrogen substituted nanotubes is one possible method to control the electronic properties of nanotubes [123-125].

However, it has been a practical problem to control the size and length of these synthesized nanomaterials, which seriously restrict the future applications. Lai *et al*. [126] was able to synthesize carbon nitride nanotubes (CN-NT) using an electron cyclotron resonance chemical vapor deposition (ECR–CVD) system with a mixture of C_2H_2 and N_2 as precursors without using any catalyst. Nanotube properties can thus be tuned by changing the diameter. Unfortunately, SWCNTs are presently produced only on a small scale and are extremely expensive in their purest form.

All currently known synthesis method for SWCNTs result in major concentration of impurities. Carbon-coated metal catalyst contaminates the nanotubes of the HiPco route, and both carbon-coated metal catalyst and, typically, ~60% forms of carbon other than nanotubes are formed in the carbon-arc route [127,128]. These impurities are typically removed by acid treatment, which introduces other impurities, can degrade or shorten nanotube length and perfection, and adds to nanotube cost. Nevertheless, the acid treatment was used in this project to shorten the tubes and introduce the carboxyl groups for ease of attachment for SAM formation. Vertically aligned periodic arrays of carbon nanotubes (CNTs) are used to create topographically enhanced light-trapping photovoltaic cells [129].

1.6. Physico-chemical characterization of modified electrodes

1.6.1. Electrochemical Impedance Spectroscopy (EIS)

The development of solid state batteries as rechargeable high-power-density energy storage devices were since developed in the late years of World War II. As a result, the characterization of systems with solid-liquid interfaces is the new revolution in high-temperature electrochemical sensors in environment, industrial, energy efficiency control and the introduction of fuel cells. Electrochemical impedance spectroscopy is a newest and powerful tool for characterization of electrochemical system mainly focusing on the electrical properties of materials and their interfaces with electronic conducting electrodes [130].

Electrochemical impedance spectroscopy describes the measurement of the impedance of a system as a function of frequency of an applied perturbation.

1.6.1.1 Basics of electrochemical impedance spectroscopy

Impedance is a measure of opposition to a sinusoidal alternating current (AC). From a physical point of view, impedance is just a totally complex resistance (measured in Ohms, Ω) that appears when an AC current flows through a circuit made of resistors, capacitors, inductors or any combination of these. This magnitude shows a complex notation, with a resistive or real part attributable to resistors (in phase with the applied voltage) and a reactive or imaginary part attributable to the contribution of capacitors (out of phase with the applied voltage by $+\pi/2$) or inductors (out of phase with the applied voltage by $-\pi/2$) as shown in figure 1.11(a).

The graphical or vector representation of imaginary impedance against the real impedance showing how impedance, Z, and phase angle, ϕ, are defined, and is called the impedance plot as illustrated in figure 1.11(b). When working with electrochemical systems, this perturbation is normally an AC voltage of small amplitude, typically 5–10 mV peak-to-peak, and the response is a current that differs in amplitude and phase (phase difference, ϕ) with the applied voltage.

Impedance is a complex function, therefore, the total impedance consist of the real component (Z') located on the abscissa which is the resistance and the imaginary component (Z'') which is the reactance, locate on the ordinates of the impedance plot in figure 1.11(b).

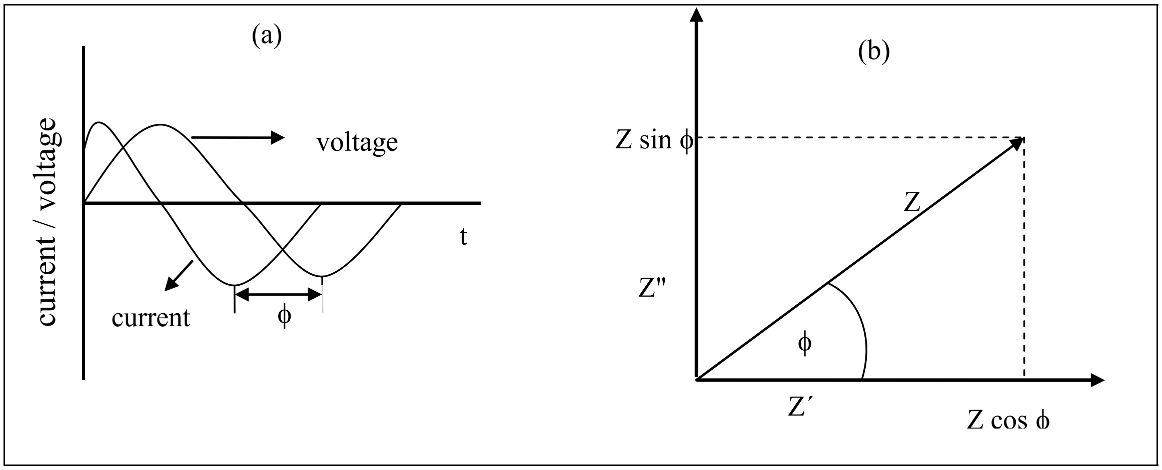

Figure 1.11: (a) Applied voltage and (b) resulting current response.

Impedance Z, Z" and Z' are related as follows :

$$Z = Z' + jZ'' \qquad (1.11)$$

where the complex number j is $(-1)^{1/2}$. In terms of the resistance and reactance, equation 1.11 can be expressed as :

$$R - jX\,; \quad \text{and} \quad X = 1/\omega C \qquad (1.12)$$

where R is the resistance (measured in Ω), X the reactance, C the capacitance (measured in Farads, F), and ω the applied angular frequency (measured in rad.s^{-1}; $\omega = 2\pi f$, f is the frequency measured in hertz). The ratio of applied voltage to measured current is the impedance, Z of the system, described by Ohms law, equation 1.13:

$$Z = E/I \qquad (1.13)$$

where E is the potential voltage or energy in volts and I the current in amperes. Impedance is, in simple terms, applying a constant voltage across a resistance R which induces a constant current I. Impedance parameters are measured as a function of frequency of the applied perturbation.

1.6.1.2 Applications and data representation

A common way of showing the resulting data is the complex plane or Nyquist Plot (Figure 1.12), in which the real Z´ versus the imaginary Z" components of the impedance are plotted.

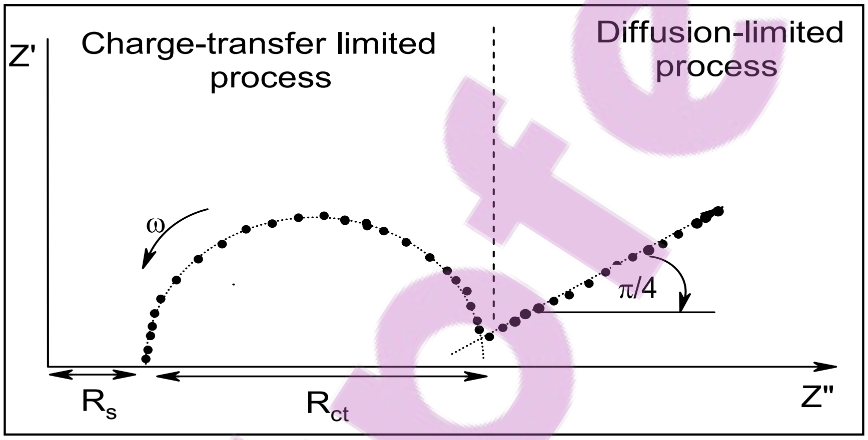

Figure 1.12: Nyquist plot for the electrochemical system with diffusion and kinetics limited processes.

In this plot, two separate processes are very well differentiated, that is, a semicircle relating to a charge-transfer-controlled process, the intercept of which with the x-axis gives R_s and R_{ct} values, and a straight line with a slope of 1 due to Z_w, whose extrapolation to the x-axis allows calculation of the Warburg coefficient, σ , from which the diffusion coefficients of the electroactive species can be estimated using equation 1.14 [131].

$$\sigma = \frac{\sqrt{2}\left(RT\ /\ F\right)}{FAC\ \sqrt{D}} \tag{1.14}$$

were F is the Faraday's constant, R is the gas constant, T is the temperature and A the geometric area of the electrode. From the frequency at the top of the semicircle, where Z" is maximum, the time-relaxation constant, τ, for the Faradaic process can also be calculated.

Another way of presenting impedance data is the Bode Plot (figure 1.13) which gives an indication of the frequency where the impedance was measured. Bode data representation is the plot of logarithm of the absolute value of Z and the phase angle, ϕ, plotted against the logarithm of frequency *f*. These data presentations give direct information about f and ϕ that help ascertain the different constituent phases of the system more easily. Thus, in those frequency regions where a resistive behaviour is dominant, a horizontal line is observed for the log Z vs log *f* representation and a ϕ close to 0^{o} is measured. Also, capacitive behaviour within a frequency region is described by a straight line with a slope of -1 in the log Z vs log *f* plots and a ϕ around 90^{o}, whereas diffusion-controlled phenomena (Warburg Impedance) would give a straight line with a slope of -1/2 and a ϕ of 45°. A detailed mathematical description of all the above parameters can be found elsewhere [132,133].

To establish whether the experimental impedance data (Nyquist and Bode plots) can be fitted to any equivalent circuit, the spectrum should be first subjected to the so-called Kramers-Kronig (K-K) assumption.

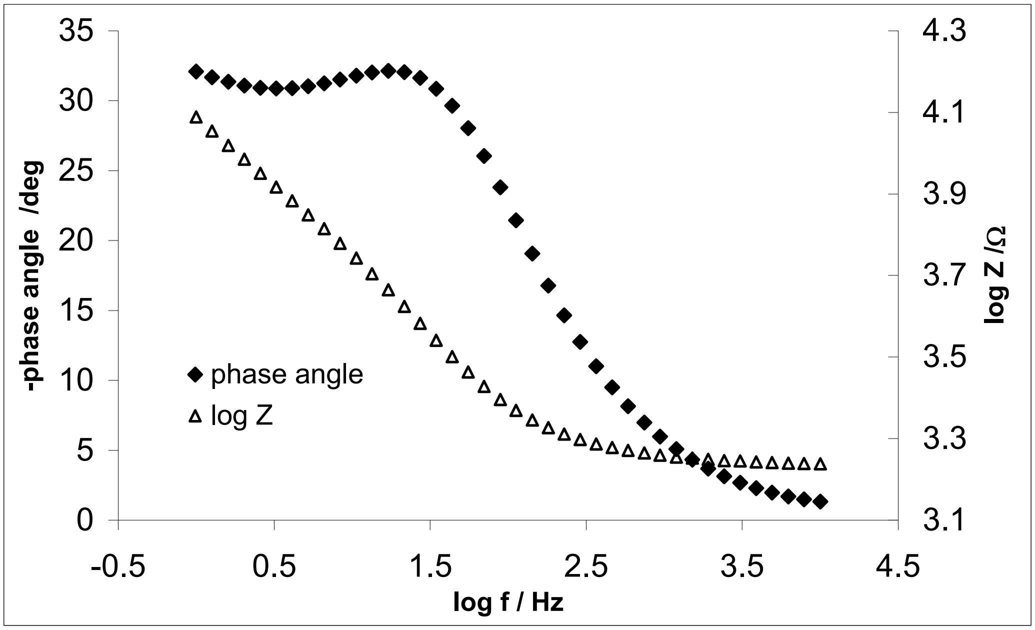

Figure 1.13: Typical Bode plots indicating the phase angle and logarithm of impedance versus frequency.

The main essence of the K-K test is simply to check whether the measured impedance spectra comply with the assumptions of the well known K-K transformation, which are (i) that the impedimetric response is only related to the excitation signal; (ii) that the impedimetric response is linear (or the perturbation is small, e.g., <10 mV, for non-linear systems; (iii) that the system does not change with time, say due to ageing, temperature changes, non-equilibrium conditions, etc; and (iv) that the system is finite for all values of ω, including zero and infinity [132,133]. Failure of the K-K test, signified by a large value of pseudo χ^2 is usually an indication that no good fit can be obtained using the electrical equivalent circuit methods. It should be noted that aside from visual inspection of goodness of the fitting lines, two accurate ways to establish how well the modeling functions reproduce the experimental data sets are the relative error estimates (in %) and chi-square functions (χ^2) [134], which is the sum of squares of the relative residuals (i.e., sum of the real and imaginary χ^2), easily obtained from the K-K test.

Experimental impedance data of an electrochemical cell can be easily fitted to the impedance of an equivalent circuit mainly comprising resistors and capacitors. Equivalent circuit concept is the heart of impedance analysis. In such circuits, a resistance ideally describes a conductive path, such as that generated by the bulk conductivity of the system or the charge-transfer step due to an electrode reaction, whereas a capacitance generally describes space-charge-polarisation regions within the system as well as modification of an electrode surface due to adsorption processes or polymer-layer deposition. The Randles circuit [135] in Figure 1.14, is the simplest equivalent circuit that describes an electrochemical cell where a single-step Faradaic process in the presence of diffusion may occur.

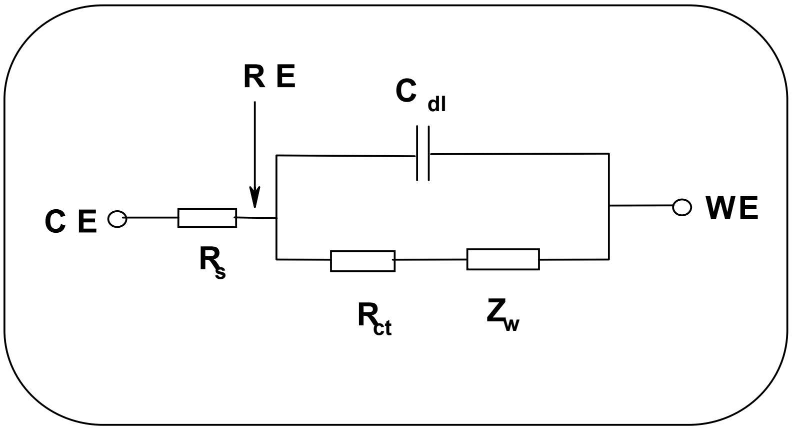

Figure 1.14: Randles electronic equivalent circuit (for an ideal situation).

It combines three components, namely the electrolyte resistance between working and reference electrodes R_s, the double layer capacitance (C_{dl}), and the Faradaic impedance consisting of charge-transfer resistance R_{ct} at the working electrode-electrolyte interface and the so-called Warburg Impedance Z_w, which reflects the influence of the mass transport of the electroactive species on the total impedance of the electrochemical cell. Thus, for those diffusion-limited processes, Z_w becomes dominant, whereas for those charge-transfer-controlled processes, only R_{ct} can be obtained.

For a practical situation, the double layer capacitance (C_{dl}) in the Randles equivalent electric circuit is replaced by the constant phase element (CPE) as depicted in Figure 1.15.

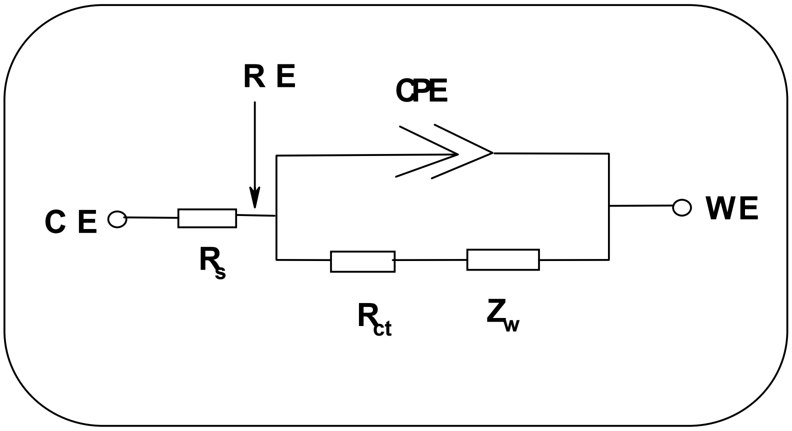

Figure 1.15: Modified Randles equivalent electric citcuit (for a real practical situation)

The impedance of the CPE (Z_{CPE}) is a power-law dependent interfacial capacity defined as [136]:

$$Z_{CPE} = \frac{1}{[Q(j\omega)^n]} \tag{1.15}$$

where *Q* is the frequency-independent constant relating to the surface electroactive properties, ω is the radial frequency, the exponent n arises from the slope and the exponent n has values $-1 \le n \le 1$ which is estimated from the slope of log Z vs log f. If $n = 0$, the CPE behaves as a pure resistor; $n = 1$, CPE behaves as a pure capacitor, $n = -1$ CPE behaves as an inductor; while $n = 0.5$ corresponds to Warburg impedance (Z_W) which is associated with the domain of mass transport control arising from the diffusion of ions to and from the electrode|solution interface. Generally speaking, CPE has been known to occur via several factors notably (i) the nature of the electrode (e.g., roughness and polycrystallinity), (ii) distribution of the relaxation times due to heterogeneities existing at the electrode/electrolyte interface, (iii) porosity and (iv) dynamic disorder associated with diffusion [137].

1.6.1.3 Factors affecting rate of electron transfer

Several factors affect the response of modified electrode, notably, the SAM-modified electrode. Passivation is one of them. It results if the electrode surface is modified with a resistive monolayer and hence alters their AC response. In terms of the Randles equivalent circuit, some components are affected [134]. Firstly, at high frequency where the electrode reaction is purely kinetic controlled, the heterogeneous charge-transfer resistance is expected to increase due to inhibition of the electron-transfer rate.

The increase in the charge-transfer resistance is related to the electrode coverage and is given by:

$$1 - \theta = \frac{R_{ct}^{0}}{R_{ct}} \tag{1.16}$$

where θ is the apparent electrode coverage, assuming that all the current is passed via bare spots on the electrode, R_{ct}^{0} is the charge-transfer resistance measured at a bare electrode, and R_{ct} is the charge-transfer resistance measured under the same conditions at the monolayer-covered electrode.

Secondly, at lower frequencies the Warburg impedance is expected to deviate from a linear dependence upon $\omega^{1/2}$, which is the behaviour in the case of a semi-infinite diffusion. Such deviation would be manifested in cases where the defects or pinholes in the monolayer are far apart from each other when compared to the diffusion layer thickness. In this situation when the diffusion layers of neighbouring pinhole overlap. There maybe, however, a situation where the diffusion layers do overlap, even at highly covered electrodes. Then, the AC response at low frequencies resembles the behaviour of bare electrodes.

Equation 1.16 assumes that the current is due to the presence of defects within the monolayer [131] (defect is a site at which molecules or ions can approach the electrode surface at a distance shorter than the normal thickness of the SAM) and should not be used when the surface coverage values are close to 1, i.e $\theta > 0.9$. Using these θ values, the size and the distance between pinholes may be estimated from equations (1.17) and (1.18). A pinhole is a site at which the electrode surface is exposed to the electrolyte.

$$r_a = \frac{r_b}{\sqrt{(1-\theta)}} \tag{1.17}$$

$$r_b = \frac{\gamma(1-\theta)}{\sigma\sqrt{\frac{0.72}{D}}} \tag{1.18}$$

where r_a and r_b are the size and distance between pinholes, respectively, γ is the y intercept of the plot of $Z' \; vs \; \omega^{-1/2}$. Graphical representation that illustrates the concept of defects and pinholes is shown in figure 1.16.

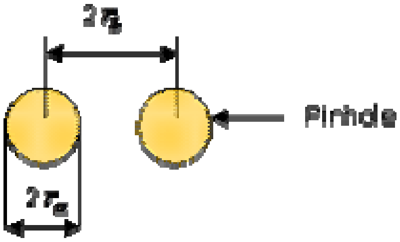

Figure 1.16: Illustration of the defects and the pinholes.

1.6.2. Atomic Force Microscopy

Scanning probe microscopes (SPM) describes a broad group of instruments use to image and measure properties of chemical species on solid surfaces. The two major forms of SPM are scanning tunneling microscopy (STM) and atomic force miscroscopy (AFM). Acquiring a topographic image with high resolution to investigate the properties of a sample surface, atomic force miscroscopy, (AFM), is the standard technique to use.

Atomic force microscopy is a probe microscope which was invented in 1982 [138] and operates by measuring the force between the probe and the sample [139,140]. The probe consists of a sharp tip made of silicon or silicon nitride, attached to a force-sensitive cantilever. The tip scans across the surface by a piezoelectric scanner, and the cantilever deflects in response to force interactions between the tip and the substrate. Such deflection is monitored by bouncing a laser beam off it onto a photodector. The Atomic Force Microscope was developed to overcome a basic drawback with STM, that it can only image conducting or semiconducting surfaces or samples. The AFM, however, has the advantage of imaging almost any type of surface, including polymers, ceramics, composites, glass, and biological samples [141]

The atomic force microscope relies on the force between the tip and sample, knowing this force is important for proper imaging. Hook's law gives :

$$F = -kz \tag{1.19}$$

where F is the force, k the stiffness of the lever, and z is the deflection of the cantilever. The force is not measured directly, but calculated by measuring the deflection of the lever, and knowing the stiffness of the cantilever. When the maximum deflection for a given force is needed, a soft spring is required. This makes the spring the critical component because a stiff spring with high resonant frequency is necessary in order to minimize the sensitivity to vibrational noise [141]. The resonant frequency of the spring is given by equation 1.20: [138]

$$f_o = \tfrac{1}{2}\pi\sqrt{k/m_o} \tag{1.20}$$

where k is the spring constant and m_o is the effective mass that loads the spring. Equation 1.20 suggests that as k is reduced to soften the spring, m_o must also decrease to keep the ratio k/m_o large. Binning *et al*. [138] proposed a measurement of ultrasmall forces on particles as small as a single atom by monitoring the elastic deformation of different types of springs as a measure of force.

(a) Contact mode AFM

This is a scanning probe mode which operates by rastering a sharp tip across a sample. The performance of AFM is critically dependent upon the physical characteristics of the cantilever of low spring constant and the tip. A low interatomic force is maintained on the cantilever as it rasters and thereby pushing the tip against the sample. The repulsive force between the tip and the sample or the actual tip deflection is recorded relative to spatial variation and then converted into an analogue image of the sample surface. The AFM tip is manually brought close to the sample surface and the scanner makes the final adjustment in tip sample distance based on the setpoints determined by the user. The tip in contact with the sample surface through any adsorbed gas layer is then scanned across the sample under the action of piezoelectric actuators by moving either the sample or the tip relative to the other. At the back of the cantilever is the laser beam which reflects off the cantilever surface to a split photodiode and then detects the small cantilever deflections.

(b) Non-contact mode

Non-contact mode AFM does not suffer from tip or sample degradation effects that are sometimes observed after taking numerous scans with contact AFM. This is due to the tip of the cantilever which does not come in contact with the sample surface. The cantilever is instead oscillated at a frequency slightly above its resonance frequency where the amplitude of oscillation is typically a few nanometers (<10 nm) [138]. This makes non-contact AFM preferable to contact AFM for measuring soft samples. In the case of rigid samples, contact and non-contact images may look similar.

However, if a few monolayers of adsorbed fluid are lying on the surface of a rigid sample, the images may look quite different. An AFM operating in contact mode will penetrate the liquid layer to image the underlying surface, whereas in non-contact mode an AFM will oscillate above the adsorbed fluid layer to image both the liquid and surface. However, both contact and non-contact mode AFM were used in this thesis.

1.6.3. Scanning Electron Microscopy

Scanning electron microscopy, SEM, is used for inspecting topographies of specimens at much greater resolution, approximately 5nm magnifications [142]. During this inspection, a beam of electrons is focused on a spot volume of the specimen, resulting in the transfer of energy to the spot. These bombarding electrons, also referred to as primary electrons, dislodge electrons from the specimen itself. The dislodged electrons, also known as secondary electrons, are attracted and collected by a positively biased grid or detector, and then translated into a signal. To produce the SEM image, the electron beam is swept across the area being inspected, producing many such signals. These signals are then amplified, analyzed, and translated into images of the topography being inspected.

The energy of the primary electrons determines the quantity of secondary electrons collected during inspection. The emission of secondary electrons from the specimen increases as the energy of the primary electron beam increases, until a certain limit is reached. Beyond this limit, the collected secondary electrons diminish as the energy of the primary beam is increased, because the primary beam is already activating electrons deep below the surface of the specimen. Electrons coming from such depths usually recombine before reaching the surface for emission.

A beam of electrons must travel to the sample, therefore, the sample must be vacuum compatible and either electrically conducting or coated with a conductive layer to avoid sample build-up [143]. The surface of a solid sample is scanned in a raster pattern with a beam of energetic electrons to produce signal of several types including backscattered, Auger electrons and X-ray fluorescence photons. Backscattered electrons serve as the basis of scanning electron microscopy, whereas, X-ray emission is used in electron microprobe analysis.

1.6.4. X-ray Photoelectron Spectroscopy

Electron spectroscopy is a powerful tool for the identification of most the elements in the periodic table with the exception of hydrogen and helium. It provides useful information about the electronic structure of molecules, permits determination of the most oxidation state of an element and the type of species to which it is bound. For the study of surfaces, there are three types of electron spectroscopy. The most common type, which is based on upon irradiation of the sample surface with monochromatic X-radiation is called X-ray photoelectron spectroscopy (XPS).

It utilizes X-Rays with low energy (typically 1-2 keV) to knock off photoelectrons from atoms of the sample through the photoelectric effect. The energy content of these ejected electrons is then analyzed by a spectrometer to identify the elements where they came from [144]. The spectra provide not only qualitative information about the type of atoms present in a compound but also the relative number of each type. It is worthwhile pointing out that the photo-electrons produced in XPS are incapable of passing through a solid. Thus the most important application of electron spectroscopy is the accumulation of information about surfaces.

Its use includes identification of active sites and poisons on catalytic surfaces, determination of surface contaminants on semiconductors, analysis of the composition of human skin and the study of oxide surface layers on metals and alloys.

1.7. Background on the studied analytes

1.7.1. Potassium thiocyanate

Thiocyanate is considered to be non-toxic and its concentration in mining effluent is not regulated at the present time [145]. However, it is known that ultraviolet light decomposes thiocyanate to form cyanide, it is then possible that sunlight may liberate cyanide levels toxic to aquatic life from effluent rich in thiocyanate. In view of these considerations, it is not unlikely that in the future some limit may be imposed on the concentration of thiocyanate in effluent. It is known to block the iodine uptake by thyroid gland. Is a detoxification product of hydrogen cyanide [6,146]. It has been used in the body fluid to monitor hydrogen cyanide from tobacco smoke, fire atmospheres and some vegetables containing cyanogenic glucosides [147]. In addition to the use of modified metallic electrodes, a number of researchers [146,148,149] are using ion selective electrode to determine thiocyanate. Unsubstituted iron-phthalocyanine, FePc [150], has also been used as a modifier to analyze thiocyanate in human urine and saliva samples.

REFERENCES

1. S. Iijima, *Nature* 354 (1991) 56.
2. P. G. Wiles, J. Abrahamson, *Carbon* 6 (1978) 341.
3. P. J. Britto, K. S. V. Santhanam, P. M. Ajayan, *Bioelectronics and Bioenergertics* 41 (1996) 121.
4. J. Wang, *Electroanalysis* 17 (2005) 7.
5. B. S. Flaven, J. Yu, A. V. Ellis and J. G. Shapter, *Electrochim. Acta* 54 (2009) 3191.
6. K. I. Ozoemena and T. Nyonkong, *Encyclopedia of Sensors* (ed.) C. A. Grimes, E. C. Dickey, and M. V. Pishko 3 (2006) 157.
7. M. Sekota and T. Nyonkong, *Polyhedron* 16 (1997) 3279.
8. S. Vilakazi and T. Nyonkong, *Polyhedron* 19 (2000) 229.
9. J. Limson and T. Nyonkong, *Electroanalysis* 9 (1997) 255.
10. M. Thamae and T. Nyonkong, *J. Elecrtoanal. Chem*. 470 (1999) 126.
11. S. Grieve, G. Pavez, J. H. Zagal and F. Bedioui, *J. Electroanal. Chem*. 497 (2001) 75.
12. B. O. Agboola and K. I. Ozoemena, *Phys. Chem. Chem. Phys* 10 (2008) 2399.
13. J. M. Lehn, *Supramolecular chemistry,* VCH Weinhein (1995).

14. J. N. Richardson, S. R. Peck, L. S. Curtin, L. M. Tender, R. H. Terrill, M. T. Carter, R. W. Murray, G. K. Rowe and S. E. Creager, *J. Phys. Chem.* 99 (1995) 766.
15. K. Weber, L. Hockett and S. E. Creager, *J. Phys. Chem. B* 101 (1997) 8286.
16. S. E. Creager and G. K. Rowe, *Anal. Chim. Acta* 246 (1991) 233.
17. S. E. Creager and G. K. Rowe, *Langmuir* 9 (1993) 2330
18. J. J. Gooding, A. Chou, J. Liu, D. Losic, J. G. Shapter, D. B. Hibbert, *Electrochem. Commun.* 9 (2007) 1677.
19. P.M. S. Monk, *Fundamentals of Electroanalytical Chemistry*, John Wiley and Sons Ltd, Chichester, New York (2001)
20. P. T. Kissinger, C. R. Preddy, R. E. Shoup and W. R. Heineman in *Laboratory Techniques in Electroanalytical Chemistry* 2nd ed., P. T. Kissinger and W. R. Heineman, Eds.; Marcel Dekker Inc., New York 1996.
21. J. Wang, Analytical *Electrochemistry*, VCH Publishers Inc. New York (1994).
22. D. B. Hibbert, *Introduction to Electrochemistry*, Macmillan, London (1993).
23. A. E. Kaifer and M. Gómez-Kaifer, *Supramolecular Electrochemistry*, Wiley-VCH, New York (1999).

24. A. J. Bard, L. R. Faulkner, *Electrochemical methods: Fundamental and applications*, 2nd ed., John Wiley and Sons, Hoboken, NJ, (2001).

25. C. Kittel, *Thermal physics*, 3rd edn, Wiley, New York (1969) 215.

26. G. Inzelt, Kinetics of electrochemical reactions. In: Scholz F (ed) *Electroanalytical methods* Springer, Berlin (2002) 38.

27. P. A. Christenson and A. Hamnet, *Techniques and Mechanisms in Electrochemistry*, 1st ed, Blackie Academic and Professional, London (1994).

28. J. E. B. Randles, *Trans. Faraday Soc*. 44 (1948) 327.

29. R. S. Nicholson and I. Shain, *Anal. Chem*. 36 (1964) 1351.

30. A. Sevcik, Coll. Czech. *Chem. Comm*. 13 (1958) 349.

31. J. Wang, *Analytical Electrochemistry*, 3rd ed, Wiley-VCH John Wiley & Sons Publishers Inc., Hoboken, New Jersey (2006).

32. E. R. Brown and R. F. Large, *in Physical Methods of Chemistry, Vol.1-Part IIA:Electrochemical Methods*, eds. A. Weissberger and B. Rossiter, Willey-Interscience, New York (1971).

33. F. M. Hawkridge in P. T. Kissinger and W. R. Heineman (Eds), *Laboratory techniques in electroanalytical chemistry*, 2nd ed., Marcel Dekker Inc., New York (1996).

34. J. Wang, *Analytical Electrochemistry*, VCH Publishers Inc., New York (1994).

35. J. Wang, D. B. Luo, P. A. M. Farias and J.S. Mahmoud, *Anal. Chem.* 57 (1985) 101.

36. J. G. Osteryoung, *Acc. Chem. Res*. 26 (1993) 77.

37. J. G. Osteryoung and R. A. Osteryoung, *Anal. Chem*. 57 (1985) 101A.

38. J. A. Turner, J. H. Christie, M. Vukovic, R. A. Osteryoung, *Anal. Chem*. 49 (1977) 1904.

39. G. C. Barker, A. W. Gardner, *J. Electroanal. Chem*. 100 (1979) 641.

40. S. Komorsky-Lovric, M. Lovric, M. Branica, *J. Electroanal.Chem*. 241 (1988) 329.

41. H. B. Oldham and J. C. Mayland, *Fundamentals of electrochemical science*, Academic press, San Diego (1994).

42. P. H. Rieger, *Electrochemistry*, Prentice Hall, Oxford (1987) 151.

43. A. J. Bard (ed) *Electroanalytical Chemistry*, Marcel Dekker, New York 13 (1994) 191.

44. A. J. Bard (ed) Electroanalytical Chemistry, Marcel Dekker, New York 18 (1994) 89.

45. R. G.Compton and C. E. Banks, *Understanding Voltammetry*, World Scientific Publishing Co. Pte. Ltd (2007).

46. J. Ni, H. Ju, H. Chen and D. Leech, *Anal. Chim. Acta* 378 (1999) 151.

47. A. J. Bard, G. Inzelt and F. Scholz, *Electrochemical dictionary*, Springer (2008).

48. R. D. Rocklin and R. W. Murray, *J. Phys. Chem.* 85 (1981) 2104.

49. F. Zhi, X. Lu., Y. Jiandong, X. Wang, H. Shang, S. Zhang, X. Zhonghua, J. Phys. Chem. C 113 (2009) 13166.

50. C. Chuangye, S. Yonghai; L. Wang, Electro. Chim. Acta 54 (2009) 1607.

51. R. G. Gonzalez-Huerta, A. R. Pierna, O. Solorza-Feria, J. New Mat. Electrochem. Syst. 11 (2008) 63.

52. I. Kazufumi, N. Katsuhiko, T. Isao, Chem. Lett. 38 (2009) 686.

53. R. N. Goyal, V. K. Gupta, S. Chatterjee, Biosensors & Bioelectronics 24 (2009) 3562.

54. M. H. Smit, C. A. Rechnitz, *Anal. Chem.* 64 (1992) 245.

55. X. Cai, K. Kalcher, C. Neuhold, W. Diewald, R. J. Magee, *Analyst* 118 (1993) 53.

56. S. M. Golabi, J. B. Raoof, *J. Electroanal. Chem*. 46 (1996) 75.

57. S. A. Wring, *Analyst* 117 (1992) 1215.

58. R. A. Durst, A. J. Baumner, R. W. Murray, R. P. Buck and C. P. Andrieux, *Pure Appl. Chem.* 69 (1997) 1317.

59. K. A. Peterlinz and R. Goergiadis, *Langmuir* 12 (1996) 4731.

60. B. Fang, X. H. Deng, X. W. Ken, H. S. Tao, W. Z. Zhang and M. G. Li, *Anal. Lett.* 39 (2006) 697.

61. J. Yu, J.G. Shapter, M. R. Johnston, J. S. Quinton, and J. J. Gooding, *Electrochim. Acta.* 52 (2007) 6206.

62. M. D. Porter, T. B. Bright, D. L. Allara, and C. E. D. Chidseyi, *J. Am. Chem. Soc*. 109 (1987) 1559.

63. R. G. Nuzzo, B.R. Zegarski and L. H. Dubois, *J. Am. Chem. Soc*. 109 (1987) 733.

64. L. H. Dubois and R. G. Nuzzo, *Ann. Rev. Phys. Chem*. 43 (1992) 437.

65. S. Griveau, J. Pavez, J. H. Zagal and F. Bedioui, *J. Electroanal. Chem.* 497 (2001) 75.

66. K. I. Ozoemena and T. Nyonkong, *Talanta* 67 (2005) 162.

67. G. M. Whiteside and B. Grzybowski, *Science* 295 (2002) 2418.

68. G. R. Desiraju*, Crystal Engineering: The Design of Organic Solids*, Elsevier, New York (1989).

69. L. Isaacs, D. N. Chin, N. Bowden, Y. Xia, G. M. Whitesides, *Supramolecular Technology,* D. N. Reinhoudt, Ed., Wiley, New York (1999) 1-46.

70. R. K. Shervedani, M. Bagherzadeh and S. A. Mozaffari, Sens. Actuators B 115 (2006) 614.

71. H. Wang, S. Chen, L. Li and S. Jiang, Langmuir 21 (2005) 2633.

72. R. K. Shervedani and S. A. Mozaffari, *surf. Coat. Technol.* 198 (2005) 123.

73. Y. I. Skurlatov, L. S. Ernestova, E. V. Vichutinskaya, D. P. Samsonov, I. V. Semenov, I. Y. Rod'ko, V. O. Shvidky, R. I. Pervunina and T. J. Kemp, *J.Photochem.Photobiol.* 107 (1997) 207.
74. W. A. Nevin, W. Liu, S. Greenberg, M. R. Hempstead, S. M. Maruccio, M. M. Melnik, C. C. Leznoff and A. B. P. Lever, *Inorg. Chem*. 26 (1987) 291.
75. H. O. Finklea in *Electroanalytical Chemistry*, A. J. Bard and I. Rubinstein, Eds., Marcel Dekker: New York 19 (1996) 109.
76. H. O. Finklea in R. A. Meyers, Eds., *Encyclopaedia of Analytical Chemistry: Applications, Theory and Instrumentations*, Vol. 11, Wiley, Chichester (2000) 10090.
77. D. Losic, J. G. Shapter and J. J. Gooding, *Langmuir* 17 (2001) 3307.
78. K. C. Nirmalya, M. Aslam, J. Sharma and K. Vijayamohanan, *Proc. Indian Acad. Sci (Chem. Sci.)* 113 (2001) 659.
79. M. Mrksich, G. M. Whitesides, *Annu. Rev. Biomol. Struct.* 25 (1996) 55.
80. J. J Gooding, V. Praig and E. A. H Hall, *Anal. Chim. Acta* 70 (1998) 2396.
81. Y. Okahata, Y. Matsunobu, K. Ijiro, M. Mukae, A. Murakami and K. Makino, *J. Am. Chem. Soc.* 114 (1992) 8299.

82. W. Wang, J. J. Gooding and D. B. Hibbert, *J. Electroanal. Chem.*516 (2001)10.

83. H. O. Finklea and D. D. Hansheu, *J. Am. Chem. Soc.* 114 (1992) 3173.

84. A. M. Becka and C. J. Miller, *J. Phy. Chem.* 96 (1992) 2657.

85. Y. H Tse, P. Janda and A. B. P. Lever, *Anal. Chem.* 66 (1994) 384.

86. T. F. Kang, Z. Y. Xie, H. Tang, G. L. Shen and R. Q. Yu, *Talanta* 45 (1997) 291.

87. M. Thamae and T. Nyonkong, *J. Electroanal. Chem.* 470 (1999) 126.

88. T. Mafatle and T. Nyonkong, *Anal. Chim. Acta.* 354 (1997) 307.

89. C. A. Caro, F. Bedioui and J. A. Zagal, *Electro. Chim. Acta* 47 (2002) 1489.

90. A. J. Bard, J. Chem. Ed. 60 (1983) 302.

91. I. Zilbermann, J. Hayon, T. Katchalski, R. Ydgar, J. Rishpon, A. I. Shames, E. Korin and A. Bettelheim, *Inorg. Chim. Acta.* 305 (2000) 53.

92. M. J. Cook, J. Mater. *Chem.* 6 (1996) 677

93. M. J. Cook, *Pure Appl. Chem*. 71 (1999) 2145.

94. A. Ulmann, *An introduction to ultrathin organic films from Langmuir-blodgett to self-assembly*, Academic Press, San Diego (1991).

95. H. Li, T. F. Guarr, *J. Chem.Soc. Chem.Commun.* (1989) 832.

96. J. M. Robertson, *J. Chem. Soc.* (1936) 1195.

97. P. Gregory, *J. Porphyrins Phthalocyanines* 3 (1999) 468.

98. N. B. McKeown, *Chem. Ind.* (1999) 92.

99. T. Nyokong, Z. Gasyna and M.J. Stillman, *Inorg. Chem.* 26 (1987) 548.

100. J. Simon and P. Bassoul, *Phthalocyanine: Properties and Applications,*Leznoff, C.C., Lever, A.B.P., Eds. V.H.S. Publishers: New York (1989).

101. P. Gregory in *High Technology Applications of Organic Colorants*, Plenum Press, New York (1991).

102. J. E. Kuder, *J. Imaging Sci*., 32 (1988) 51.

103. R. Ao, L. Kummert and D. Haarer, *Adv. Mater*. 5 (1995) 495.

104. H. S. Nalwa and J. A. Shirk in *Phthalocyanine: Properties and Applications,*(A. P. B. Lever and C. C. Leznoff, Eds), VCH Publishers, New York 4 (1996) 79.

105. E. Ben-Hur and I. Rosenthal, *Int. J. Radiat. Biol*. 47 (1985) 145.

106. E. Ben-Hur and I. Rosenthal, *J. Photochem. Photobiol*. 42 (1985) 129.

107. I. Rosenthal and E. Ben-Hur, *in Phthalocyanine: Properties and Applications,*eds. A.P.B. Lever and C.C. Leznoff, VCH Publishers, New York, 1 (1989).

108. D. Phillips, *Pure Appl. Chem*. 67 (1995) 117.

109. I. J. MacDonald and T. Dougherty, *J. Porphyrins Phthalocyanines* 5 (2001) 105.

110. A. B. P. Lever, M. R. Hempstead, C. C. Leznoff, W. Lui, M. Melnik, W. A Nevin and P. Seymour, *Pure Appl. Chem*. 58 (1986) 1467.

111. K. Morishige, S. Tomoyasu and G. Iwano, *Langmuir* 13 (1997) 5184.

112. A. W. Snow and W.R. Barger in *Phthalocyanines: Properties and Applications* eds. A.P.B. Lever and C.C. Leznoff, VCH Publishers, New York 1 (1989).

113. S. Vilakazi and T. Nyokong, *Polyhedron* 19 (2000) 229.

114. T. Nyonkong and S. Vilakazi, *Talanta* 61 (2003) 27.

115. J. H. Zagal, *Coord. Chem. Rev.* 119 (1992) 89.

116. S. Top, A. Vessières, G. Leclercq, J. Quivy, J. Tang, J. Vaissermann, M. Huché and G. Jaouen, *Chem. Eur.J.* 9 (2003) 5223.

117. H. B. Kraatz, J. Lusztyk and G. D. Enright, *Inorg. Chem.* 36 (1997) 2400.

118. P. Saweczko, H. -B. Kraatz, *Coord. Chem. Rev.* 190 (1999) 185.

119. P. Allan and L. Jason, Chem Rev. 7 (1997) 6.

120. Z. K. Tang, Z. Lingyun, N. Wang, X. X. Zhang, G. H. Wen, G. D. Li, J. N. Wang, C. T. Chan and P. Sheng, *Science* 292 (2001) 2462

121. R. G. Ding, G. Q. Lu, Z. F. Yan, and M. Wilson, *J. Nanosci. Nanotechnol.* 1 (2001) 7.

122. P. Ball, *Nature* 414 (2001) 142.

123. P. Kim and C. M. Lieber, *Science* 286 (1999) 2148.

124. O. Stephan, P. M. Ajayan, C. Colliex, Ph. Redlich, J. M. Lambert, P. Bernier, P. Lefin, *Science* 266 (1994) 683.

125. R. Sen, B. C. Satishkumar, A. Govindaraj, K. R. Harikumar, G. Raina, J. -P. Zhang, A. K. Cheetham, C. N. R. Rao, *Chem. Phys.Lett.* 287 (1998) 671.

126. M. Yudasaka, R. Kikuchi, Y. Ohki, S. Yoshimura, *Carbon 35* (1997) 195.

127. S. H. Lai, Y. L. Chen, L. H. Chan, Y. M. Pan, X. W. Liu, H. C. Shih, *Thin Solid Films* 444 (2003) 38.

128. S. G. Louie, *Top. Appl. Phys*. 80 (2001) 113.

129. R. Camacho, A. Morgan, M. Flores, T. McLeod, V. Kumsomboone, B. Mordecai, R. Bhattacharjea, W. Tong, B. Wagner, J. Flicker, S. Turano, W. Ready, *J. Min. Metals and Mater. Soc.* 59 (2007) 39.

130. B. A. Boukamp, *Solid States Ionics* 18 and 19 (1986) 136.

131. S. Khene, D. A. Geraldo, C. A. Togo, J. Limson and T. yonkong*,* *Electro. Chim. Acta.* 54 (2008) 183.

132. C. M. Brett, A. M. O. Brett, *Electrochemistry: Principle, methods and Applications*, Oxford University Press, New York, USA (1993).

133. S. Krause, Impedance methods, in A. J. Bard, M. Stratmann, P. R. Unwin (Eds), *Encyclopedia on Electrochemistry*, vol 3, Wiley-VCH, Weinheim, Germany (2003).

134. Y. Yang, S. B. Khoo, *Sens. Actuators B* 97 (2004) 221.

135. X. Ren, P. J. Puckup, *J. Electroanal. Chem.* 420 (1997) 251.

136. A Chidembo, B. A. Agboola, V. Gupta, G. G. Wildgoose, R. G. Compton and K. I. Ozoemena, Chem. Commun. (2009) in press.

137. D. D. MacDonald, *Electrochim. Acta*, 51 (2006) 1376.

138. G. Binning, C. F. Quate and C. Gerber, Phys. Rev. Lett. 56 (1986) 930.

139. H. Hansma, A. Weisenhorm, A. Edmundson, H. Gaub and P. Hansma, *Clin. Chem*. 37 (1991) 1497.

140. C. E. Gardner, J. V. Macpherson, *Anal. Chem.* 74 (2002) 576A.

141. C. R. Blanchard, *The chemical educator* 1 (1996) 1.

142. Y. A. Novikov, Y. V. Ozerin, A. V. Rakov and P. A. Todua, Measurement Sci. Technol. 18 (2007) 367.

143. S. Guenu, A. E. Heng, F. Charbonne, M. J. Galmier, F. Charles, P. Deteix, B. Souweine and C. Lartigue, Rapid Comm. Mass Spectrom. 21 (2007) 229.

144. D. Briggs and M. P. Seah, Practical Surface Analysis by Auger and X-Ray Photoelectron Spectroscopy, Eds. New York: Wiley 1983

145. J. Javier, S. Heriban and N. Fabiola, *Regeneration of Cyanide by oxidation of thiocyanate* (1996) US Patent 5482694.

146. K. A. Singh, U. P. Singh, S. Mehtab and V. Aggarwal, *Sens. Actuators* B 125 (2007) 453.

147. J. A. Cox and T. Gray, *Anal. Chem.* 60 (1988) 1710.

148. A. Abbaspour, M. A. Kamyabi and R. K. Esmaeilbeig, *Talanta* 57 (2002) 859.

149. M. K. Amini, S. Shahrokhian, and S. Tangestaninejad, *Anal. Chim. Acta.* 402, (1999) 137.

150. K. O. Ozoemena and T. Nyonkong, *J. Electroanal. Chem.* 579 (2005) 283.

CHAPTER 2

EXPERIMENTAL

2.1. Introduction

This chapter describes the reagents and their grades, as well as the equipments used to carry out the experiments reported in this thesis. The method used to functionalize carbon nanotubes is reported in details. Also, described are the characterization techniques employed in this project, namely SEM, XPS, AFM and EDX.

2.2. Reagents and material

Table 2.1 lists the reagents used and their purity or composition in weight %. The reagents were of analytical grade and were used as received from the suppliers without further purification.

Gold electrode of radius 0.8 mm from Bioanalytical systems (BAS), the rotating disk electrode consists of a 5 mm gold disk of radius 2.5 mm embedded in a cylindrical insulating material (e.g Teflon) were obtained from Eco Chemie. The electrodes were cleaned before forming the SAM following the same procedure described below for the normal electrode of radius 0.8 mm. ITO-gold nanoparticles (used as received).

Saliva samples of smokers and non-smokers were donated by colleagues at the University of Pretoria. 1 ml of saliva sample was diluted to 1:10 with pH 4.8 phosphate buffer. The resulting mixture was used directly for determination of thiocyanate ion concentration.

Table 2.1: List of reagents, their purity and suppliers

Reagents	Purity or composition (wt%)	Supplier
Alumina		Sigma
Cobalt tetraaminophthalocyanine(II)[a]	—	—
Cysteamine hydrochloride	98.0	Fluka
Dicyclohexylcarbodiimide	99.0	Aldrich
N,N-dimethylformamide	99.0	SAARCHEM
Ethanol	99.5	SAARCHEM
Ferrocenecarboxylic acid	97.0	Fluka
1,1-Ferrocene-dicarboxylic acid	96.0	Aldrich
Hydrogen peroxide	30.0	SAARCHEM
Iron tetraaminophthalocyanine(II)[a]	—	—
Nitric acid	65.0	A C E
Ortho-Phosphoric acid	85.0	SAARCHEM
Octa(hydroxyethylthio)phthalocyaninatoiron(II)[a]		—
Potassium chloride	99.0	RADCHEM
Potassium ferrocyanide	98.0	B.O. Jones LTD
Potassium ferricyanide	98.0	Bio-zone chemicals
Potassium thiocyanate	—[b]	A C E
Single-walled carbon nanotubes	70.0	Aldrich
Sodiumdihydrogenphosphate-1-hydrate	99.0	MERCK
Sodium hydroxide	98.0	Bio-zone chemicals
di-Sodiumhydrogenphosphate	98.0	MERCK
Sulphuric acid	98.0	BDH

[a] used as received
[b] purity not specified

2.2.1. Functionalization of carbon nanotubes

Purification method described by Smalley *et al*. [1], was used to functionalize the carbon nanotubes. Functionalisation strategy involves multistep processes to yield SWCNTs with carboxylic acid functional groups ready for further chemistry (SWCNT-COOH). The multistep process begins with 24 hr reflux in 2.6 mol.l^{-1} of 65% nitric acid. After cooling, the mixture was centrifuged at 3000 rpm leaving black sediment at the bottom of the centrifuge bottles and a clear brownish-yellow supernatant which is decanted off. The sediment still contained substantial trapped acid which is removed by repeatedly washing the sediment with deionized water. This step was followed by a 24 hr sonication at 40°C in a mixture of 3:1 H_2SO_4 and HNO_3. Again the mixture was washed by means of centrifuge and dried at 30^{o}C overnight. Finally the SWCNT-COOHs were centrifuged in a mixture of 4:1 ratio H_2SO_4 and H_2O_2, washed with deionised water and monitor pH every after wash using indicator sticks until the solution's pH approaches 7.0, filtered and dried at 30^{o}C overnight. All experiments were performed at 25±1 °C.

2.3. Instrumentation

Voltammetric and amperommetric measurements were carried out using Advanced Electrochemical System, Autolab potentiostat PGSTAT 100/30 (Eco Chemie, Utretch, The Netherlands) driven by the General Purpose Electrochemical Systems data processing software (GPES, software version 4.9) equiped with a three electrode set-up consisting of either bare gold electrode (r = 0.8 mm, BAS) or the same gold electrode modified with the investigated SAMs, as working electrode, Ag|AgCl wire as pseudo reference electrode and platinum wire as counter electrode. Square wave parameters were: step potential 5 mV; equilibration time 5 sec, amplitude 25 mV at a frequency of 15 Hz. Electrochemical impedance spectroscopy (EIS) measurements were performed with Autolab Frequency Response Analyser (FRA) software between 10 kHz and 10 mHz using a 5 mV rms sinusoidal modulation in phosphate buffer solutions of different pH values of 1 mM of $K_4Fe(CN)_6$ and 1 mM $K_3Fe(CN)_6$ (1:1) mixture containing 0.1 M KCl at the $E_{1/2}$ of the $[Fe(CN)_6]^{3-/4-}$ (0.1 V vs Ag|AgCl). Solutions were deoxygenated by a stream of high purity nitrogen for at least 5 min before running the experiment and the solution was protected from air by a blanket of nitrogen during the experiment. Using the $[Fe(CN)_6]^{3-/4-}$ reversible electrochemistry at scan rates ranging from 0.01 to 0.20 Vs^{-1} and employing the Randles

Sevčik theory [2,3], the electrochemical roughness factor of the gold electrode (i.e. ratio o fthe real ($0.027cm^2$) to geometric ($0.020cm^2$) used for this report was determined to be *ca.* 1.34. Before electrochemical examination of each of the modified electrode, the electrode was first pretreated by repetitive cycling (20 scans) in 0.5 M H_2SO_4 until a reproducible scan was obtained.

A BENCHTOP, 420A (LABOTEC) pH meter was used for pH measurements. Ultra pure water of resistivity 18.2 MΩ.cm was obtained from a Milli-Q Water System (Millipore Corporation, Bedford, MA, USA) and was used throughout for the preparation of solutions. Ultrasonic bath (INTEGRAL SYSTEMS) was used for sonication.

Surface images were acquired with atomic force microscopy (AFM) 5100 System (Agilent Technologies, USA) using AC mode AFM scanner interfaced with a PicoScan 5.0 controller. Silicon type PPP-NCH-20 (Nanosensors®) of thickness 4.0±1.0 μm, length 125±10 μm, width 30±7.5 μm, spring constants 10-130 $N\ m^{-1}$, resonant frequencies of 204–497 kHz and tip height of 10-15 μm were used. All images were taken in air at room temperature in anti-vibration chamber. Gold coated glass was cleaned by placing the glass in pinraha solution for 2 min, then rinsed with Millipore water, dried with air nitrogen and immediately immersed in desired solution to form SAM. After Sam formation the electrode was then rinsed with Millipore water followed by ethanol and dried in nitrogen and placed in a sample chamber for scanning. Field emission electron microscopy (FESEM) images were obtained from JOL JSM 5800 LV (Japan). Morphological analyses of the different SAMs were carried out and viewed at an accelerating voltage of 5 kV and using the lowest beam current in order to avoid sample damage. Small amounts of sample material were transferred into a test tube. About 5ml of ethanol were added to the test tube which was then placed in an ultrasonic bath (bramsonic bath 5200) for about 30 sec to separate the sample particle and produce a suspension of fine particle. Small amounts of the suspension were extracted with 2 mL disposable polyethylene Pasteur pipette and transferred onto a conducting adhesive carbon tab (12 mm diameter) which were attached to an aluminium stub. The alcohol was allowed to evaporate in an oven at 30^{o}C.

X-ray photoelectron spectroscopy (XPS) measurements were carried out using a physical electronics model 5400 spectrometer system at a vacuum of abour 10^{-8} Torr, with monochromatic Mg Kα radiation at 1253.6 eV. Take-off angle of 20, 45 and 80^{o} were used for the studies. All spectra were averages of 20 scans of 60 sec duration. The binding energies for all thin film samples were referenced to the 1s carbon peak at 284.5 eV. The experiments were performed with gold-coated glass slides as substrates for the SAMs.

2.4. Electrode modification procedure

2.4.1. Electrode pre-treatment

The gold electrodes used were first cleaned following the conventional procedure [4,5]. For each experiment the electrode was polished in an aqueous slurry of alumina (<10 μm) on a SiC-emery paper (type 2400 grit), and then to a mirror finish on a Buehler felt pad. The electrode was then subjected to ultrasonic vibration in absolute ethanol to remove residual alumina particles that might be trapped at the surface. Finally the electrode was etched for about 2 min in a hot 'Piranha' solution (1:3 (v/v) 30% H_2O_2 and concentrated H_2SO_4) for about 1 min, and then rinsed with copious amounts of ultrapure Millipore water followed by ethanol. This stage was necessary to remove organic contaminants and was followed by thorough rinsing with distilled water. The cleanliness of the bare electrode surface was finally established by placing it in 0.5 M H_2SO_4 and scanning the potential between −0.5 and 1.5 V (vs Ag|AgCl wire) at a scan rate of 0.05 Vs^{-1} until a reproducible scan was obtained.

***CAUTION**: Piranha solution must be handled with care as it reacts violently with organic materials and can explode when stored in closed containers*.

2.4.2. Self-assembling technique

2.4.2.1 SWCNT-phthalocyanine based electrode

The formation of reproducible self-assembled monolayers (SAM) requires a reproducible surface. Following the pre-treatment, the electrode was placed in nitrogen-saturated 10 mM solutions of cysteamine hydrochloride to allow the Au-Cys electrode to form for a desired period of time. Then the electrode was thoroughly rinsed with absolute ethanol solution before reacting with SWCNT. A 3 mg of acid treated SWCNT was first dispersed in 1 ml pure dry DMF with 0.5 mg DCC (2.4μmol) to convert the –COOH groups at the ends of the SWCNT into active carbodiimide esters. The surface condensation of the Au-Cys electrode was achieved by placing the electrode in the black solution of SWCNT/DCC/DMF for 24 hr. The condensation of the –COOH functional groups of the SWCNT with the $-NH_2$ groups of the Cys SAM resulted in the formation of the amide bonds [6-8].

The FeOHETPc was attached to the free DCC-activated ends of the SWCNT by placing the Au-Cys-SWCNT electrode in a DMF solution containing ~ 1.0×10^{-3} M FeOHETPc for 25 hr. The surface of the Au-Cys-SWCNT electrode is expected to contain some active carbodiimide esters that would be attacked by the hydroxyl functional groups of the FeOHETPc to generate the SWCNT-FeOHETPc via ester bonds, releasing dicyclohexylurea (DCU) in the deposition solution [9]. Facile esterification of the –OH functionality through carbodiimide couplings is well documented [10-12] and more recently, in selective esterification of the -OH of the mercarptoethanol functionality with the free -COOH of the SWCNT SAM. The experiments were carried out using nitrogen purged solutions of either H_2SO_4 for pretreatment or analyte in phosphate buffer (pH 4.8) using gold electrode modified with the complexes as the working electrodes while Ag|AgCl and platinum electrodes were employed as reference and counter electrodes, respectively.

2.4.2.2 SWCNT-ferrocene based electrodes

Self-assembled monolayers of alkanethiol capped with carboxylated ferrocene and single-walled carbon nanotubes were prepared on gold surfaces. Following the formation of Au-Cys electrode for 18 hr, the electrode was rinsed with ultrapure water and dried with nitrogen. The formation of Au-Cys-FDCA and Au-Cys-FMCA followed after placing the Au-Cys electrode in a 1ml DMF solution containing 3mg FDCA or FMCA for 48 hr, respectively.

The Au-Cys-SWCNT/FDCA electrode was obtained simply by placing Au-Cys in DMF solution containing equimolar mixture of SWCNT and FDCA and 0.5 mg DCC for 48 hr. This same method was used to prepare Au-Cys-SWCNT/FMCA. Upon removal from the deposition solution, prior to electrochemical experiments, the electrode was thoroughly rinsed with millipore water and dried in a nitrogen atmosphere.

Prior to electrochemical experiments, the modified electrodes were conditioned by placing in 0.5 M H_2SO_4 and repetitively scanned between −0.5 and 0.6 V (vs Ag|AgCl) potential window at a scan rate of 25 mVs^{-1} until a constant scan was obtained.

2.4.2.3 Nano-gold indium tin oxide electrode

The gold nanoparticles were deposited on indium tin oxide surface by the method described by Kambayashi *et al*. [13]. The electrodes were kindly donated by Prof. Munetaka Oyama of the chemistry department of Kyoto University, Japan. The SEM images of these electrodes, (see Figure 2.1), shows the attached gold nanoparticles in which the SAM was anchored. Formation of the SAM follows the described procedure (see chapter 3) where ITO-nanoAu was deposited to a nitrogen-saturated absolute ethanol solution of cysteamine for 4 hr. After rinsing, the electrode was immediately placed into a mixture of SWCNT/FDCA for 2 hr to form nanoAu-Cys-SWCNT/FDCA electrode and the electrode was ready for use.

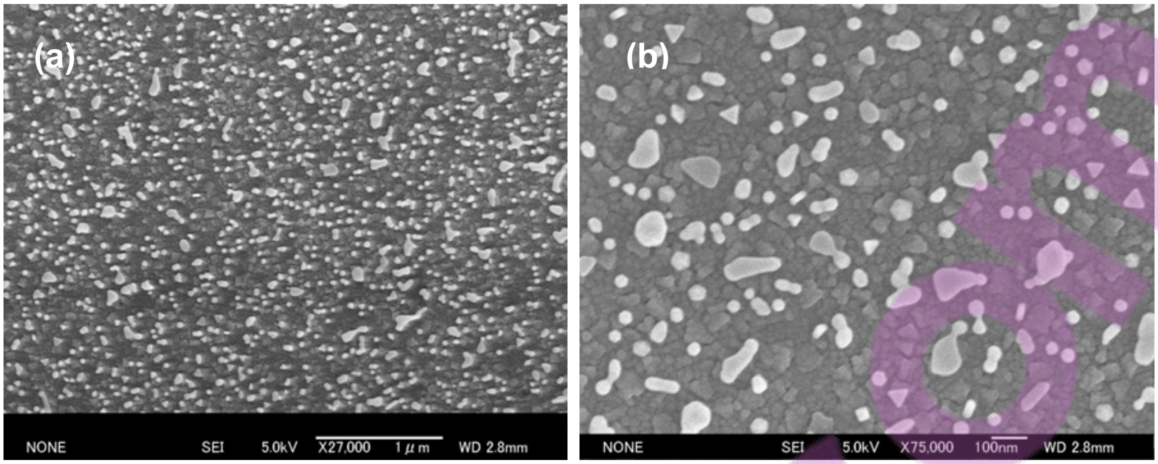

Figure 2.1: FESEM images of the nanogold modified ITO electrode (a) 1 μm magnification and (b) 100 nm magnification. (Duplicated with permission from Oyama and co-workers [13]).

REFERENCES

1. R. E. Smalley, A. G. Rinzler, J. Liu, H. Dai, P. Nikolaev, C. B. Huffman, F. J. Rodriguez-Macias, P.J. Boul, A. H. Lu, D. Heymann, D. T. Colbert, R. S. Lee, J. E. Fischer, A. M. Rao, P. C. klund, Appl. Phys. A 67 (1998) 29.
2. A. J. Bard, L. R. Faulkner, Electrochemical Methods: Fundamentals and Applications, 2nd ed., John Wiley & Sons, Hoboken, NJ. 2001
3. H. O. Finklea in R. A. Meyers, Eds., *Encyclopaedia of Analytical Chemistry:Applications, Theory and Instrumentations*, Vol. 11, Wiley, Chichester (2000) 10090.
4. P. Diao, Z. Liu, J. Phys. Chem. B. 109 (2005) 20905.
5. Z. F. Liu, Z. Y. Shen, T. Zhu, S. F. Huo, L. Z. Ying, Z. J. Shi and Z. N. Gu, Langmuir 16 (2000) 3569.
6. J. J. Gooding, R. Wibowo, J. Liu, W. Yang, D. Losic, S. Orbons, F. J. Meams, J.G. Shapter, D. B. Hibbert, *J. Am. Chem. Soc.* 125 (2003) 9006.
7. F. Patolsky, Y. Weizmann, I. Willner, *Angew. Chem. Int*. Ed. 43 (2004) 2113.
8. L. Sheeney-Haj-Ichia, B. Basnar, I. Willner, *Angew. Chem. Int*. d. 44 (2005) 78.

9. P. Y. Bruice, *Organic Chemistry*, fiftth ed., Person Prentice Hall, New Jersey, chapter 22 (2007) 1041.

10. B. Neiss, W. Steglich, *Org. Synth*. 63 (1985) 183.

11. R. Shelkov, M. Nahmany, A. Melman, *Org. Biomol. Chem*. 2 (2004) 397.

12. J. Yu, J. G. Shapter, J. S. Quinton, M. R. Johnston, D. A. Beattie, *Phys.Chem.Chem.Phys.* 9 (2007) 510.

13. J. Zhang, M. Kambayashi, M. Oyama, *Electrochem. Commun.* 2004, 6, 683.

SECTION B

CHAPTER 3

RESULTS AND DISCUSSION*,[1]

SPECTROSCOPIC , MICROSCOPIC AND ELECTROCHEMICAL PROPERTIES OF IRON-PHTHALOCYANINE SINGLE-WALLED CARBON NANOTUBE BASED ELECTRODES

---

*Chapters 3 – 6 comprise the results and discussion.

[1] Five publications resulted from work presented in these chapters and they are not referenced further in this thesis.

3.1 SAM formation strategies

The stepwise self-assembly strategy employed in the preparation of the main electrodes is schematically represented in the Scheme 3.1 following the established procedure. For simplicity, the gold electrodes modified with the cysteamine is represented as Au-Cys, the Au-Cys integrated with single-walled carbon nanotubes is represented as Au-Cys-SWCNT, while the Au-Cys-SWCNT integrated with the FeOHETPc as the Au-Cys-SWCNT-FeOHETPc.

Upon acid treatment, single-walled carbon nanotubes bear most of the carboxylic acid groups which are found at the end of these tubes, the edge-plane and or defect sites of the tubes. Few appearance of the functional groups at the defect sites of the walls are also possible as depicted in scheme 3.1. The fabrication of Au-Cys-SWCNT-FeTAPc followed a similar protocol. Also, the Au-FeOHETPc was prepared as reported by Ozoemena *et al.* [1], while the Au-FeTAPc electrode was fabricated using the method described by Somashekarappa *et al.* [2].

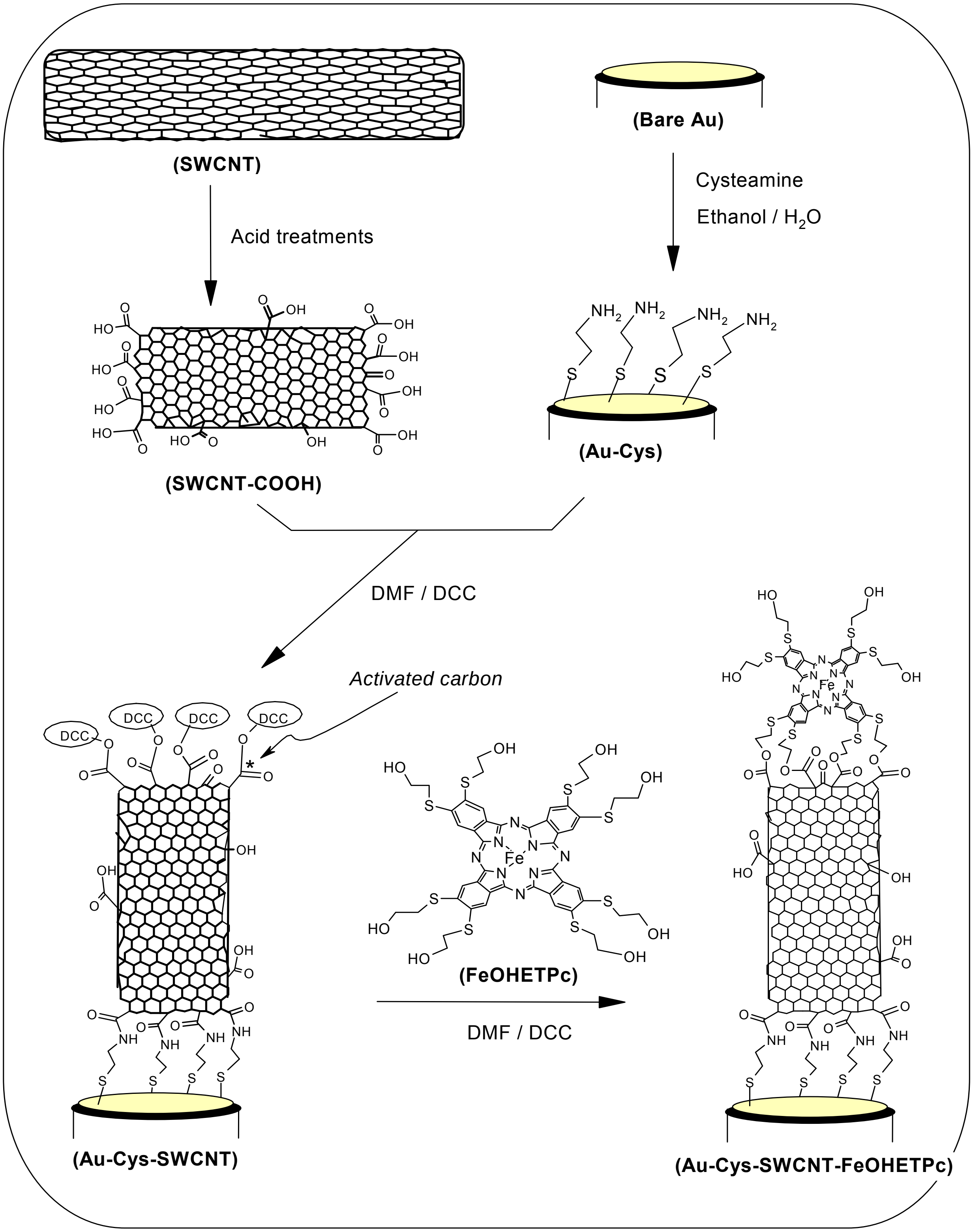

Scheme 3.1: Schematic representation of the self-assembly processes of the SWCNT and SWCNT-FeOHETPc on gold electrode.

3.2 Atomic force microscopy characterization

AFM studies were conducted to give an insight to the surface morphologies of the formed SAMs and figure 3.1 exemplifies the 3-D AFM images of the Au-Cys (a), Au-Cy-SWCNT (b) and Au-Cys-SWCNT-FeOHETPc (c), indicating that the SAMs assume perpedincular orientations on the gold surfaces.

The needle-like protrusions are in agreement with several literature reports for SWCNT-based SAMs [3-5]. If we realise that as many as eight carboxyl groups might be present at each end of a ~1.3 nm-diameter SWCNT [4], it is reasonable therefore to assume that about eight amide bonds could be generated between each SWCNT and the modified gold surface, hence explaining the preferred vertical alignment of the SWCNT onto the gold surface.

The strong van der Waal's attractive forces existing between carbon nanotubes should make SWCNTs assemble as bundles and not as individual. This is even more possible given that Au-Cys SAM (Figure 3.1(a)) also exist as bundles because of this attractive force. According to literature [3], SWCNTs prefer to assemble on gold surfaces as bundles of around 5 – 20 tubes. It is apparent from the images shown in figure 3.1(a) that the aligned SWCNTs did not assemble on the gold surface as individual tubes but as bundles.

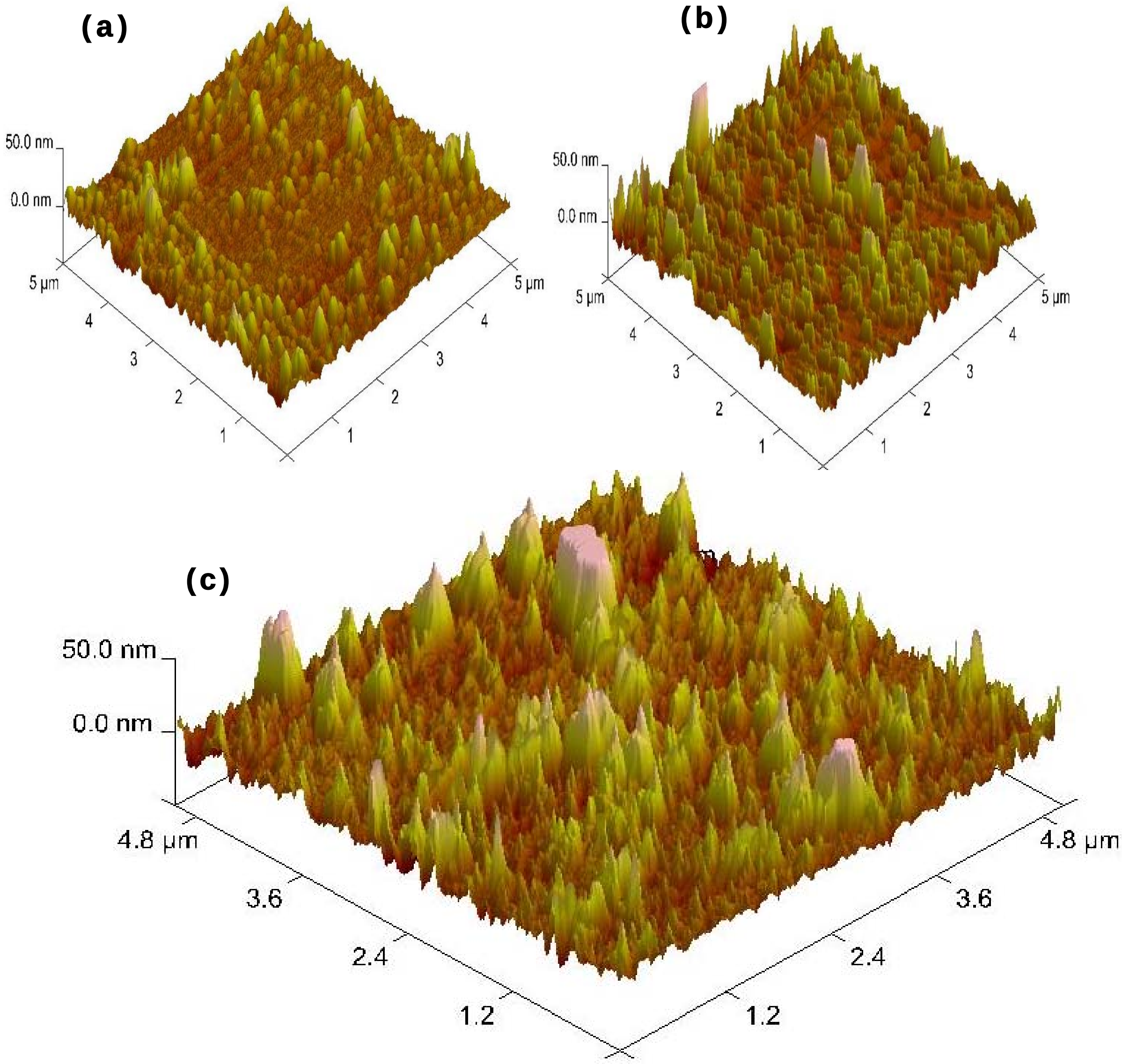

Figure 3.1: Typical AFM images of aligned (a) Cys, (b) Cys-SWCNT and (c) Cys-SWCNT-FeOHETPc modified gold surfaces.

Although, the 'cut' SWCNTs were not fractionalized before being immobilized onto the gold electrodes, it is interesting to observe that the heights of the vertically aligned SWCNT bundles still lie in the ~ 30

– 50 nm range, as observed in previous reports [3-5]. The AFM images obtained on subsequent coupling of the FeOHETPc onto the Au-Cys-SWCNT surface (reaction time 25 hr) (Figure 3.1(b)) expectedly shows similar bundled shapes of the Au-Cys-SWCNT. However, unlike in figure 3.1(b), the FeOHETPc showed more defined needle-like protrusions, with slight increase (*ca*. 2 nm) in the average bundle lengths, suggesting that the FeOHETPc species are linked to the ends of the SWCNTs (few binding on the defect sites of the sidewalls of the SWCNTs may not be completely ruled out). Li *et al.* [6] predicted from computer modelling that MPc containing eight peripheral substituents, R, (R = $O(CH_2)_4CH_3$) has a diameter of 21 Å. In this work, where R = $S(CH_2)_2OH$, it means that the diameter of the FeOHETPc (if modelled as a circle) with standing (vertical) orientation as depicted in Scheme 1 may be assumed to be about 20 Å (i.e., ~ 2 nm). This value certainly explains the insignificant change in the length of Au-Cys-SWCNT-FeOHETPc compared to that of the Au-Cys-SWCNT shown by the AFM experiments.

3.3 XPS characterization

Having confirmed the formation of the SAMs on gold surfaces by AFM experiments, XPS was carried out to give some insights into the elemental compositional details of the self-assembled nanostructures. Figure 3.2 shows the survey X-ray photoelectron spectra for the full (Figure 3.2(a)) and the expanded portions of regions of most interests; sulphur (2p) (Figure3.2(b)), nitrogen (1s) (Figure 3.2(c) and carbon (1s) (Figure 3.2(d)) for the bare Au (i), Au-Cys (ii), Au-Cys-SWCNT (iii), and Au-Cys-SWCNT-FeOHETPc (iv) electrodes.

It is well recognized in XPS [6,7] that oxygen and carbon are almost always present on gold surfaces due to contaminations, the most reliable indicators for the formation of the SAMs studied here are the peaks due to sulphur and nitrogen, however, the carbon peaks give some insights into the presence of the CO and COOH. Calibrating the binding energies using the normal carbon 1s peak of adventitious carbon at 284.5 eV, the sulphur (2p) peak for both Au-Cys and Au-Cys-SWCNT appeared at 161.5 eV, assigned to the normal Au-S bond [6-12], while that for the Au-Cys-SWCNT-FeOHETPc was observed at 162.5 eV.

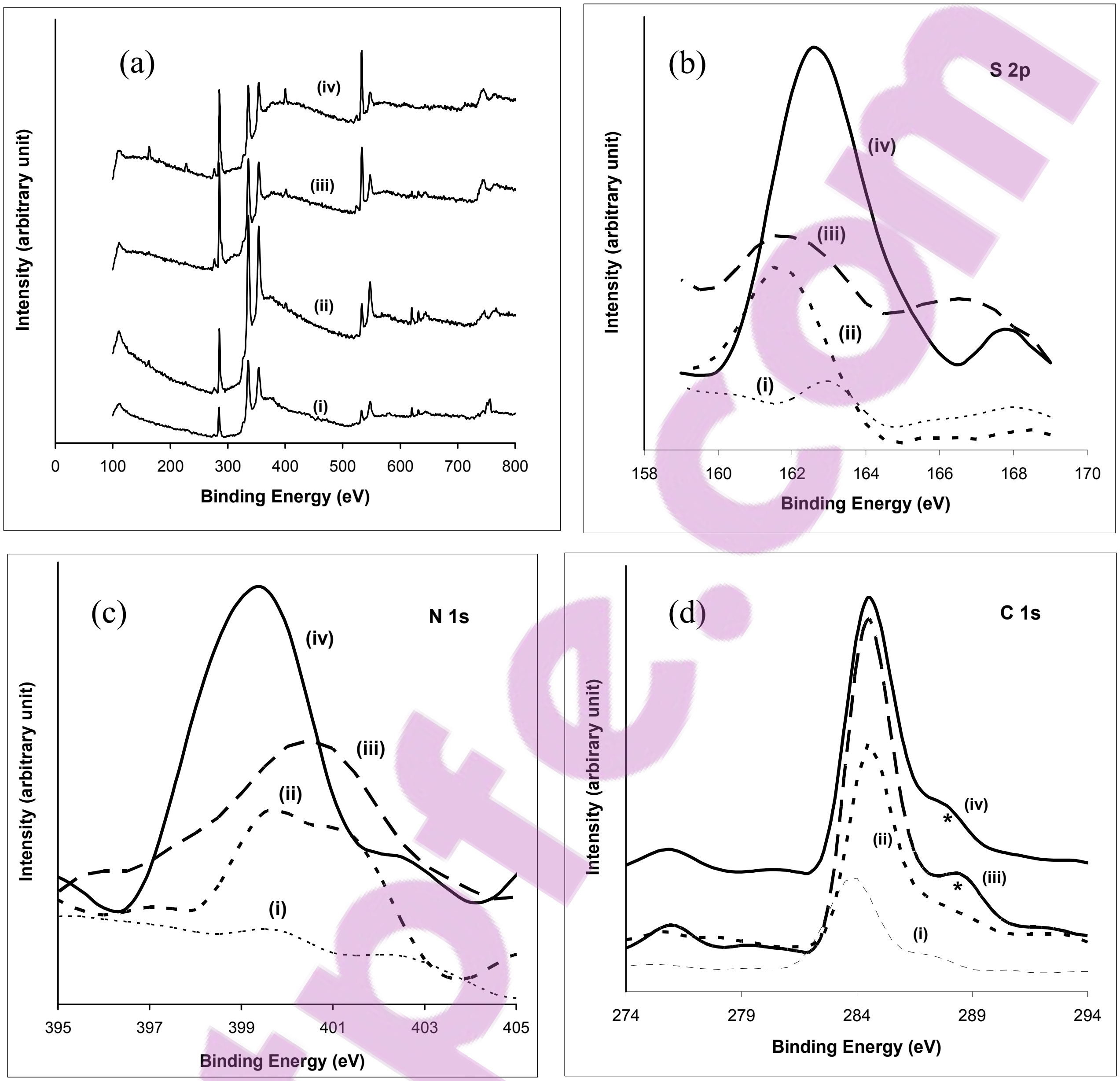

Figure 3.2: Survey X-ray photoelectron spectra for the full (a) and the expanded regions for the sulphur (b), nitrogen (c) and carbon (d) for the bare Au (i), Au-Cys (ii), Au-Cys-SWCNT (iii), and Au-Cys-SWCNT-FeOHETPc (iv) electrodes.

The 1 eV shift of the sulphur (2p) peak of the Au-Cys-SWCNT-FeOHETPc with increased peak intensity (Figure 3.2(b) (iv)) compared to those of the other SAMs suggest the presence of both gold bound (Au-S) and the sulphur of the peripheral substituents (-S$(CH_2)_2$OH) of the FeOHETPc species. The presence of these two types of sulphur for the Au-Cys-SWCNT-FeOHETPc was confirmed by a multiplexing experiment which revealed two peaks at ~161.5 and 162.7 eV for the Au-Cys-SWCNT-FeOHETPc and one peak at ~161.5 eV for the Au-Cys SAM. The cysteamine SAM showed two components for the nitrogen (1s) peak at 399.5 and 401 eV, which is in agreement with literature for cysteamine SAMs [9]. The nitrogen (1s) peak for the phthalocyanine is known to occur at either 398 or 400 eV [10], thus the appearance of sharp nitrogen (1s) peak for the FeOHETPc at 399.5 eV confirms the attachment of the FeOHETPc on the SWCNT. The nitrogen (1s) peak of the CONH for the SWCNT was observed at 400.5 eV. The different binding energies for the nitrogen (1s) of the different SAMs is indicative of the different environments where the nitrogen atoms occur. As would be expected, in terms of peak intensity and binding energy width, SWCNT exhibited relatively high concentrations of carbon Figure 3.2(d) (iii) and oxygen (not shown). Also, unlike the cysteamine SAM (Figure 3.2(d) (ii)), the SWCNT (Figure 3.2(d) (iii)) and FeOHETPc (Figure 3.2(d) (iv)) SAMs exhibited shoulders in the binding energy regions of 287.5 and 289.5 eV (see asterisked), attributed to the carbonyl and carboxylic groups [10,11] and suggesting the formation of the amide and ester bonds during the self-assembly. The Au-Cys-SWCNT-FeOHETPc exhibited a weak peak at the binding energy of ~ 718 eV (not shown) corresponding to the Fe(II) peak (Fe, $2p^{3/2}$) [12].

3.4 Cyclic voltammetric characterization

3.4.1 Pretreatment of SWCNT-FeOHETPc

Unless otherwise stated, adsorption times of 18, 24 and 48 hr were adopted for the formation of the SAMs of Cys, SWCNT and FeOHETPc, respectively. It was dicovered that these SAMs could be formed within 8hr adsorption period; however, longer adsorption time was employed to permit for enhanced coverage of the SAMs on gold surface. To avoid possible oxidative desorption of the SAMs at high positive potential > 1.0 V vs Ag|AgCl, all voltammetric studies were restricted to the -0.20 to 1.0 V potential window. Previous studies [13,14] have shown that the first cyclic voltammetric scan of SAMs, especially the MPc SAM, sometimes differ from subsequent scans.

Figure 3.3 presents cyclic voltammetric profiles of the various electrodes studied compared with the bare Au in 0.5M H_2SO_4. The modified electrode exhibited strong electrochemical stability, confirmation proved by reproducibility in 0.5M H_2SO_4 solution during repetitive scanning. Such stability is important for electrochemical studies and application of surface-confined thin films in aqueous solutions.

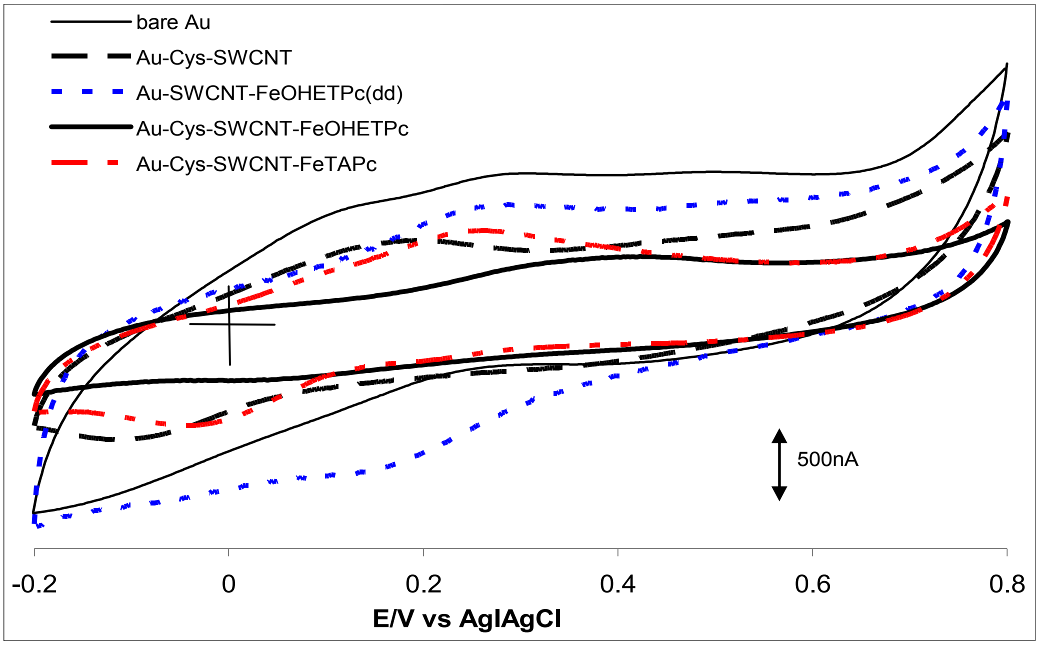

Figure 3.3: Cyclic voltammetric profile of the various electrodes studied, compared with the bare Au in 0.5 M H_2SO_4 at the scan rate of 25 mV s-1. Other scans heve been excluded for clarity.

The redox couple observed for the Au-Cys-SWCNT is attributed to the four-electron process [15]. From the several reports on the electrochemistry of surface-confined phthalocyaninatoiron(II) complexes [16-18], the peaks at the +0.23V and +0.02V at the A-Cys-SWCNT-FeOHETPc electrodes were attribute to the Fe(III)/Fe(II) redox process. For the SWCNT and SWCNT-FeOHETPc films, the peak separations are greater than the ideal zero volts expected for surface-immobilized species which may be attributed to the kinetic limitations or some electrostatic interactions of the molecules in the films.

3.4.2 Interfacial capacitance

The interfacial capacitances of the films were estimated from the non-Faradaic region of the CVs (~ +0.6V vs Ag|AgCl)) using the equation (3.1) [18,19]:

$$C_T = \frac{I_{ch}}{\nu A} \tag{3.1}$$

where C_T= total capacitance, I_{ch} = charging current, v = scan rates and A is the area of the electrode. The capacitances estimated from Figure 3.3 were 1.4 μFcm^{-2} (bare gold), 0.6 μFcm^{-2} (Au-Cys), 0.7 μFcm^{-2} (Au-Cys-SWCNT), 0.6 μFcm^{-2} (Au-Cys-SWCNT-FeOHETPc), 1.2 μFcm^{-2} (Au-SWCNT$_{dd}$-FeOHETPc), 0.7 μFcm^{-2} (Au-Cys-SWCNT-FeOHETPc$_{(no\ DCC),}$) 0.6 μFcm^{-2} (Au-Cys-FeOHETPc), and 0.5 μFcm^{-2} (Au-FeOHETPc). Au-SWCNT$_{dd}$-FeOHETPc obtained by first preparing a nanotube bed by drop-coating SWCNT gave good FeOHETPc electrochemistry but with huge capacitive current. Various reports [20-22] have indicated that the electrochemistry of small redox-active molecules and proteins were observed through hydrophobic walls of CNTs. Also phthalocyanine complexes such as tetra-*tert*-butylphthalocyanines [23], FePc [24] and CoTAPc [25] have been observe to strongly adsorb onto CNT via π-π interactions. Thus, the observed electrochemistry of FeOHETPc on SWCNT bed electrode as seen in figure 3.3 should perhaps not be surprising as the bed position could easily allow direct association of the phthalocyanine ring of the FeOHETPc with the walls of the SWCNT via π-π interaction (although some covalent interactions cannot be completely ruled out). Note also that some electrochemistry of the FeOHETPc is observed at the Au-Cys-SWCNT-FeOHETPc in the absence of DCC, which is necessary for covalent linkages of the SWCNT and FeOHETPc. This indicates that there is significant non-specific adsorptions of the FeOHETPc on the SWCNT, the same explanation of close π-π interaction as for the bed position could also hold for this behaviour. The relatively smaller capacitive current of the Au-Cys-SWCNT-FeOHETPc, coupled to the faster electron transfer kinetics (further discussed in section 3.5) is advantageous to electroanalytical applications and underscores the preference of the aligned nanotube compared to electrode without DCC or its bed form on gold electrode.

The results obtained here is consistent with literature precedents where the capacitance of bare Au is usually more than order of maginitude higher than the typical capacitances for most alkanethiol SAMs [18,19]. The marked decreased in the capacitive charging currents of the bare gold electrode by the modifying species is characteristic of compact and less defective films capable of suppressing electrolyte ions from penetrating into the film. The ability of the films to suppress ion penetration increases with increasing hydrophobicity of the film head groups (which in this study are the –NH_2 for cysteamine; –COOH for the SWCNT, and –OH for the FeOHETPc). Based on the p*Ka* of the head groups of the species used in this work mercaptoethanol 9.5; [26] cysteamine (10.5) [26,27] and benzyl species substituted with carboxylic group (in the 4.0–5.0 [28,29]), it suggests that their ion suppression ability should follow the observed trend of Cysteamine ≈ FeOHETPc > SWCNT. The capacitance values of various SWCNT-modified electrodes obtained by dip-coating were reported to fall in the 159–710 $\mu F/cm^2$ range [30-33]. The difference between these data and the results from this thesis is that dip-coated SWCNTs give much higher coverage compared to the self-assembly method [34]. Thus, the high capacitance for the Au-SWCNT-FeOHETPc obtained in this work is attributed to the higher amount of SWCNT on the Au obtained by drop-dry method. Also, these results differ from reports in 0.01 M PBS pH 4.4 or 1.0 M Na_2SO_4 pH 4.0 [13,14] where the SAMs exhibited higher capacitive currents than the bare Au. This deviation may be associated with the working electrolytes (0.5 M H_2SO_4) used in this study. This prompted us to carry out all the studies in this electrolyte conditions. Advantageously, this electrolyte condition also activates the central Fe(II)/Fe(III) redox process of the attached FeOHETPc species compared to PBS pH 4.4.

3.4.3 Surface coverage

The amounts of the SAM molecules on the gold surface (Γ) were estimated from the anodic charges of the CV profiles in 0.5 M H_2SO_4 (Figure 3.3) using the expression [18,19,35]:

$$\Gamma_{SAM} = \frac{Q}{nFA} = \frac{\int Idt}{nFA} \tag{3.2}$$

where Q is the background-corrected charge under the cathodic or anodic waves, n = number of electrons involved in the redox process, F is the Faraday constant (96485 C mol^{-1}), and A is the experimentally determined area of the electrode. Assuming a four-electron for the Au-Cys-SWCNT redox process, [15] and one-electron process for the other electrodes, the surface concentrations were approximately as 6.8 x 10^{-10} mol cm^{-2} (*ca* 4.1 x 10^{14} molecules cm^{-2} or ~ 24 Å^2 per molecule) for the Au-Cys, 1.4 x 10^{-10} mol cm^{-2} (*ca*. 8.2 x 10^{13} particles cm^{-2} ≈ 122 Å^2 per particle) for the Au-Cys-SWCNT, and 7.0 x 10^{-10} mol cm^{-2} (*ca* 4.2 x 10^{14} molecules cm^{-2} or ~ 24 Å^2 per molecule) for the Au-Cys-SWCNT-FeOHETPc. The values are of similar magnitudes as those reported in the literature for the Au-Cys [3,4], Au-Cys-SWCNT [3,4], and Au-FeOHETPc [13], confirming monolayer coverage [18,19]. The similarity in surface coverages suggests that the observed electrochemistry was due to the SWCNT attached to the cysteamine, and FeOHETPc attached to the ends of the SWCNTs. The projected area of the FeOHETPc molecule (assuming a diameter of ~ 20 $Å^2$ as discussed in the AFM results above [6]) is ~315 $Å^2$, implying that for this MPc to lie flat on the ends of the SWCNTs, then its coverage should work out to be ~ 3.2 $x10^{13}$ particles cm^{-2}, i.e. ~ 5.3 $x10^{-11}$ mol cm^{-2}. Thus, the high surface coverage for the FeOHETPc is a clear confirmation of a standing position rather than flat orientation, corroborating the AFM results for the FeOHETPc. Interestingly, FeOHETPc is also known to prefer perpendicular orientation when adsorbed on a gold surface as a SAM [13]. Similarly, the cross sectional area for a single SWCNT of diameter of ~ 1.3 nm [4] should be *ca*. (1.33 – 1.54) x 10^{-14} cm^{-2}, meaning that each SWCNT particle occupies an area of ~133 – 154 $Å^2$, which is in close correlation with the surface coverage (~122 $Å^2$) obtained in this work. This result is consistent with the AFM results which showed that these SAMs lie normal to the gold surface. The surface concentrations shown by other FeOHETPc-based electrodes also indicate horizontal rather than vertical orientations. The coordination of Cys with FeOHETPc could occur via axial ligation of the $-NH_2$ with the central Fe [35] and/or electrostatic attraction. Axial ligation (flat orientation) is excluded as the surface coverage would have been smaller than the observed value. For the other electrodes, the surface concentrations were estimated as 4.2 x 10^{-10} mol cm^{-2} (Au-FeOHETPc, 1.2 x 10^{-9} mol cm^{-2} (Au-Cys-SWCNT-FeOHETPc$_{(no\ DCC)}$) and 4.5 x 10^{-9} mol cm^{-2} for the Au-SWCNT$_{dd}$-FeOHETPc. The coverage of the randomly dispersed nanotubes or the bed form (Au-SWCNT$_{dd}$-FeOHETPc) is about 40 times greater than those obtained by the aligned nanotubes (Au-Cys-SWCNT-FeOHETPc). Surface-confined electropolymeric complexes of redox-ctive of MPc complexes give coverages in the 10^{-9} and 10^{-8} mol cm^{-2} order, thus this result suggests that the Au-SWCNT$_{dd}$-FeOHETPc could be acting like a redox polymer rather than a monolayer.

3.5 Electrochemical impedimetric characterization

3.5.1 Electron transport behaviour of the SAMs

Cyclic voltammetric and impedimetric responses of the different electrodes in aqueous solution of the outer-sphere redox probe, $[Fe(CN)_6]^{3-}/[Fe(CN)_6]^{4-}$ were compared as emplified in figure 3.4 (CV) and figure 3.5 (EIS). Impedance spectroscopy was used since it is well-recognized as a powerful diagnostic tool for providing high accuracy in measuring the electron transport properties of redox-active SAMs [37-40]. Therefore, in figure 3.5 we see the Nyquist plots which exhibit the characteristic semicircles at high frequencies and a straight line at low frequencies, corresponding to kinetic and diffusion processes, respectively.

The phase angles seen in figure 3.6(a) (i.e., –phase angle (ϕ) vs log f,) are in the range of 30 - 40°, which are less than the 90° expected of an ideal capacitive behaviour. The lower the phase angle, the lower the capacitive behaviour of the electrode hence the faster the electron transfer.

The other Bode plot illustrates the relationship between the logarithm of impedance and frequency. The slopes of the Bode plots (log Z vs log f) are approximately similar for all the electrodes (*ca*. –0.37, r^2 = 0.996) at the mid frequency region, indicative of pseudocapacitive behaviour. At high frequency regions, the slopes are almost zero, indicative of resistive behaviour at these high frequency regions.

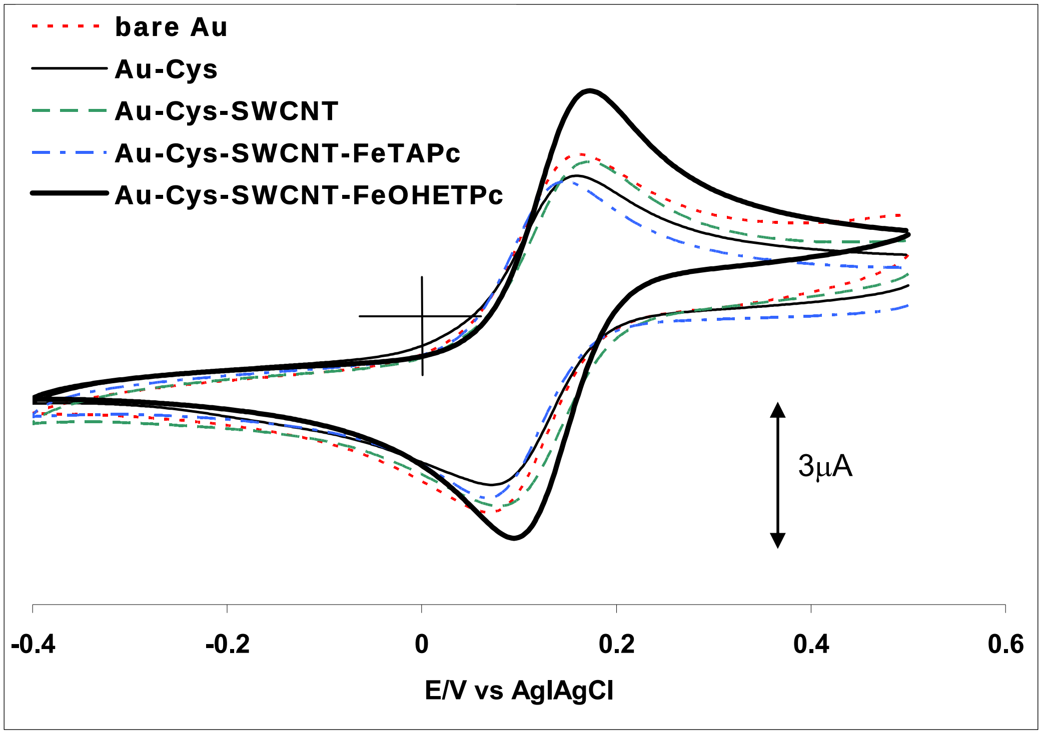

Figure 3.4: Typical cyclic volammograms of the indicated electrodes towards the reversible couple $Fe(CN)_6]^{3-}$/ $[Fe(CN)_6]^{4-}$ in 0.1 M PHS (pH 4.8). scan rate: 25 mVs^{-1}.

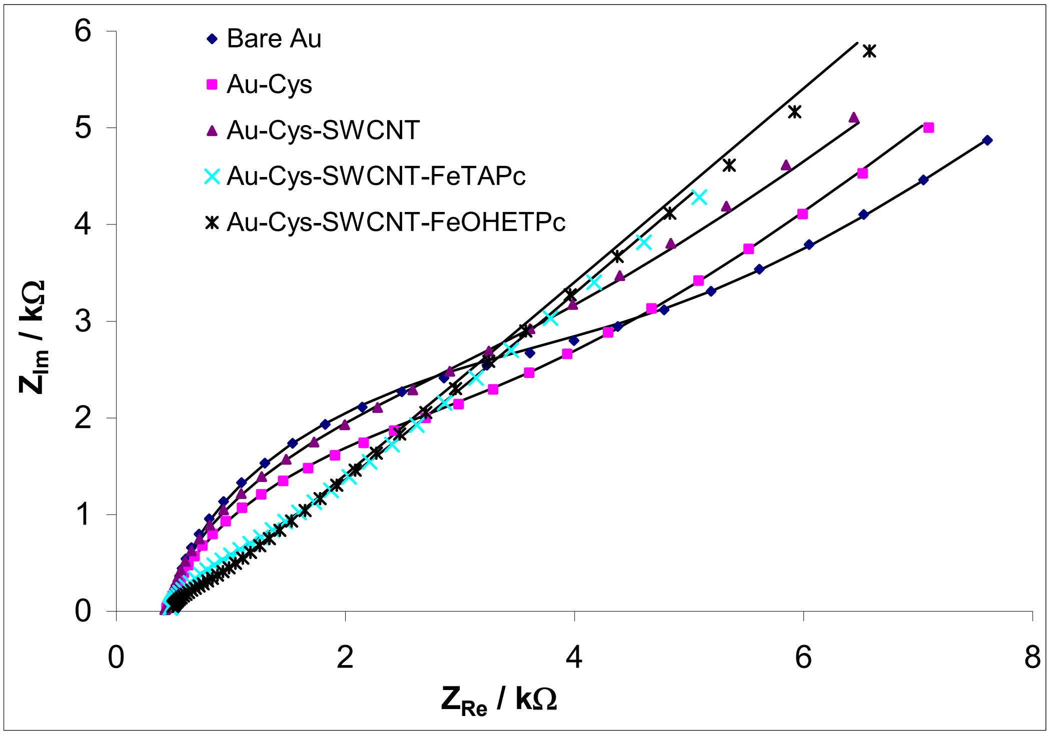

Figure 3.5: Impedance spectral responses of the indicated electrodes obtained at +0.10 V vs AgIAgCl in $Fe(CN)_6]^{3-}$/ $[Fe(CN)_6]^{4-}$ 0.1 M PBS (pH 4.8)

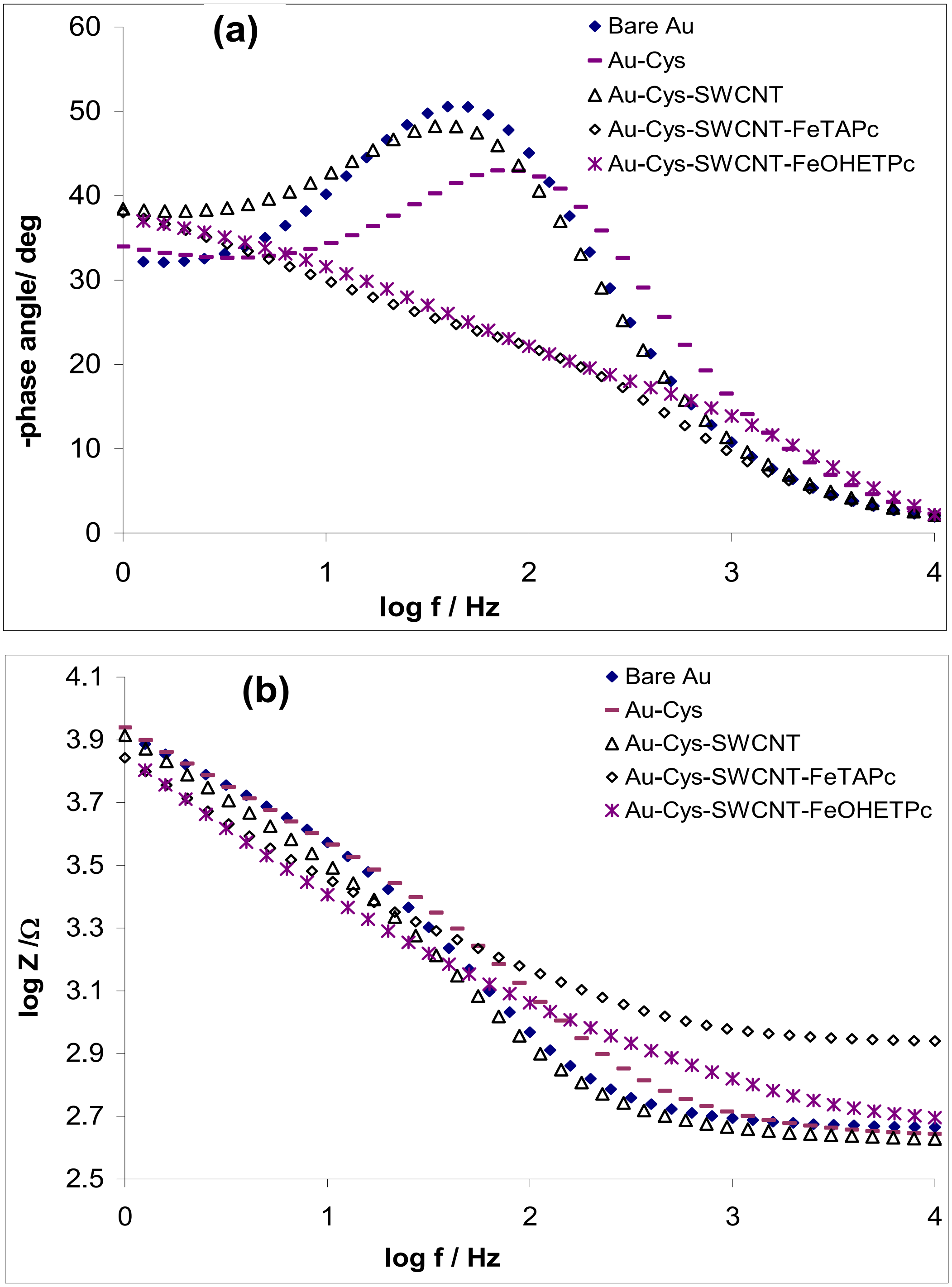

Figure 3.6: Bode plots, phase angle vs log f (a) and log Z vs log f (b),of the impedance spectra of the modified electrodes in redox probe ($[Fe(CN)_6]^{4-}$/ $[Fe(CN)_6]^{3-}$) in 0.1 M PBS solution (pH 4.8).

3.5.2 Impact of solution pH on electron transfer

The effects of solution pH and estimation of the surface *pka* values of SAM-modified electrodes are important in the theory and potential applications of the SAMs [41-46]. The *pka* of a surface-confined species is defined as the value of the pH in contact with the monolayer when half of the functional groups are ionized [46]. The *pka* of Au-Cys SAM has been reported to be ~7.6 and so was not repeated in this report. Figure 3.7 presents examples of the plots of R_{CT} vs pH for the Au-Cys-SWCNT (A) and Au-Cys-SWCNT-FeOHETPc (B) in PBS solutions of $[Fe(CN)_6]^{3-/4-}$.

The differences in the impedance spectral profiles indicate the coordination of the different SAMs with different head groups giving different surface reactions. With increasing pH, the R_{CT} values markedly increase, which could be ascribed to the increasing dissociation/deprotonation of the monolayer head groups. Each of the electrodes exhibits semicircles in the high frequency region and a Warburg line in the low frequency region even at pH $\geq$ 9.0, suggesting that semi-infinite diffusion process still occurs at this high pH.

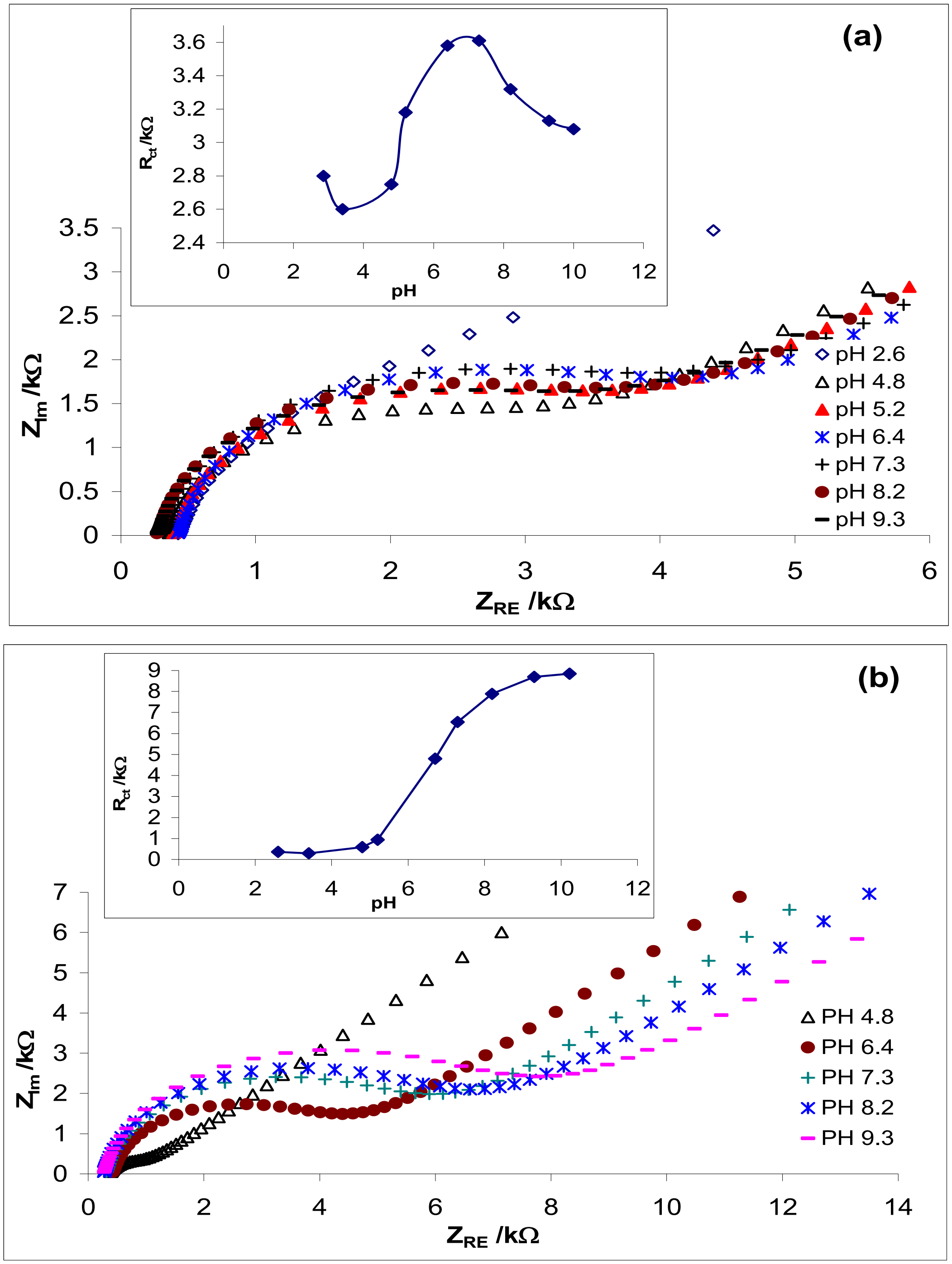

Figure 3.7: Examples of the impedimetric responses of the Au-Cys-SWCNT (a) and Au-Cys-SWCNT-FeOHETPc (b) at different pH of the $Fe(CN)_6]^{3-}/[Fe(CN)_6]^{4-}$ solutions. Insets are the corresponding plots of R_{CT} vs pH.

This behaviour should make some sense considering (i) that the solution p*Ka* values of mercaptoethanol (for the Au-Cys-SWCNT-FeOHETPc electrode) is 9.5 [26]; and (ii) that the –COOH group and other functionalities as the phenols present in acid digested SWCNTs are stabilized by the strong hydrogen bonding that could impede the facile ionization of the Au-Cys-SWCNT. The increase in the R_{CT} of the Au-Cys-SWCNT at pH $\geq$ 5 is due to the electrostatic repulsion of the anionic probe by the negative potential established at the monolayer -COOH head group. At pH $\geq$ 7.5, the electron transport slightly increases, possibly due to repulsive interations of the fully ionised neighbouring head groups that could lead to less compactness of the SAM and permit the penetration of the redox probe into the underlying electrode, a similar phenomenon that had been observed for SAMs by Jun and Beng [47]. The surface *pKa*s of the electrodes could be estimated from the midpoints of the R_{CT} vs pH plots. We estimated the surface p*Ka* for the Au-Cys-SWCNT to be *ca.* 5.5. Back and Shim [48] reported the pH-responsiveness of a single isolated SWCNT electrochemical transistor integrated with microfluidic channel under 10 mM KCl solution and found that the threshold voltage shifted with pH while its transconductance and subthreshold swing remained independent of pH. From the plot of the threshold shift (ΔV_t / V) with pH, a p*K*a value of ~ 7.6 was estimated. Given that the experimental conditions employed by these authors are widely different, it is impossible to adequately compare the findings in this present work with theirs. For example, the authors studied a single isolated SWCNT (not treated in acid conditions, meaning it has little or no -COOH) in unbuffered electrolyte with high ionic strength. It is interesting to read from the recent work of Yang *et al*. [49] that SWCNT containing a large number of carboxyl groups (SWCNT grafted with polyacrylic acids) exhibit strong responses only at below or above pH 5. The *pKa* of the Au-Cys-SWCNT-FeOHETPc was estimated to be *ca.* 7.3. This value is slightly lower than the *pKa* value of the mercaptoethanol solution of 9.5 [26], this difference may be attributed to the stabilizing effect of the resonating sp^2 carbons of the phthalocyanine rings to which the mercaptoethanol moiety is attached.

3.5.3 Impact of single-walled carbon nanotubes on electron transfer

The FeOHETPc-based electrodes gave higher electron transfer at acidic conditions (see pH studies above), in good agreement with previous studies where it was established that MPc SAMs gave better electrochemical response in pH < 7 [13,14]. Hence, in this present work, the electron transport properties of all the modified electrodes at acidic conditions were compared. Fig 3.8(a) presents a comparative

Nyquist plots of (i) bare Au, (ii) Au-FeOHETPc, (iii) Au-Cys-SWCNT, (iv) Au-Cys-FeOHETPc, (v) Au-Cys-SWCNT-FeOHETPc$_{(No\ DCC)}$, (vi) Au-Cys-CoTAPc, and (vii) Au-Cys-SWCNT-FeOHETPc in 0.1 M PBS (pH 4.8). Other electrodes have been removed from the figure for clarity purposes but their impedance spectral data are summarized in Table 3.1. The experimental EIS data was fitted with the equivalent circuit of mixed kinetic and diffusion control (Figure 3.8(b)) involving a solution resistance, R_s, in series with Q which is a measure of capacitance of the constant phase element, CPE, R_{CT} is the electron-transfer resistance (domain of kinetic control) and Z_w is the Warburg impedance (domain of mass transport control) resulting from the diffusion of ions to the electrode interface from the bulk of the electrolyte. The impedance of the CPE (Z_{CPE}) is a power-law dependent interfacial capacity given as:[40]

$$Z_{CPE} = [Q(j\omega)^n]^{-1} \tag{3.3}$$

where Q is the frequency-independent constant, ω is the radial frequency, and n is an exponent related to the depression angle. An n value of zero corresponds to a pure resistor; a unit value of n corresponds to a pure capacitor. The CPE model was chosen for simulating the EIS data to represent the real world situation that recognizes the topographic imperfections or roughness of the electrode.

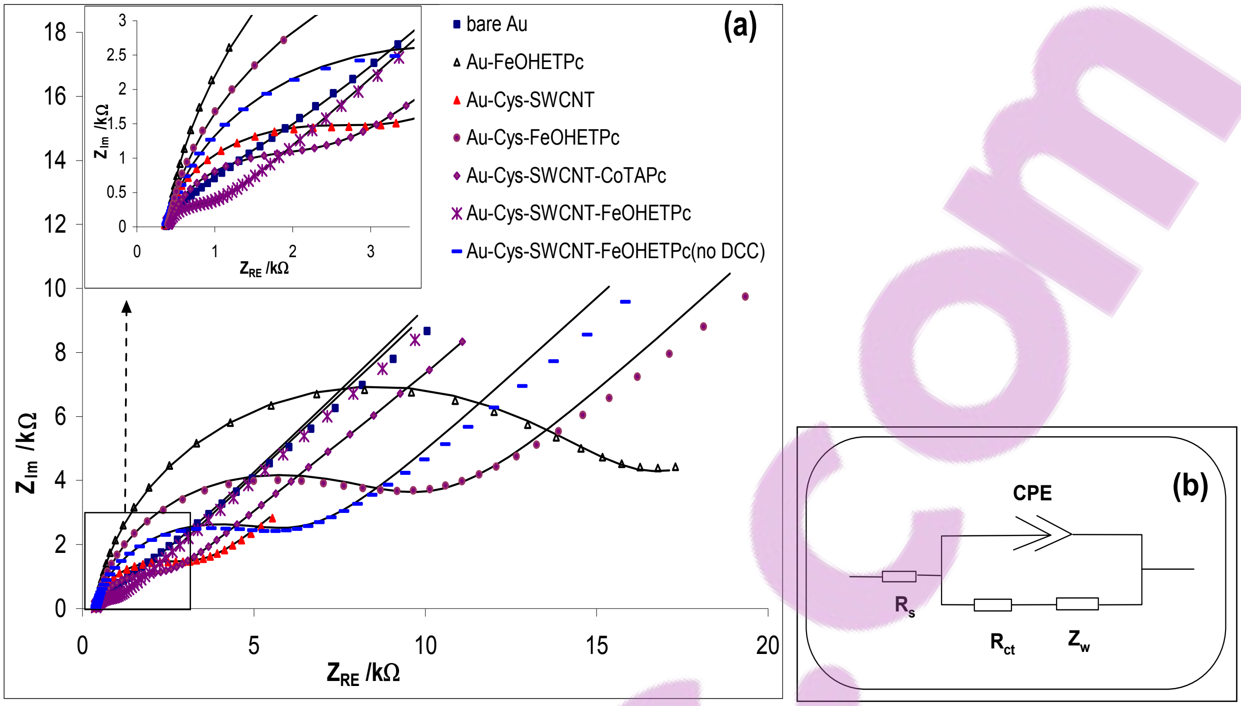

Figure 3.8: Examples of comparative Nyquist (a) and circuit used (b) fot the different modified electrodes in 0.1 M PBS (pH 4.8). Others have been removed for clarity but the EIS data are shown in Table 3.1.

As can be seen in the Table, the EIS data adequately fitted the chosen equivalent circuits with low estimated percentage errors (R_S in the 0.4 – 0.8% range; Q in the 3 – 13% range; R_{CT} between 1 and 10%; Z_W between 0.4 and 6% and n between 0.3 and 1.6%). As expected, n values extracted from the equivalent circuit were in the 0.6 – 0.9 range, confirming that the electrodes exhibit pseudocapacitive behaviour. Note that the Q values obtained here are consistent with the C_T estimated from the voltammetric analysis in equation 1, the electrode obtained by randomly dispersing SWCNT on the gold electrode (Au-Cys-SWCNT$_{dd}$-FeOHETPc) gave the highest Q values. It is interesting to observe that the Q value for the Au-Cys-SWCNT$_{dd}$-FeOHETPc is about 30 times greater than of the aligned Au-Cys-SWCNT-FeOHETPc electrode.

Also, the comparative Bode plots of phase angle vs log *f* (Figure 3.9 (a)) showed well-defined symmetrical peaks at different maxima for the different electrodes, corresponding to the different relaxation processes of the electrode|solution interfaces. The slopes of the Bode plots (log *Z* vs log *f*, Figure 3.9(b)) are approximately identical for all the electrodes (*ca*. –0.40, r^2 = 0.997) at the mid frequency region, indicative of pseudocapacitive behaviour. At high frequency regions, the slopes are almost zero, indicative of resistive behaviour at these high frequency regions. The phase angles (i.e., –phase angle *(ϕ)* vs log *f*,) which are in the range of 25 - 42°, less than the 90° also expected of an ideal capacitive behaviour.

The apparent electron transfer rate constant k_{app} was obtained from the conventional equation [50] (see Table 3.1):

$$k_{app} = \frac{RT}{n^2 F^2 A R_{CT} C} \tag{3.4}$$

where n is the number of electron transferred (i.e. n=1), A is the geometric area of the electrode (0.027 cm^2), C is the concentration of the $[Fe(CN)_6]^{3-}$ (in mol cm^{-3}, the concentration of $[Fe(CN)_6]^{3-}$ and

$[Fe(CN)_6]^{4-}$ are equal), R, T and F have their usual meanings. As exemplified in the acidic pH, FeOHETPc without SWCNT showed much higher R_{CT} value (low k_{app}) than the SWCNT-FeOHETPc, indicating that SWCNT markedly enhances the electronic communications between FeOHETPc and the gold electrode. It is also noteworthy here to observe (Figure 3.8, pH 4.8 PBS) that under similar experimental conditions employing $[Fe(CN)_6]^{3-/4-}$ as redox probe, Au-Cys-SWCNT-FeOHETPc showed much faster electron transfer (~ 3 times faster) than the previously reported Au-Cys-SWCNT-CoTAPc. Thre is no firm explanation for this but may be related to the differences in the head groups and central metal ions that change the chemistry of the two MPc complexes. Depending on experimental conditions, surface-immobilized FePc complexes sometimes show faster electron transport and better catalysis compared to their surface-immobilised CoPc counterparts [51] The value of k_{app} for the Au-Cys-SWCNT$_{dd}$-FeOHETPc (~1.2 x 10^{-3} cm s^{-1}) is about 16 times less than that of the aligned Au-Cys-SWCNT-FeOHETPc electrode (~1.7 x 10^{-2} cms^{-1}). This is in good agreement with the report of Gooding and coworkers [3,52] that electron transfer to ferricyanide in solution was slower at randomly dispersed SWCNTs than at vertically aligned SWCNTs.

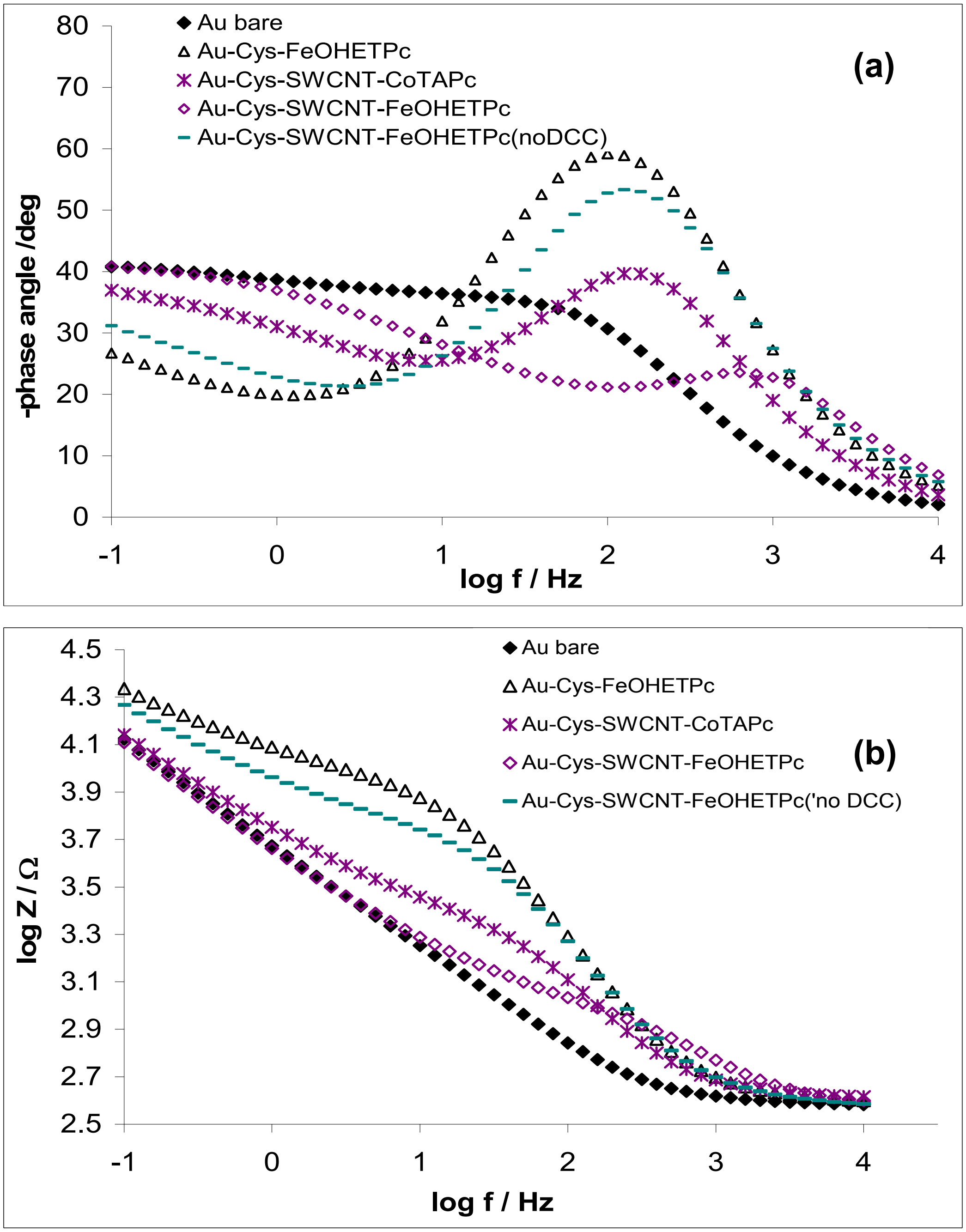

Figure 3.9: Bode plots, phase angle vs log f (a) and log Z vs log f (b),of the impedance spectra of the modified electrodes in redox probe ($[Fe(CN)_6]_{4-}$/ $[Fe(CN)_6]_{3-}$) in 0.1 M PBS solution (pH 4.8). Others have been removed for clarity but the EIS data are shown in Table 3.1.

This difference may be related to the different pathways to which electrons move at the two orientations. Unlike the vertically aligned orientation where electron-flow presumably occur between the underlying gold electrode and a redox species in solution through a single nanotube, at the randomly dispersed SWCNT, the electron-flow likely occur by hopping of electrons from one nanotube to the next mainly across the nanotube walls. Electron transport is expected to be faster along the tube than through the nanotube walls, similar to faster electron transport through edge plane than the basal plane [53,54]. Thus, electron hopping through nanotube walls should be expected to be the slowest step. Following similar literature reports for SWCNT-based SAM electrodes [3-5], the aligned SWCNTs may be assumed to act as efficient conductive nanowires in the electron transport process of the Au-Cys-SWCNT-FeOHETPc electrode.

Table 3.1: Summary of estimated EIS parameters.

Electrode	**Estimated Electrochemical Impedance Parameter**[1]					
	R_s / kΩ	**Q / μF**	**R_{ct} / kΩ**	**10^4 Z_w / Ω $s^{-1/2}$**	**n**	**10^3 k_{app} / cm s^{-1}**
Bare Au	0.38 (0.66)	0.42 (12.69)	1.92 (7.51)	9.02 (1.31)	0.75 (1.62)	5.14±0.39
Au-Cys	0.37 (0.66)	0.02 (11.38)	6.74 (7.76)	0.85 (4.98)	0.58 (1.04)	1.46±0.11
Au-Cys-SWCNT	0.36 (0.36)	0.52 (2.78)	2.75 (0.95)	1.05 (1.03)	0.97 (0.37)	3.59±0.03
Au-Cys-SWCNT-FeOHETPc	0.38 (0.83)	0.16 (11.82)	0.59 (2.75)	1.01 (0.36)	0.86 (1.64)	16.71±0.46
Au-$SWCNT_{dd}$-FeOHETPc[2]	0.39 (0.66)	4.83 (8.72)	8.55 (9.93)	0.99 (4.85)	0.83 (1.14)	1.15±0.11
Au-Cys-FeOHETPc	0.40 (0.62)	0.36 (3.23)	8.67 (0.95)	0.87 (1.31)	0.90 (0.38)	1.14± 0.01
Au-Cys-SWCNT-$FeOHETPc_{(no\ DCC)}$[3]	0.38 (0.75)	0.32 (4.50)	5.38 (1.26)	0.89 (1.21)	0.88 (0.55)	1.83 ±0.02
Au-FeOHETPc	0.76 (0.62)	0.31 (2.72)	4.81 (1.10)	1.00 (6.04)	0.92 (0.33)	0.67±0.01
Au-Cys-SWCNT-FeTAPc	0.91 (0.31)	2.34 (7.32)	0.95 (2.01)	1.04 (0.48)	0.86 (1.10)	0.28±0.02

[1] The values in brackets for R_S, Q, R_{CT}, Z_W and n are the estimated error in percent. All potential were measured against Ag|AgCl wire. [2] Electrode obtained by first coating the gold electrode with SWCNT and drying, followed by immersion in DMF solution of FeOHETPc for 25h; [3] Electrode obtained without the addition of the coupling agent, DCC, in either the solution of SWCNT or FeOHETPc.

REFERENCES

1. K. I. Ozoemena, T. Nyokong, P. Westbroek, *Electroanalysis* 15 (2003) 1762.
2. M. P. Somashekarappa, J. Keshavaya, S. Sampath, *Pure Appl. Chem*. 74 (2002) 1609.
3. J. J. Gooding, R. Wibowo, J. Liu, W. Yang, D. Losic, S. Orbons, F. J. Meams, J. G. Shapter, D. B. Hibbert, *J. Am. Chem. Soc.* 125 (2003) 9006.
4. F. Patolsky, Y. Weizmann, I. Willner, *Angew. Chem. Int. Ed*. 43 (2004) 2113.
5. L. Sheeney-Haj-Ichia, B. Basnar, I. Willner, *Angew. Chem. Int. Ed*. 44 (2005) 78.
6. Z. Li, M. Lieberman, W. Hill, *Langmuir* 17 (2001) 4887.
7. B. Varughese, S. Chellama, and M. Lieberman, Langmuir 18 (2002) 7964.
8. C. -J. Zhong, R. C. Brush, J. Anderegg, M. D. Porter, *Langmuir* 15 (1999) 518.
9. M. Wirde, U. Gelius, L. Nyholm, *Langmuir* 15 (1999) 6370.
10. Z. Chen, K. Kobashi, U. Rauwald, R. Booker, H. Fan, W. -F. Hwang, J. M. *Tour, J. Am. Chem. Soc.* 128 (2006) 10568.
11. J. Chattopadhyay, F. de Jesus Cortez, S. Chakraborty, N. K. H. Slater, W. E. Billups, *Chem. Mater*. 18 (2006) 5864.

12. Handbook *of X-Ray Photoelectron Spectroscopy,* ed. G. E. Muilenberg, Perkin-Elmer Corp, Eden Praire, Minnesota, 1979.

13. K. I. Ozoemena, T. Nyokong, P. Westbroek, *Electroanalysis* 15 (2003) 1762.

14. K. I. Ozoemena, T. Nyokong, *Electrochim. Acta*, 47 (2002) 4035.

15. H. Luo, Z. Shi, N. Li, Z. Gu, Q. Zhuang, *Anal. Chem.* 73 (2001) 915.

16. A. B. P Lever, E. R. Milaeva, G. Speier In: A. P. B. Lever and C. C. Leznoff, Editors, *Phthalocyanines: Properties and Applications,* Vol.3, VCH Publishers, New York 1993.

17. M. P. Somashekarappa, J. Keshavaya, S. Sampath, *Pure Appl. Chem*. 74 (2002) 1609.

18. H. O. Finklea in *Electroanalytical Chemistry,* eds. A. J. Bard and I. Rubinstein, Marcel Dekker, New York, Vol. 19, 1996, p.109.

19. H. O. Finklea in *Encyclopedia of Analytical Chemistry: Applications, Theory and Instrumentations,* eds. R.A. Meyers, Wiley, Chichester, 11 (2000) 10090.

20. J. K. Campbell, L. Sun, R. M. Crooks, *J. Am. Chem. Soc*. 121 (1999) 3779.

21. B. R. Azamian, J. J. Davis, K. S. Coleman, C. B. Bagshaw, M. L. H. Green, *J. Am. Chem. Soc*. 124 (2002) 12664.

22. M. Shin, N. W. S. Kam, R. J. Chen, Y. M. Li, H. J. Dai, *Nano Lett*. 2 (2002) 285.

23. X. Wang, Y. Liu, W. Qiu, D. Zhu, *J. Mater. Chem.* 12 (2002) 1636.

24. J. S. Ye, Y. Wen, W. D. Zhang, H. F. Cui, G. Q. Xu, F. S. Sheu, *Electroanalysis* 17 (2005) 89.

25. K. I. Ozoemena, J. Pillay, T. Nyokong, *Electrochem. Commun*. 8 (2006) 1391.

26. H. Munakata, D. Oyamatsu, and S. Kuwabata, *Langmuir* 20 (2004) 10123.

27. R. Z. Shervedani, M. Bagherzadeh, and S. A. Mozaffari, *Sens. Actuators B* 115 (2006) 614.

28. C. R. Raj and S. Behera, *J. Electroanal. Chem*. 581 (2000) 61.

29. J. Ye, J. Liu, Z. Zhang, J. Hu, S. Dong, Y. Shao, *J. Electroanal. Chem*. 508 (2001)123.

30. H. Luo, Z. Shi, N. Li, Z. Gu, Q. Zhuang, *Anal. Chem.* 7 (2001) 915.

31. M. Musameh, J. Wang, A. Merkoci, Y. Lin, *Electrochem. Commun*. 4 (2002) 743.

32. J. Wang, M. Li, Z. Shi, N. Li, Z. Gu, *Electroanalysis* 14 (2002) 225.

33. L. Wang, J. Wang, F. Zhou, *Electroanalysis* 16 (2004) 627.

34. L. Su, F. Gao and L. Mao, *Anal. Chem*. 78 (2006) 2651.

35. A. J. Bard, L. R. Faulkner, Electrochemical Methods: Fundamentals and Applications, 2nd ed., John Wiley & Sons, Hoboken, NJ. 2001

36. G. Kalyuzhny, A. Vaskevich, G. Ashkenasy A. Schanzer, I. Rubinstein, *J. Phys. Chem. B*. 104 (2000) 8238.

37. E. Kats and I. Wilner, Electroanalysis 15 (2003) 913.

38. E. Kats and I. Wilner in: V. M. Mirsky (Ed.), Ultrathin Electrochemical Chemo and Biosensors. Technology and Performance, Springer-Verlag, New York, Chapter 4 (2004) 68

39. E. Barsoukov, J. R. Macdonald (Ed.), Impedance Spectroscopy: Theory Experiment and Applications 2nd ed., Wiley Hoboken, New Jersey, Chapter 1-4 (2005)

40. D. D. Macdonald, Electrochim. Acta 51 (2006) 1376.

41. M. A. Bryant and R. M. Crooks, Langmuir 9 (1993) 385.

42. J. Zhao, L. Luo, X. Yang, E. Wang, and S. Dong, *Electroanalysis* 11 (1999) 1108.

43. J. F. Smalley, K. Chalfant, S. W. Feldberg, T. M. Nahir, and E. F. Bowden, J. Phys. Chem. B 103 (1999) 1676.

44. Y. Jiang, Z. Wang, H. Xu, H. Chen, X. Zhang, M. Smet, W. Dehaem, Y. Hirano and Y. Ozaki*, Langmuir* 22 (2006) 3715.

45. M. Root and A. M. Shaw, *Phys.chemChem.Phys*. 8 (2006) 4741.

46. T. R. Lee, R. D. Carey, H. A. Biebuyck, G. M. Whitesides, *Langmuir* 10 (1994) 741.

47. Y. Y. Jun, K. S. Beng, *Electrochem. Commun.* 6 (2004) 87.

48. J. H. Back and M. Shim, *J. Phys. Chem. B*. 110 (2006) 23736.

49. D. Yang, J. Hu, C. Wang, *Carbon* 44 (2006) 3161.

50. E. Sabatani, I. Rubinstein, *J. Phys. Chem.* 91(1987) 6663.

51. K. I. Ozoemena, T. Nyokong, In Encyclopedia of Sensors, C. A Grimes, E. C. Dickey, M. V. Pishko, Eds., American Scientific Publishers, California, 3 (2006) Chapter E, pp.157 – 200, and references therein.

52. J. J. Gooding, *Electrochim. Acta*. 50 (2005) 3049.

53. C. E. Banks, R. R. Moore, T. J. Davies, R. G. Compton, *Chem. Commun*. 2004 1804.

54. C. E. Banks, T. J. Davies, G. G. Wildgoose, R. G. Compton, *Chem. Commun.* (2005) 829.

CHAPTER 4

ELECTROCATALYTIC PROPERTIES OF IRON-PHTHALOCYANINE-SWCNT BASED ELECTRODES: THIOCYANATE AS A MODEL ANALYTE

4.1 Square wave voltammetric detection of SCN$^-$

Figure 4.1 shows a typical comparative square wave voltammetric (SWV) evolutions obtained at constant concentration (1 mM) of SCN$^-$ at the various electrodes. The following deductions can be made from these voltammograms. First, it clearly shows that the current response at the various electrodes follows this trend: Au-Cys-SWCNT-FeOHETPc > Au-Cys-SWCNT-FeTAPc > Au-Cys-SWCNT > Au-Cys ≈ Au-FeOHETPc > Au-FeTAPc ≈ Bare Au (see figure 4.1 for abbreviations). The enhanced current response of the FeOHETPc and FeTAPc in the presence of the SWCNTs is a clear indication that the aligned SWCNTs enhance the electronic communication between FeOHETPc and FeTAPc and the bare gold electrode. It may be concluded here that it is the combined synergistic activities of these iron phthalocyanine (FePc) complexes (good catalysts) and the SWCNTs (efficient electronic conducting nanowires) that is responsible for the enhanced response of the Au-Cys-SWCNT-FeOHETPc and Au-Cys-SWCNT-FeTAPc towards the detection of the SCN$^-$ species.

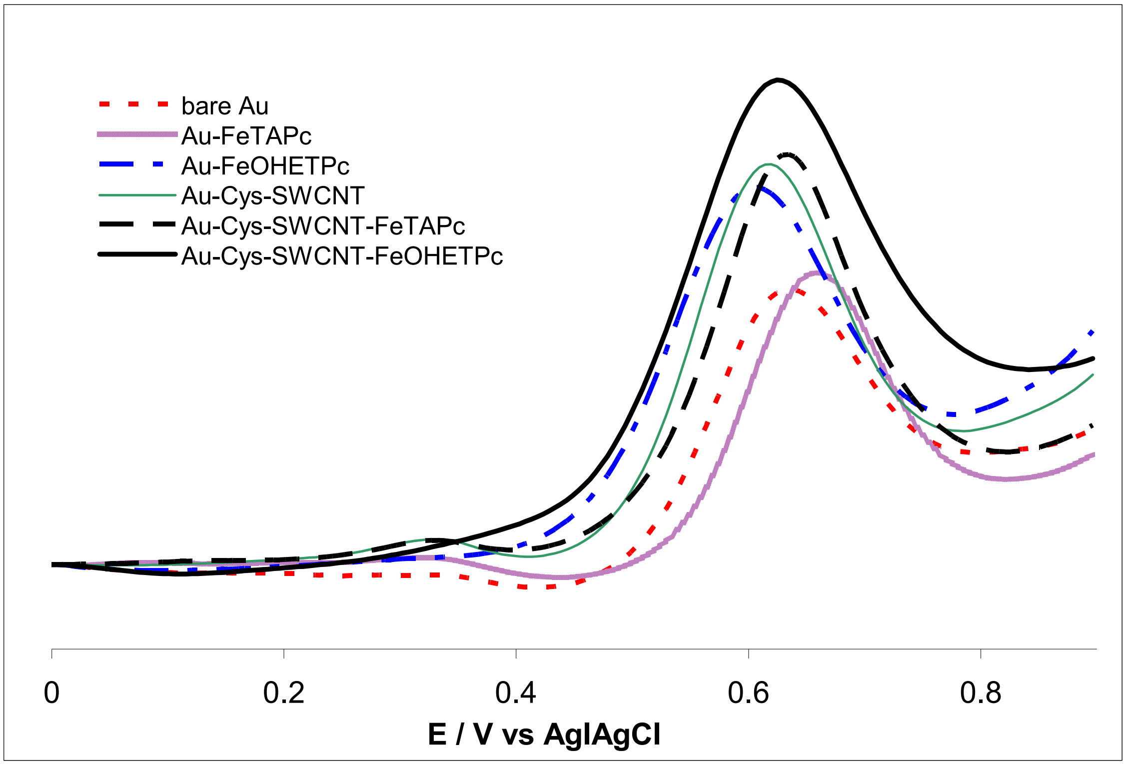

Figure 4.1: Typical comparative square wave voltammetric response of the various electrodes in PBS solution (pH 4.8) containing 1 mM SCN^-. Au-Cys voltammogram omitted for clarity.

Second, the weak peaks observed at the ~0.3 V for the electrodes modified with SWCNTs and the FePc complexes (FeOHETPc and FeTAPc) are attributed to the redox waves of the acidified SWCNT [1] and the $Fe^{(II)}/Fe^{(III)}$ [2], respectively. As it was recently observed [2], in acidic pH (0.5 M H_2SO_4) the Au-Cys-SWCNT shows pseudo-reversibility with anodic peak around 0.2 V (vs Ag|AgCl) and a cathodic peak at about −0.1 V (vs Ag|AgCl), thus the broadness of this peak for the Au-Cys-SWCNT-FeOHETPc electrode may be associated with the overlap of both the redox waves of the SWCNTs and that of the FePc complexes.

Third, FeOHETPc-based electrodes gave better response than their FeTAPc counterparts. The electrocatalytic activity of the FeOHETPc-based electrodes started at less positive potentials and with greater current response compared to the FeTAPc-based electrodes. Of special note is the electrocatalytic activity of the Au-Cys-SWCNT-FeOHETPc that started from ~0.3 V compared to all the other electrodes that only started at ≥ 0.4 V. Some of the established factors that could influence the electrochemistry of MPc complexes are (i) the type of central metal ion; (ii) nature of axial ligands on the central metal; and (iii) the type and position of substituents (peripheral or non-peripheral, electron-donating or electron-accepting, and amount substituted from 1 to 16) at the macrocyclic phthalocyanine rings. Since the only structural difference between these two FePc complexes used in this work is the different substituent groups ($-NH_2$ and $-SCH_2CH_2OH$ moieties), the high current response of the FeOHETPc over the FeTAPc is most likely to be due to the influence of these peripheral substituents. Thus, subsequent studies in this work, unless otherwise stated, were focused on the Au-Cys-SWCNT-FeOHETPc electrode.

4.2 Influence of scan rates on electrocatalysis of SCN$^-$

Cyclic voltammetric experiments were carried out with a view to establishing the impact of scan rates (ν) at constant concentration (1 mM) of the SCN$^-$. The study was carried out with both Au-Cys-SWCNT-FeOHETPc and Au-Cys-SWCNT-FeTAPc electrodes (exemplified in Figure 4.2(a) using Au-Cys-SWCNT-FeOHETPc). At both electrodes there were corresponding increases in the peak currents with increasing scan rates (scan rates ranging 25 - 1000 mV/s). Also, a broad reduction peak (in the 0.1 to 0.5 V regions) appearing only at higher scan rates, > 100 mVs^{-1}. A similar observation was reported in a previous study [3], where unsubstituted FePc was axially coordinated to the SAM of 4-mercaptopyrindine species on gold elelctrode (Au-4-MPyr-FePc) using the strategy introduced by Rubinstein and co-workers [4,5] (but only at > 25 mVs^{-1}), and was attributed to the reduction product(s) of the oxidised SCN$^-$ species. The same explanation may hold for this study especially since it has been reported by others [6] that the oxidation of SCN$^-$ is associated with several oxidation products via the unstable thiocyanogen $(SCN)_2$.

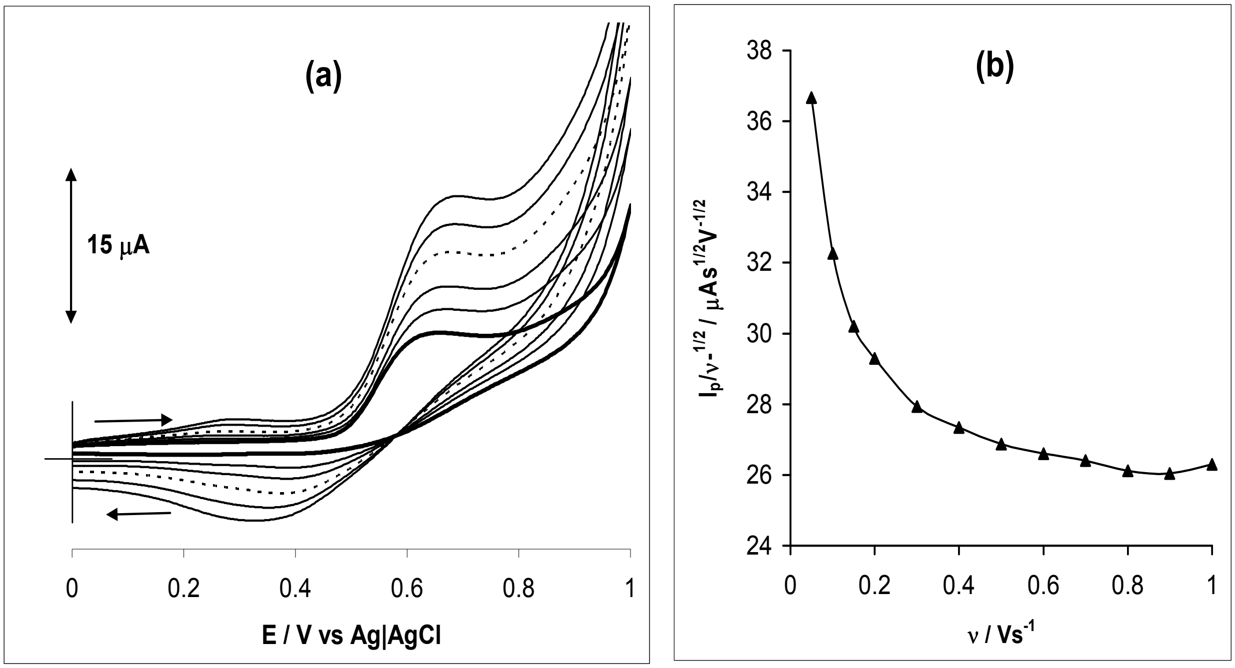

Figure 4.2: (a) Typical examples of cyclic voltammetric evolutions at varying scan rates (50, 150, 200, 400, 600 and 800 mVs^{-1}, inner to outer; outer omitted for clarity); and (b) Plot of current function ($I_p/\nu^{1/2}$) versus scan rate (ν) ranging from 50 to 1000 mVs^{-1}. [SCN$^-$] = 1 mM

The main reasons for the detection of these intermediate products of the oxidised SCN$^-$ at > 25 mVs^{-1} for the Au-4-MPyr-FePc and at >100 mVs^{-1} for the Au-Cys-SWCNT-FeOHETPc are not apparent at this moment, but may be connected with the different reactivities of these two types of SAM-based electrodes. It could be interesting to further investigate this observation in future studies. The current function ($I_p/\nu^{1/2}$) decreased with the scan rate (figure 4.2b) which is indicative of a coupled chemical reaction, EC_{cat} mechanism [7-9]. Peak current (I_p) of the SCN^- oxidation gave a linear relationship with the square root of scan rate ($\nu^{1/2}$) ($R^2 = 0.9985$), indicating a diffusion-controlled reaction. A plot of I_p vs ν was not linear proving that neither the oxidized SCN^- nor its intermediate product(s) adsorbed on the modified electrode.

The equation for an irreversible diffusion controlled process is given as Equation 4.1 [10]:

$$E_p = \frac{b}{2}\log\nu + \text{constant.} \tag{4.1}$$

where b = Tafel slope = $0.059/\alpha n_\alpha$, α is the electron transfer coefficient, while $n\alpha$ is the number of electrons involved in the rate-determining step). The plots of the E_p vs $\log\nu$ gave linear equations as shown in equation 4.2.

$$E_p\,(\mathrm{V}) = (58.66\pm1.09)\times10^{-3}\,log\,\nu + (787.60\pm 0.66)\times10^{-3}$$
$$(R^2 = 0.9989) \tag{4.2}$$

Assuming an electron transfer coefficient (α) ≈ 0.50, the values of the Tafel slope was *ca.* 117 $\mathrm{mVdecade}^{-1}$, which is in excellent agreement with the ideal value of 118 $\mathrm{mVdecade}^{-1}$ for a one-electron process in the rate-limiting step [11]. This value agrees with the report using cobalt tetraethoxythiophenephthalocyanine as electrocatalyst [12]. Thus, this present result clearly suggests (i) the participation of a one-electron activity in the rate-determining step (rds) of the SCN^- oxidation at the Au-Cys-SWCNT-FeOHETPc, and (ii) that neither SCN^- nor its intermediate product(s) irreversibly adsorb on the electrode since such process should be expected to raise the Tafel slope to values higher than 120 mV/decade [11].

FePc complex is a mimic of the horse radish peroxidise (HRP), and according the work of Adak *et al* [6], HRP-catalysed oxidation of SCN^- occurs by two one-electron process with the intermediate formation of thiocyanate radicals. The radical readily dimerise to form the unstable thiocyanogen $(SCN)_2$. The $(SCN)_2$ is unstable in aqueous solution and readily hydrolyses to form some stable intermediate products. It is also well known that metalloporphyrin- and metallophthalocyanine-catalysed reactions of SCN^- usually occur by initial binding of the SCN^- to the central metal [13]. From these information and all the results (notably the involvement of the one electron process in the rate determining step as well as the coupled chemical reactions) obtained from the scan rate studies, the following reaction mechanism is suggested (Equations 4.3-4.8):

$$\mathrm{Fe^{(II)}OHETPc} \longrightarrow \mathrm{Fe^{(III)}OHETPc} + \mathrm{e^-} \qquad (4.3)$$

$$\mathrm{Fe^{(III)}OHETPc} + \mathrm{SCN^-} \longrightarrow \mathrm{[SCN\text{-}Fe^{(III)}OHETPc]^-} \quad \text{(axial ligation)} \qquad (4.4)$$

$$\mathrm{[SCN\text{-}Fe^{(III)}OHETPc]^-} \longrightarrow \mathrm{[SCN\text{-}Fe^{(III)}OHETPc]} + \mathrm{e^-} \quad \text{(rds)} \qquad (4.5)$$

$$\mathrm{[SCN\text{-}Fe^{(III)}OHETPc]} \longrightarrow \mathrm{Fe^{(II)}OHETPc} + {}^{\bullet}\mathrm{SCN} \qquad (4.6)$$

$${}^{\bullet}\mathrm{SCN} + {}^{\bullet}\mathrm{SCN} \longrightarrow \mathrm{(SCN)_2} \quad \text{(fast)} \qquad (4.7)$$

$$\mathrm{(SCN)_2} + \mathrm{H_2O} \longrightarrow \text{Reaction products} \qquad (4.8)$$

The instability of the $(SCN)_2$ may partly be responsible for the inability to observe the reduction peaks at slow time scale, small scan rates. The onset of the electrocatalysis of SCN^- at the Au-Cys-SWCNT-FeOHETPc close to the redox wave of the Fe(II)/Fe(III) suggests the involvement of the central metal and axial ligation process in the catalysis.

4.3 Rotating gold disk electrode experiments

Further experiments were performed using rotating gold disk electrode (RDE) linear scan voltammetry technique. The RDE voltammetric evolutions of constant concentration (1 mM SCN$^-$) at different rotating speed of electrodes with their Koutecky-Levich plots is shown in Figure 4.3. The Koutečky-Levich plot (Figure 4.3 inset) was obtained from the conventional Koutecky-Levich theory [10], Equation 4.9:

$$\frac{1}{i_{\lim}} = \frac{1}{i_k} + \frac{1}{i_d} = \frac{1}{nFAkC} + \frac{1}{0.62nFACD^{2/3}\gamma^{-1/6}\omega^{1/2}} \qquad (4.9)$$

where $i_{\lim}$ is the measured current, i_k and i_d are the kinetic and diffusion-limited currents, respectively. C is the bulk concentration and γ is the kinematic viscosity of the solution which was estimated from 4 M SCN$^-$ as 0.8145 cm s^{-1} [14]; other symbols retain their usual meanings. The numbers 1 to 10 in the figure correspond to 250 to 3000 rads^{-1}. The results showed that the catalytic current increased linearly with increasing $\omega^{-1/2}$ with a positive intercept, indicating that the electrode reactions were controlled by both kinetics at the electrode surface and the mass transport of SCN$^-$ species at the electrode surfaces. From the intercept and the slope of the plot, the diffusion coefficient value of *ca*. 1.30 x 10^{-5} cm^2s^{-1} was obtained.

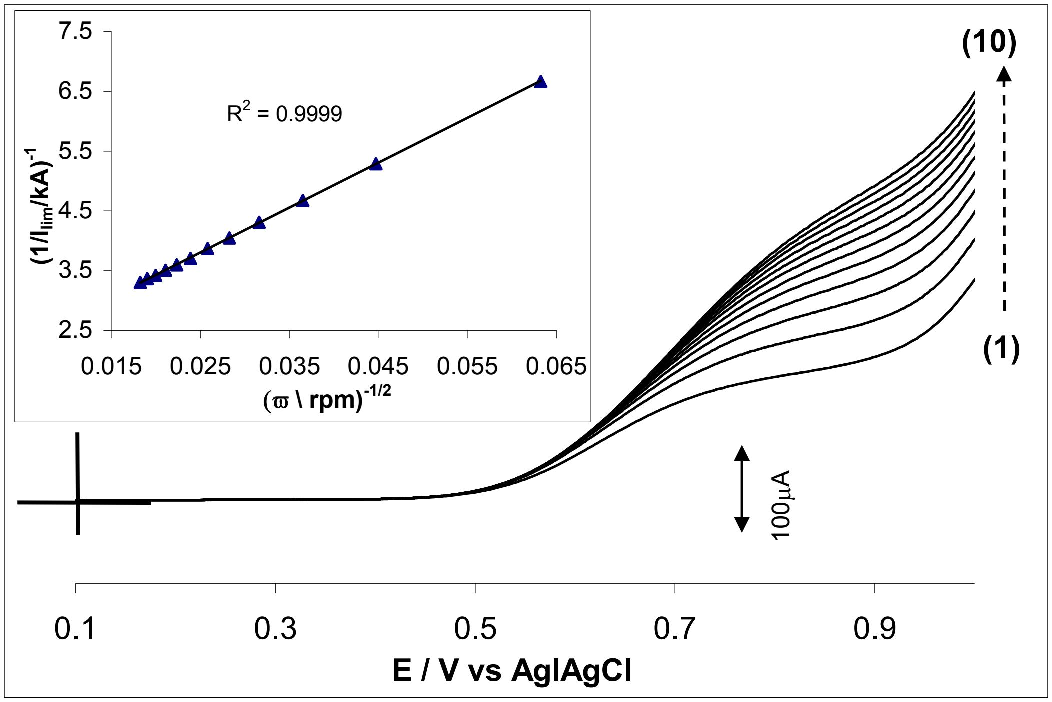

Figure 4.3: Linear sweep voltammetric evolutions of the rotating disk electrode experiments obtained at Au-Cys-SWCNT-FeOHETPc in PBS solution (pH 4.8) containing 1 mM SCN^- at 50 mVs^{-1}. (Inset is Koutečky-Levich plot.

About 28 years ago, Shimizu and Osteryoung had reported the oxidation of SCN^- at a rotating silver disk electrode (taking n = 1) and obtained a diffusion coefficient of (2.15±0.02) x10^{-5} cm^2s^{-1} [15]. If the same one-electron process is assumed, the value for D is approximately 3.60 x 10^{-5} cm^2s^{-1}, which is the same magnitude as the their report [15], the slight difference which suggests that the diffusion of SCN^- is faster at Au-Cys-SWCNT-FeOHETPc than the bare gold electrode could be ascribed to differences in experimental conditions. Using the Koutecky-Levich equation, the k value was obtained *ca*. 1.40 x 10^{-2} cm^3 mol s^{-1}.

It should be mentioned here that the electrodes (Figures 4.1 – 4.3) were stable in the acidic and neutral pH conditions in the potential window of –0.5 and +1.0V vs Ag|AgCl, a similar behaviour to the thiol-derivatised MPc SAMs that we reported previously [3]. The reason for the stability exhibited by the Au-Cys-SWCNT-FeOHETPc electrode may be due to the protection of the underlying cysteamine sulphur by the aligned SWCNTs and macrocyclic ring of the phthalocyanine. However, I advise caution when using the electrode for electroanalysis not to go beyond the +1.0 V vs Ag|AgCl to avoid electro-oxidative desorption of the film.

4.4 Chronoamperometric investigations

Double potential step chronoamperometric experiments were recorded by polarizing the working electrode potentials to 0.62 and 0.20 V (Figure 4.4). Figure 4.4 shows a well resolved double-step chronoamperometric evolutions obtained at the Au-Cys-SWCNT-FeOHETPc electrode in the absence (buffer alone) and presence of consecutive addition of 32.3 µM thiocyanate in phosphate buffer solution (pH 4.8) (The numbers 1 to10 in figure 4.4, correspond to 0.0, 32.3, 62.5, 90.9, 118, 167, 211, 250, 302 and 333 µM, respectively.). It shows that at the conditions employed for this work, the SCN^- was irreversible. Figure.4.4 (inset) depicts linearity (R^2 = 0.9987) between log I_p versus log [SCN^-] with a slope (0.8818) close to unity, suggesting that one SCN^- species interacts with one molecule of the FeOHETPc complex. Also, a linear relation was obtained for the I_p vs [SCN^-] as in Equation 4.10:

$$I_p\,(\mathrm{A}) = (4.20 \pm 0.09)\times10^{-3}\,[\mathrm{SCN^-}]/\mathrm{M} + (2.37 \pm 0.1)\times10^{-7} \quad (R^2 = 0.9964) \qquad (4.10)$$

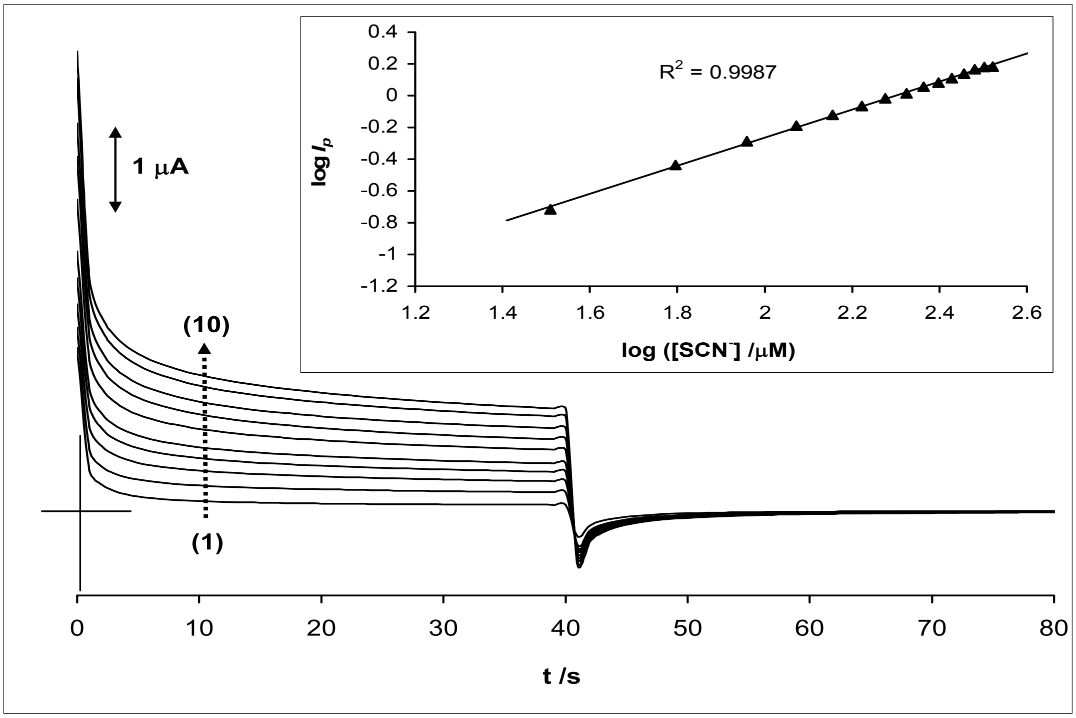

Figure 4.4: Typical double potential step chronoamperometric transients at Au-Cys-SWCNT-FeOHETPc in PBS solution (pH 4.8) following addition of SCN^- The potential was stepped from +0.62 to +0.20 and back to +0.62 V. Other chronoamperograms obtained during same experiments are omitted here for clarity purpose. Inset is the plot of chronoamperometric current at t = 10s vs log [SCN^-].

In the experimental conditions used in this work, a linear concentration range of up to 0.33 mM with a sensitivity of ca. 4.2×10^{-3} AM^{-1}, and limit of detection ~ 15 μM (LoD = 3.3 s/m [16], where s is the relative standard deviation of the intercept and m the slope of the linear peak current vs the concentration of SCN^-) were obtained

From the chronoamperometric data, both diffusion coefficient (D) and catalytic rate constant of SCN$^-$ were also determined. For D, the Cottrell equation (Equation 4.11) was used:

$$I = \frac{nFAD^{1/2}C}{\pi^{1/2}t^{1/2}} \qquad (4.11)$$

where n is the number of electrons involved in the reaction, F is the Faraday constant (96485 C mol^{-1}), and A is the experimentally determined area of the electrode, C is the bulk concentration of the thiocyanate (mol.L^{-1})), while t is time (s). It can be seen that the plots of I_p vs $t^{-1/2}$ at different thiocyanate concentrations is linear (Figure4.5), and from the plot of slopes vs [SCN$^-$], and taking n = 2, the D value for SCN$^-$ was estimated to be *ca.* 7.70x10^{-6} cm^{2}s^{-1}, which is about 60% lower than that obtained at the RDE experiment.

The catalytic rate constant for the oxidation of SCN$^-$ was also estimated from the chronoamperometry experiments using the relationship [17,18] (Equation 4.12):

$$\frac{I_{cat}}{I_{buff}} = \pi^{1/2}(kCt)^{1/2} \qquad (4.12)$$

where I_{cat} and I_{buff} are the currents in the presence and absence of thiocyanate, respectively; k is the catalytic rate constant and t is the time in seconds.

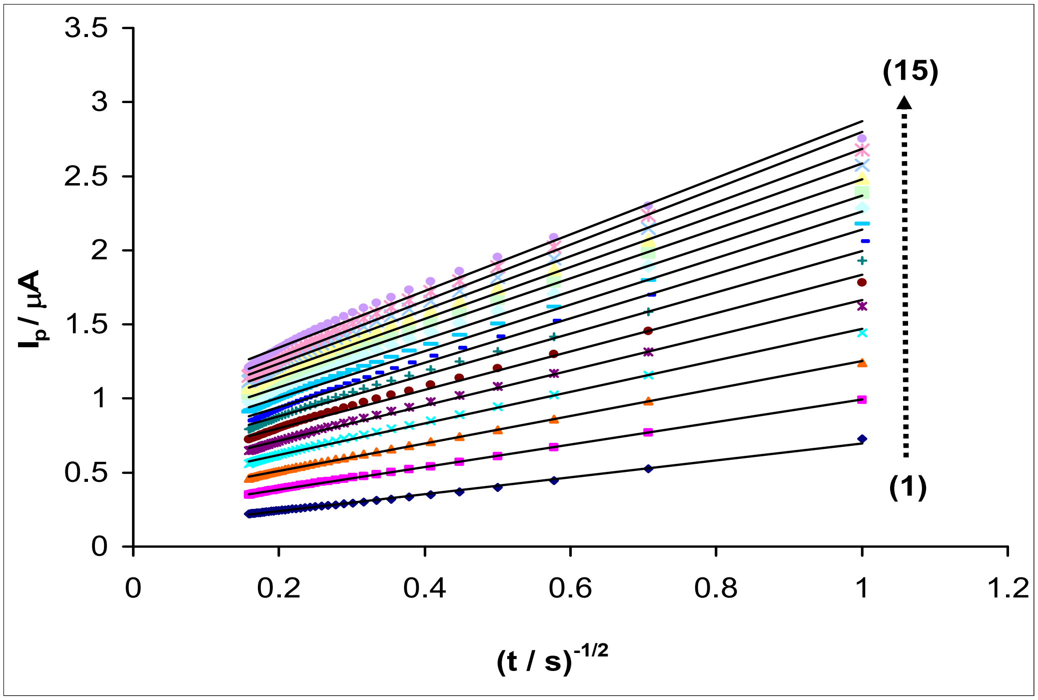

Figure 4.5: Typical Cottrell equation plots obtained from the chronoamperometric evolution at Au-Cys-SWCNT-FeOHETPc in PBS solution (pH 4.8) following addition of SCN^-. (The numbers 1 to15 correspond to 32.3, 62.5, 90.9, 118, 143, 167, 189, 211, 231, 250, 268, 286, 302, 318 and 333 μM, respectively)

From the plots of I_{cat}/I_{buff} vs $t^{1/2}$ at different thiocyanate concentrations (Figure 4.6), and a plot of the slopes vs [SCN^-], k was estimated as $1.84\text{x}10^4$ cm^3mols^{-1}. Similar chronoamperometric experiments with Au-Cys-SWCNT-FeTAPc gave sensitivity, rate constant and diffusion coefficient as $2.90 \pm 0.04\text{x}10^{-3}$ AM^{-1}, $0.82\text{x}10^4$ cm^3 mol s^{-1} and $5.97\text{x}10^{-6}$ cm^2s^{-1}, respectively. These data satisfactorily corroborate the SWV results shown in Figure 4.1.

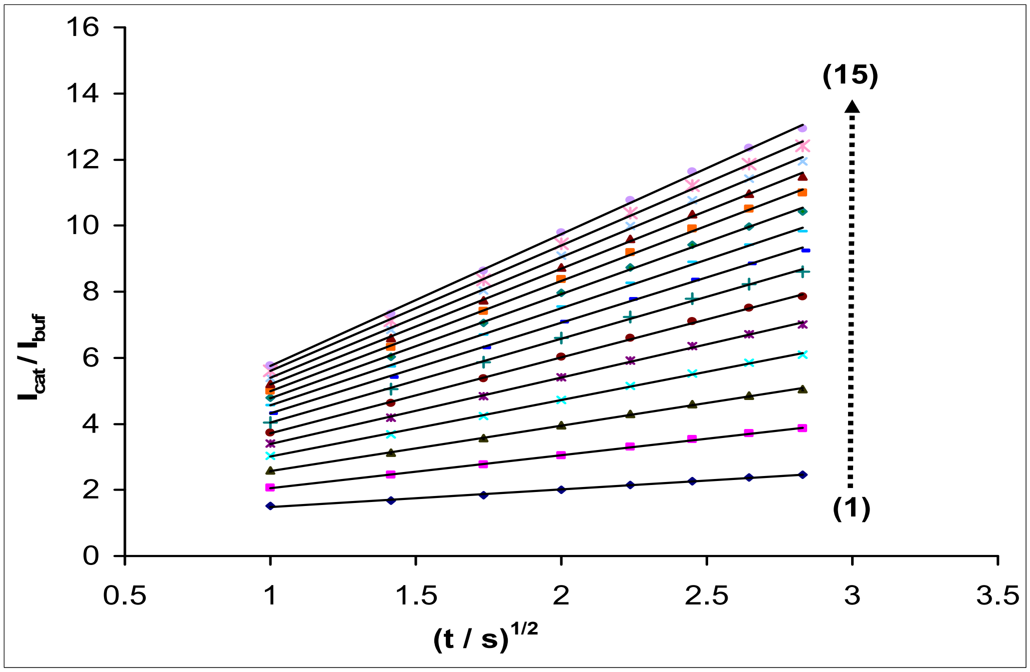

Figure 4.6: Plots of I_{cat}/I_{buff} vs $t^{1/2}$ obtained from the chronoamperometric evolution at Au-Cys-SWCNT-FeOHETPc in PBS solution (pH 4.8) following addition of SCN^-. (The numbers 1 to 15 correspond to 32.3, 62.5, 90.9, 118, 143, 167, 189, 211, 231, 250, 268, 286, 302, 318 and 333 μM, respectively)

4.5 Real sample analysis with smoker's saliva

Saliva is produced by the salivary glands and human saliva is 98% water but contains many important substances including electrolytes, mucus and antibacterial compounds and various enzymes. One of the the antibacterial compound is thiocyanate, hydrogen peroxide and secretory immunoglobulin A [19]. This study has proved that the amount of thiocyanate in human saliva of a non smoker is minimal.

For a check on the suitability of the Au-cys-SWCNT-FeOHETPc electrode for possible application as a biological sensor, the electrode was used for a comparative chronoamperometric determination of SCN^- in saliva samples of smoker and non-smoker. Figure 7.1 is an example of a typical comparative chronoamperograms in buffer solution, and buffer solutions containing saliva samples of a smoker and a non-smoker. It is clearly seen that current response to the non-smoker saliva sample is approximately as the buffer solution while that of the smoker is well pronounced. The SCN^- concentration in the saliva samples of the smoker was estimated as 38.6±0.76 μM while that of the non-smoker was 4.56±4.02 μM (n = 5).

The ability of this electrode to clearly discriminate between a smoker and non-smoker suggests that it could possibly be applied for such biological analysis in clinics.

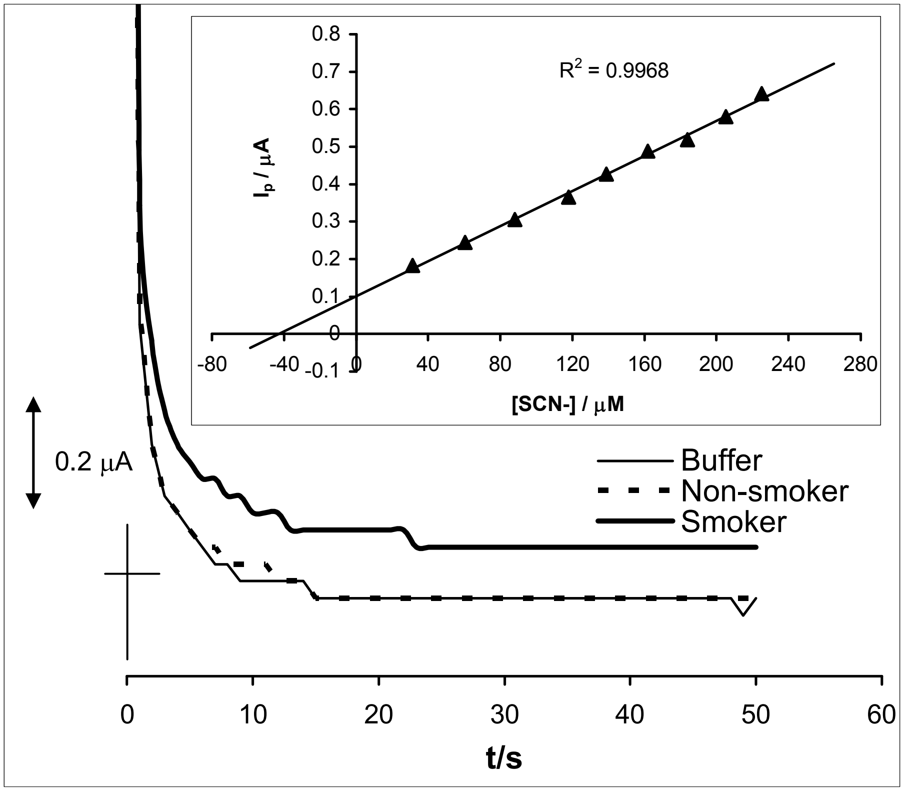

Figure 4.7: Typical example of chronoamperometric response of the saliva samples of a smoker and a non-smoker at the Au-Cys-SWCNT-FeOHETPc electrode in PBS solution (pH 4.8), fixed potential = 0.62 V vs Ag|AgCl. Inset is an example of one the replicate results of the standard addition methods.

REFERENCES

1. H. Luo, Z. Shi, N. Li, Z. Gu, Q. Zhuang, *Anal. Chem.* 73 (2001) 915.
2. K. I. Ozoemena, T. Nyokong, P. Westbroek, *Electroanalysis* 15 (2003) 1762.
3. K. I. Ozoemena, T. Nyokong, *J. Electroanal. Chem.* 579 (2005) 283.
4. G. Kalyuzhny, A. Vaskevich, G. Ashkenasy, A. Shanzer, I Rubinstein, *J. Phys. Chem. B.* 104 (2000) 8238.
5. Ashkenasy, G. Kalyuzhny, J. Libman, I Rubinstein, A. Shanzer, *Angew. Chem. Int. Ed. Engl.* 38 (1999) 1257.
6. S. Adak, A. Mazumdar, R. K. Banerjee, *J. Biol. Chem.* 272 (1997) 11049.
7. P. M. S Monk, Fundamentals of Electroanalytical Chemistry, John Wiley and Sons, Chichester, 2001, p.172
8. L. Nadjo, J. M. Saveant, *J. Electroanal. Chem.* 48 (1970) 113.
9. R. S. Nicholson, I. Shain, *Anal. Chem.* 36 (1994) 706.
10. A. J. Bard and Faulkner, Electrochemical Methods: Fundamentals and applications, 2nd ed., John Willey & Sons, Hoboken, NJ., 2001.
11. J. A. Harrison, Z. A. Khan, *J. Electroanal. Chem.* 28 (1970) 131.
12. N. Sehlotho, T. Nyokong, *Electrochim. Acta* 51 (2006) 4463.

13. K. I. Ozoemena, T. Nyokong, In Encyclopedia of Sensors, C. A Grimes, E.C. Dickey, M.V. Pishko, Eds., American Scientific Publishers, California, 3 (2006) Chapter E, pp.157.

14. A. V. Balmasov, E. V. Koroleva, S. A. Lilin., *Protect. Met.* 41 (2005) 35.

15. K. Shimizu, R. A. Osteryoung, *Anal. Chem.* 53 (1981) 2351

16. G. D. Christian, Analytical Chemistry, 6th ed. John Wiley and Sons, New York, 2004, p.113.

17. M. H. Pournaghi-Azar, R. Sabzi, *J. Electroanal. Chem.* 543 (2003) 115.

18. K. M. Manesh, P. Santosh, A. I. Gopalan, K. -P. Lee, *Electroanalysis* 18 (2006) 894.

19. M. Anthea, J. Hopkins, C. W. McLaughlin, S. Johnson, M. Q. Warner, D. LaHart, J. D. Wright, *Human Biology and Health*. Englewood Cliffs, New Jersey, USA: Prentice Hall (1993),

CHAPTER 5

MICROSCOPIC AND ELECTROCHEMICAL PROPERTIES OF FERROCENE SINGLE-WALLED CARBON NANOTUBES BASED ELECTRODES

5.1 SAM formation strategies

Monolayers of alkanethiol capped with carboxylated ferrocene and single-walled carbon nanotubes were prepared by self-assembly technique on gold surfaces. Scheme 5.1 and 5.2 summarizes the self-assembly technique which employed the normal carbodiimide coupling chemistry [1] whereby the –COOH functional groups are first activated to permit the covalent bonding with the $-NH_2$ groups of the cysteamine. The gold electrode modified with cysteamine is represented as Au-Cys. The formation of Au-Cys-FDCA and Au-Cys-FMCA followed after placing the Au-Cys electrode in a 1 ml DMF solution containing 0.5 mg (*ca.* 2μmol) of DCC and 1 mg (*ca.* 4 μmol) of FDCA or 1mg (*ca.* 4μmol) FMCA for 48hr, respectively. The Au-Cys-SWCNT-FDCA electrode was obtained by placing Au-Cys in 1ml DMF solution containing a mixture of SWCNT (1 mg) and FDCA (1 mg) and 0.5 mg DCC for 48hr. This same method was used to prepare Au-Cys-SWCNT-FMCA. Upon removal from the deposition solution, prior to electrochemical experiments, the electrode was thoroughly rinsed with millipore water and dried in a nitrogen atmosphere. The modified electrode was conditioned by placing in 0.5 M H_2SO_4 and repetitively scanned between −0.5 and 0.6 V (vs Ag|AgCl) potential window at a scan rate of 25 mVs^{-1} until a constant scan was obtained.

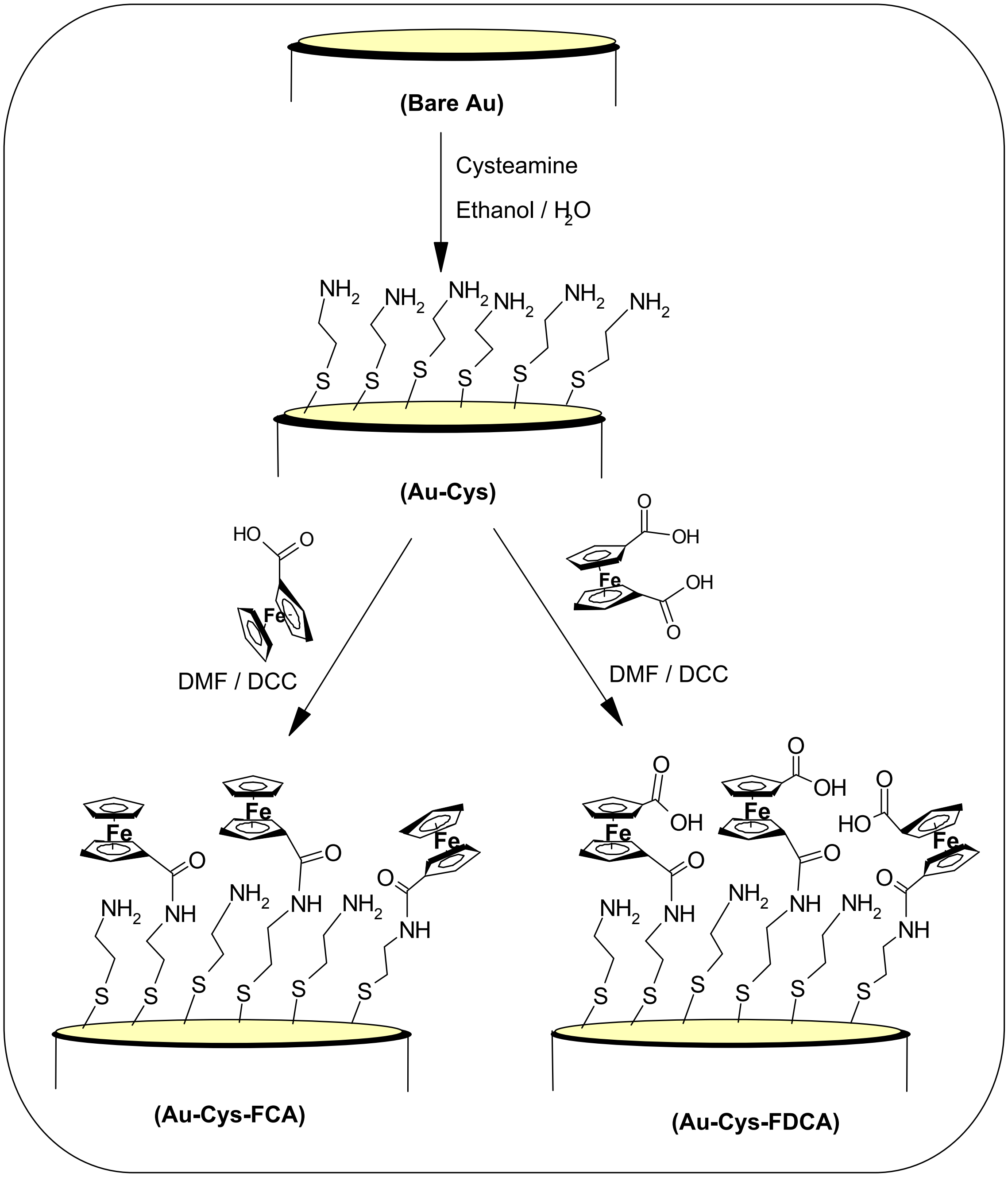

Scheme 5.1: Schematic of the gold electrode modification routes for Au-Cys, Au-Cys-FCA and Au-Cys-FDCA.

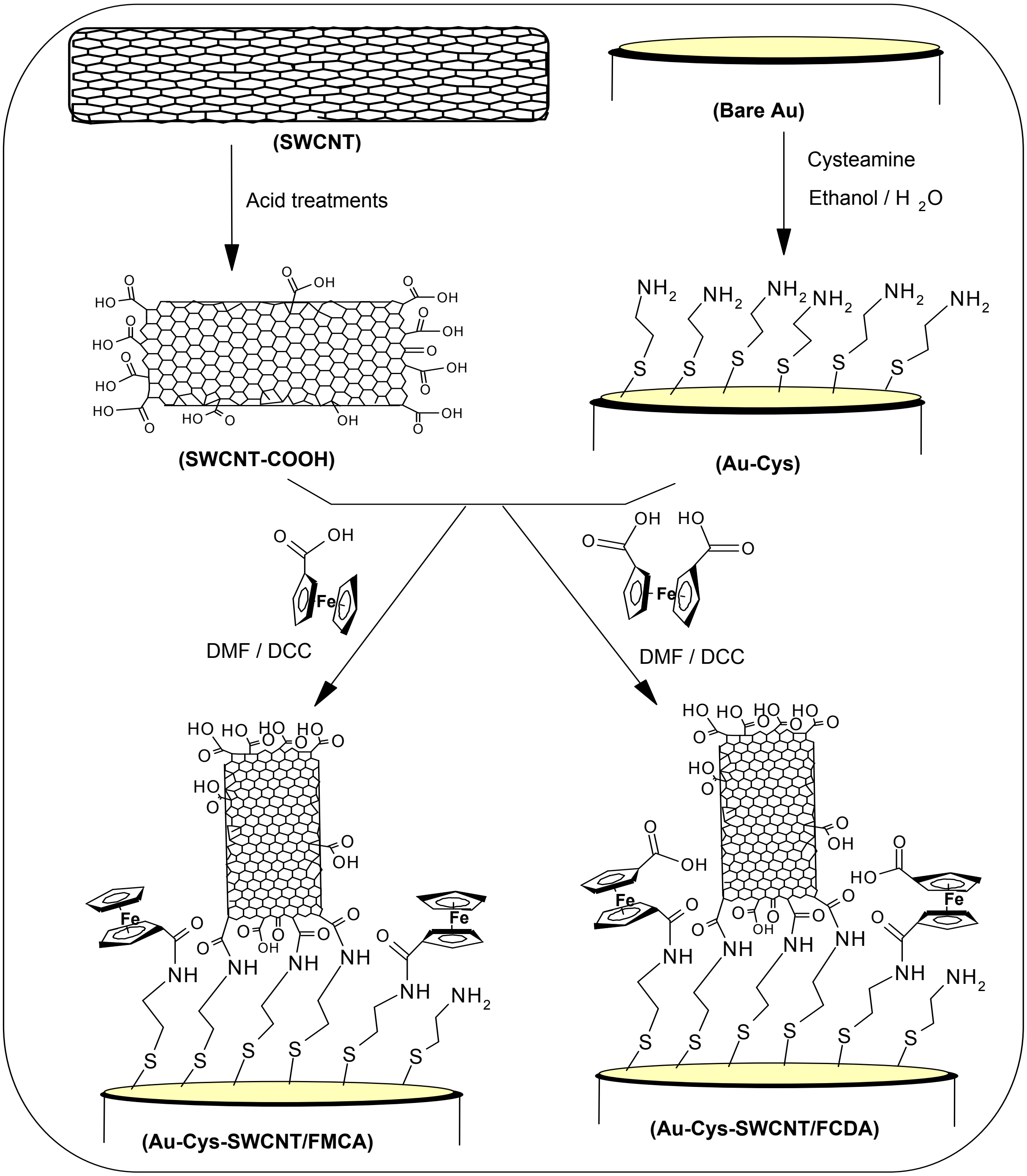

Scheme 5.2: Schematic of the gold electrode modification routes for Au-Cys-SWCNT/FMCA and Au-Cys-SWCNT/FDCA.

5.2 Atomic force microscopic characterization

Figure 5.1 summarizes the fabrication sequences for self-assembling of the SWCNTs, FCDA and FMCA onto gold electrode. Confirmation of the attachment of these redox-active species, by self-assembly technique was achieved by the use of atomic force microscopy. Figure 5.1 compares the AFM images of (a) bare Au, (b) Au-Cys-SWCNT, (c) Au-Cys-FDCA and (d) Au-Cys-SWCNT/FDCA. The needle-like protrusion of the Au-Cys-SWCNT agrees with several reports for SWCNT-based SAMs [2,3]. Typical lengths of acid-treated SWCNTs using the conditions used in this work lie in the 250 – 350 nm [4]. However, when we immobilized them as SAMs, the heights lie in the 30 – 50 nm range, which is in close agreement with literature [2]. The SWCNTs assembled as bundles and not as individual due to the strong van der Waal's attractive forces existing between carbon nanotubes. The same explanation may be true for the needle-like protrusion shown by the Au-Cys-FDCA. Interestingly, as would be expected, the mixed layers, Au-Cys-SWCNT/FDCA, showed more compactness than either the individual layers. Generally, the AFM topographic height and roughness in Figure 5.1 are greater with the combined SWCNT and Fc assemblies, exemplified with Au-Cys-SWCNT/FDCA (d). The rougness and height of the Au-Cys-SWCNT (b) are higher than those of the Au-Cys-FDCA (c) or Au-Cys-FMCA (not shown), confirming that SWCNTs are longer than the FC assemblies (as indicated in the cartoon of scheme 5.2).

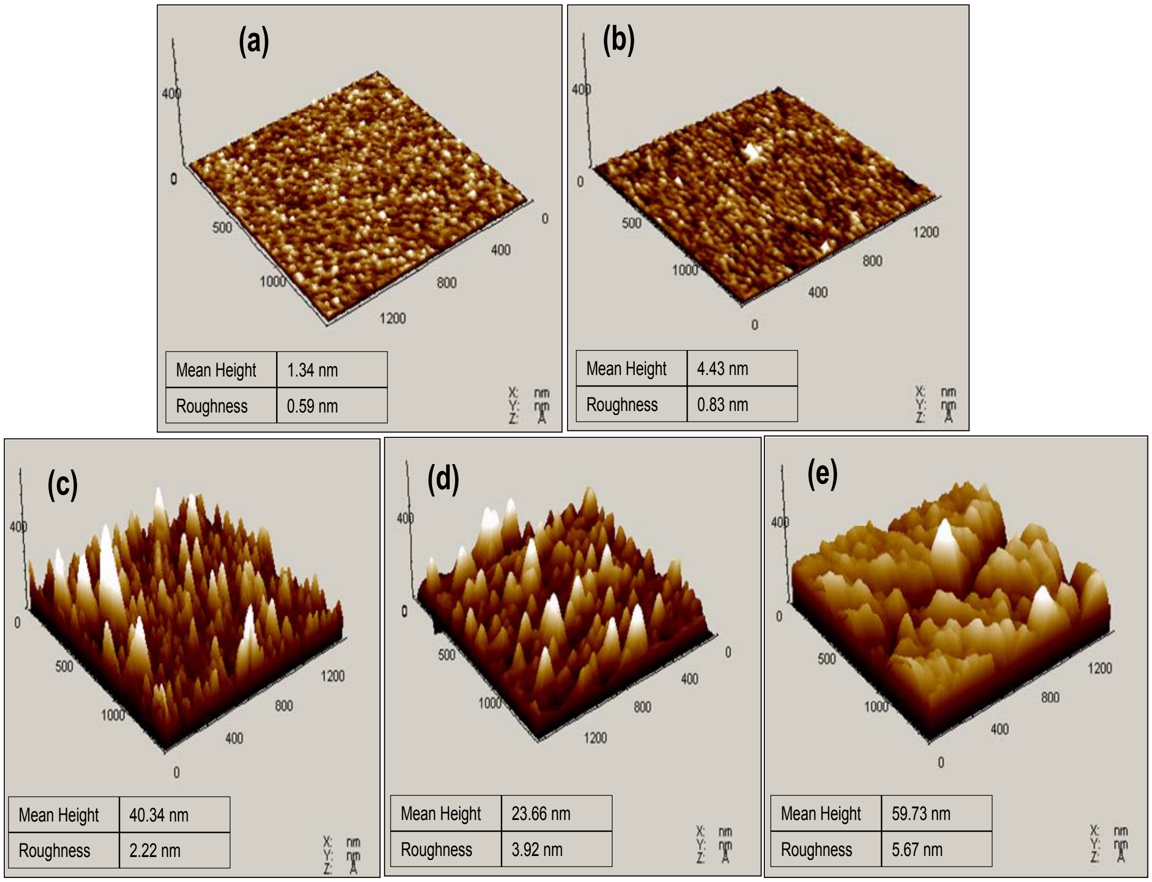

Figure 5.1: Topographic images of the electrodes: (a) Au bare, (b) Au-Cys, (c) Au-Cys-SWCNT, (d) Au-Cys-FDCA and (e) Au-Cys-SWCNT/FDCA.

5.3 Electron transfer dynamics in 0.5 M H_2SO_4 solution.

5.3.1 Cyclic voltammetric characterization

The cyclic voltammetric properties of the ferrocene-modified gold electrodes were studied in 0.5 M H_2SO_4 solution. Figure 5.2 shows the CV profiles of the electrodes obtained at 25 mVs^{-1}.

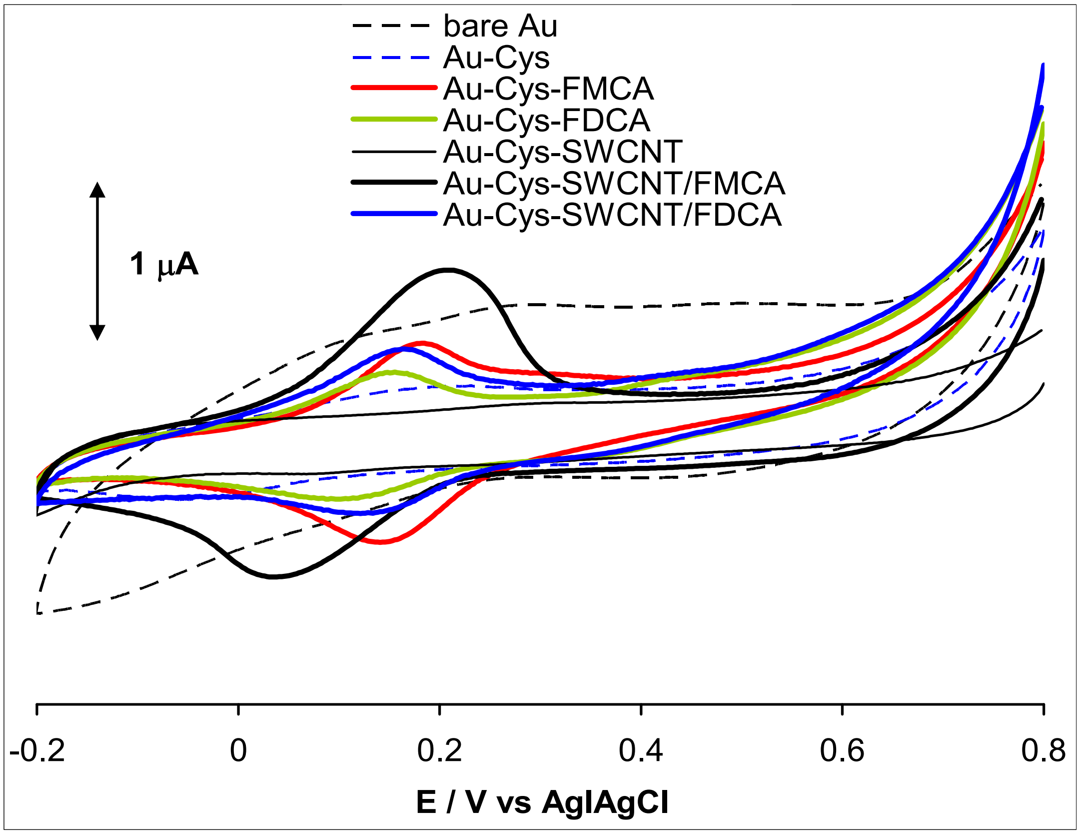

Figure 5.2: Comparative cyclic voltammetric evolutions of the modified gold electrode in 0.5 M H_2SO_4, Au-Cys-FCA, Au-Cys-FDCA, Au-Cys-SWCNT, Au-Cys-SWCNT/FMCA and Au-Cys-SWCNT/FDCA.

Each of the redox couples is ascribed to the Fe(III)/Fe(II) redox process. The electrochemical parameters, formal potential ($E_{1/2}$ / mV), peak-to-peak potential separation (ΔE_p / mV), the width at half the peak current (E_{fwhm} / mV) and ratio of anodic peak current to the cathodic peak (I_{pa}/I_{pc}) and surface coverages (Γ/molecule.cm^{-2}) are summarized in Table 5.1. All the electrodes show $I_{pa}/I_{pc} \approx 1$, indicating voltammetric reversibility. The choice of the potential used here was based on our experience working with thiolated SAMs. As we cautioned in previous reports on SAMs [5,6], the thiol monolayer only show remarkable stability in acidic and slightly alkaline pH (pH 2 – 9) at potential between window of –0.5 and +0.9 V vs Ag/AgCl. At more positive potential (≥ +0.9 V vs Ag|AgCl) thiol desorption and / or Au surface oxidation could be observed. The stability observed for these SAMs may be related to some extent by hydrogen bonds arising from the –COOH and –OH funtional groups. It may also be related to the protection of the sulfur by the large SWCNTs and and/or FC rings. The interchain attractive interactions resulting from the alkyl chains may also be another contributing factor.

As seen from Table 5.1, the electron transport (signified by the magnitude ΔE_p) in this acid electrolyte condition is fastest at the Au-Cys-SWCNT/FDCA ≈ Au-Cys-FMCA and slowest at the Au-Cys-SWCNT/FMCA. In a similar manner, the E_{fwhm} values (in the 71 – 117 mV range) slightly deviate from the ideal value of 90.6/n mV for $n = 1$ [7-9], with the Au-Cys-SWCNT/FMCA (117 mV) being slightly greater than that of the Au-Cys-SWCNT/FDCA (104 mV). The higher values of ΔE_p and E_{fwhm} for the SWCNT/FMCA compared to its SWCNT/FDCA counterpart may be related to different factors. First, some workers [3,4,10,11] have attributed such phenomenon to ferrocene species being located in a range of environments with a range of $E_{1/2}$. This should not be totally surprising considering the distribution of lengths of the SWCNTs on the gold substrate, and that the ferrocenes studied in this work could possibly be attached to the ends and/or defect sites of the SWCNTs via ester bonds (i.e., between the –COOH of the ferrocene and few –OH groups on the SWCNTs).

By different environments, it is meant that the ferrocene species have different formal potentials, and thus the effective voltammetric wave will consist of a superposition of distinct electrochemical responses, resulting in the observed voltammetric broadening [4]. It is worth pointing out that the formal redox potentials of the two FC species will be different. Also, as can be clearly seen from the the CVs, especially in the 0.3 – 0.8 V region, the backgroung current or capacitance of the bare Au (CAu) is about three times higher than the capacitance of any of the SAM-modified gold electrode (CAu-SAM).

Table 5.1: Summary of estimated voltammetric data obtained in 0.5 M H_2SO_4 (n = 4)

	Electrochemical parameters					
Electrodes	$E_{1/2}$ / mV	ΔE_p/ mV	E_{fwhm} / mV	I_{pa}/I_{pc}	$10^9\ \Gamma_a$/mol cm^{-2}	Γ_a/Γ_c
Au-Cys-FMCA	158	4.8	71	0.8	1.6±0.3	0.704
Au-Cys-FDCA	131	14.7	104	0.9	1.1±0.2	0.781
Au-Cys-SWCNT/FMCA	137	95.2	117	1.1	3.3±0.8	1.030
Au-Cys-SWCNT/FDCA	146	4.7	107	1.1	1.4±0.3	0.845

This is expected since as in aqueous solution, unlike in organic solutions, the overall electrode double-layer capacitance should be governed by the bare Au (i.e., CAu > CAu-SAM) [12,13].

The second explanation for the non-ideal ΔE_p and E_{fwhm} values for the adsorbed ferrocenes may be found from the works of Chidsey and co-workers [14-16]. According to these workers, when the self-assembled ferrocene species are well separated and do not interact with one another, a narrow symmetric redox peak with ideal E_{fwhm} value of 90.6/n mV will be obtained. However, as the concentration n of the ferrocene adsorbates increases, the resulting voltammograms will become asymmetric, broaden, with an increase in the ΔE_p value.

5.3.1.1 Surface coverage

The surface coverages were established from the CV profiles in 0.5M H_2SO_4 using the relationship:

$$\Gamma_{SAM} = \frac{Q}{nFA} = \frac{\int Idt}{nFA} \qquad (5.1)$$

where Q is the background-corrected charge under the cathodic or anodic waves, n = number of electrons involved in the redox process, F is the Faraday constant, and A is the area of the electrode. The surface coverage values are listed in Table 5.1. The average coverage increases as SWCNT/FMCA (3.3 x 10^{-9} mol cm^{-2}, 2.0 x 10^{15}

molecules/cm^{-2}) > Cys-FMCA (1.6 x 10^{-9} mol cm^{-2}, 9.6 x 10^{14} molecules/cm^{-2}) > SWCNT/FCDA (1.4 x 10^{-9} mol cm^{-2}, 8.4 x 10^{14} molecules/cm^{-2}) > Cys-FCDA (1.1 x 10^{-9} mol cm^{-2}, 6.6 x 10^{14} molecules/cm^{-2}). Since the maximum coverage expected of a monolayer of ferrocene is 4.5 x 10^{-10} mol cm^{-2} [4] (*ca* 2.7 x 10^{14} molecules cm^{-2} or ≈ 37 Å^2 per molecule), it means that the coverages obtained in this work are between 3 and 8 times higher than expected. It should however be noted that other workers have observed similar or even higher values compared to our results. For example, Gooding *et al*. [4] observed a much higher surface coverage (1.8±0.9 x 10^{-8} mol cm^{-2}) for randomly-distributed ferrocenes on SWCNTs and attributed this to the existence of a three-dimensional network of redox sites. Flavel *et al*. [10] observed a 1.14 x 10^{-9} mol cm^{-2} and 9.59 x 10^{-8} mol cm^{-2}) for macro- and nanoscale ferrocenemethanol-modified carbon nanotube electrodes on silicon, respectively. Chambers *et al*. [17] reported values of ~4 x 10^{14} molecules cm^{-2}. It is possible that the high surface coverages obtained in this work could be due to the long exposure time of cysteamine to gold electrode leading to more binding sites for the ferrocenes. The high surface coverage for the SWCNT/FMCA compared to SWCNT/FDCA suggests that FMCA species probably coordinate more with SWCNTs via ester bonds as described above compared to its FDCA counterparts. It is known from Chidsey and co-workers [14-16] that high concentration of ferrocene adsorbates leads to asymmetric and broad voltammograms, hence high ΔE_p values.

Thus, the higher surface coverage shown by the FMCA-based electrode (Table 5.1) may further explain the poor ΔE_p and E_{fwhm} values of the SWCNT/FMCA compared to its SWCNT/FDCA counterpart.

5.3.1.2 Repetitive scanning

The voltammetric behaviour of the electrodes when subjected to repetitive scanning in acidic electrolyte was also investigated. This experiment is necessary for establishing the electrochemical stability of these redox-active adsorbates. Figure 5.5 shows typical voltammograms (1st and 20th scans of each electrode) obtained on repetitively scanning each electrode in the 0.5 M H_2SO_4 solution. For all the electrodes, we observed that the first few scans (*ca.* 1 – 5 scans) remained unchanged. However, as the scan number was increased, the voltammograms became broadened (thereby increasing both the E_{fwhm} and ΔE_p values) stabilising at about the 20th scan.

Unlike the low values of the ΔE_p seen at the first five scans (Table 5.1), at the 20th scan, the ΔE_p values increased to ~ 100 mV for the Cys-FMCA, > 200 mV for the Cys-FDCA, and ~100 mV for the SWCNT/FDCA. For the SWCNT/FMCA, however, there was a slight decrease from its original 95 mV to about 80 mV at the 20th scan. This is an interesting observation considering that such behaviour has only been observed when the concentration of ferrocene adsorbates is increased [14-16]. Besides, Finklea [18] had demonstrated that the cause of such behavior arising from increase in concentration of the ferrocene to be due to double-layer effects arising from a rapid increase in surface charge during oxidation.

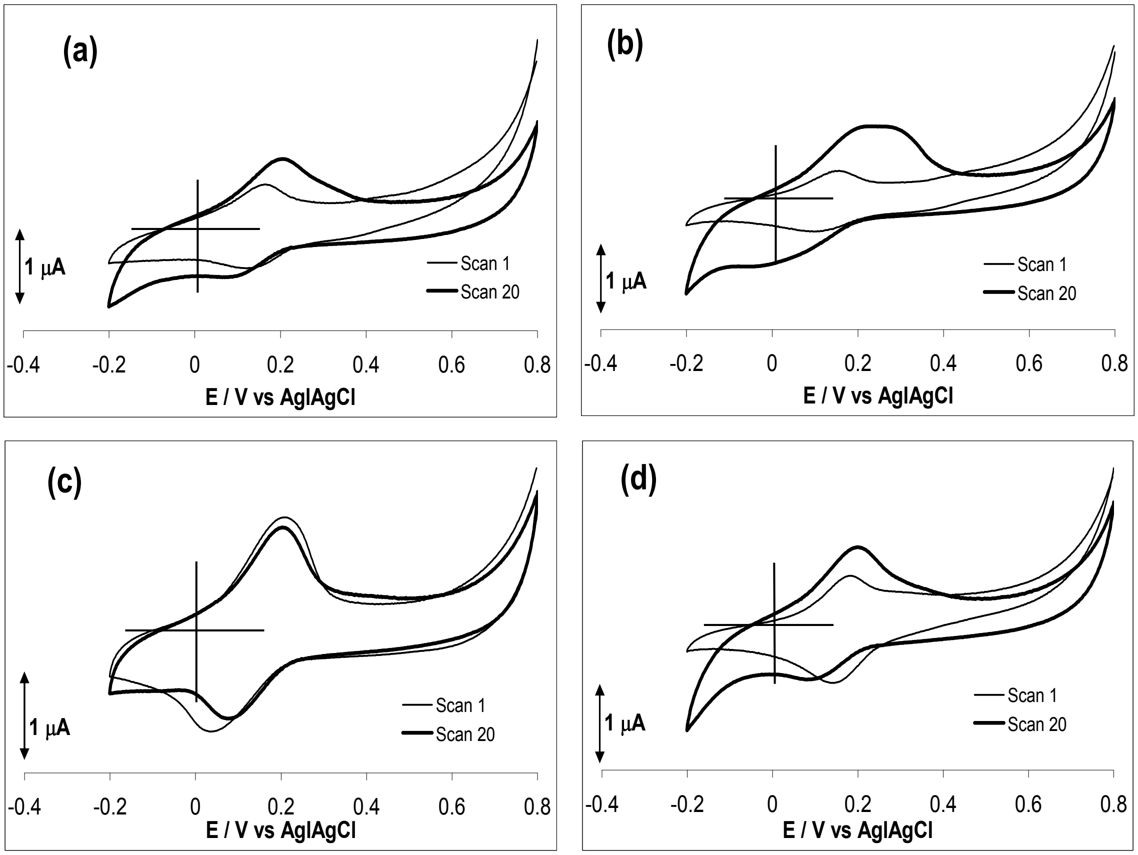

Figure 5.3: Comparative cyclic voltammetric evolutions of the modified gold electrode in 0.5M H_2SO_4 obtained at the 1st and the 20th scans for (a) Au-Cys-SWCNT/FDCA, (b) Au-Cys-FDCA, (c) Au-Cys-SWCNT/FMCA and (d) Au-Cys-FMCA. Scan rate = 25 mVs^{-1}.

In other words, surface charge effectively decreases the potential difference between the remaining unoxidised ferrocenes and the surface, and thus requiring a high applied bias for the oxidation of these ferrocene. But, in our case, since the concentration of the ferrocene species in each electrode is the same at all scans, the assumption of the asymmetric and broadening nature of the redox peaks during repetitive scanning may probably be due to the disordering of the initial well-separated ferrocene species to a form where they now interact with one another. Simply put, during the first few scans of the ferrocene-based electrodes, the ferrocenes head groups are still well-separated and do not interact with one another (indicated by the near-ideal E_{fwhm} value, Table 5.1). However, as the scanning number is increased, these ferrocenes may now begin to interact with one another and / or the double layer effects ensure. Also, it is worthy to note from Figure 5.5 that without the SWCNTs, the ΔE_p value is higher compared to when Ferrocene is co-assembled with the SWCNTs, suggesting that SWCNTs tend to suppress this double-layer effects (for example, compare the CVs of Au-Cys-FMCA and Au-Cys-SWCNT/FMCA).

The existence of the ferrocene redox activity during the repetitive scanning indicates that the modified electrodes exhibited strong electrochemical stability in 0.5 M H_2SO_4 solution. Such stability is important for their electrochemical studies as well as their potential applications in acidic pH conditions. Thus, all subsequent experiment with each of the ferrocene-based electrode was performed after 20 continuous scanning in 0.5 M H_2SO_4 solution

5.3.2 Electrochemical impedimetric characterization

Electrochemical impedance spectroscopy (EIS) is an important technique for probing heterogeneous electron transfer (HET) kinetics, especially at gold electrode modified with self-assembled mono or multi-layers of redox-active or redox silent species [13,19-22]. To establish the HET kinetics in this acidic solution, EIS experiments were carried out for each of the modified electrode, as described by Creager and Wooster [19]. Figure 5.3(a) presents typical comparative Nyquist plots obtained for the four modified electrodes, biased at their approximate formal potential (~0.14 V vs Ag|AgCl). Interestingly, the experimental data were satisfactorily fitted with the modified Randles electrical equivalent circuit (Figure 5.3(b)), popularly used for modelling a redox-active monolayer on an electrode surface [13,19]. In the model, the R_s is the solution or electrolyte resistance, R_{ct} represents the electron-transfer resistance, while the true double layer capacitance (C_{dl}) is replaced by a constant phase element (CPE_1) and

Warburg impedance (Z_w) replaced by another constant phase element (CPE_2 or capacitance of the adsorbed molecules). The electron transfer rate constant (k_{et}) of each of the electrodes was obtained from: [13,19]

$$k_{et} = \frac{1}{(2R_{ct}CPE_2)} \tag{5.2}$$

From Table 5.2, the k_{et} value increased as follows: Au-Cys-FMCA (~ 12 s^{-1}) ≈ Au-Cys-SWCNT/FDCA (~ 10 s^{-1}) > Au-Cys-FDCA (~ 0.8 s^{-1}) > Au-Cys-SWCNT/FMCA (~ 0.3 s^{-1}), in close agreement with of the CV data listed in Table 5.1.

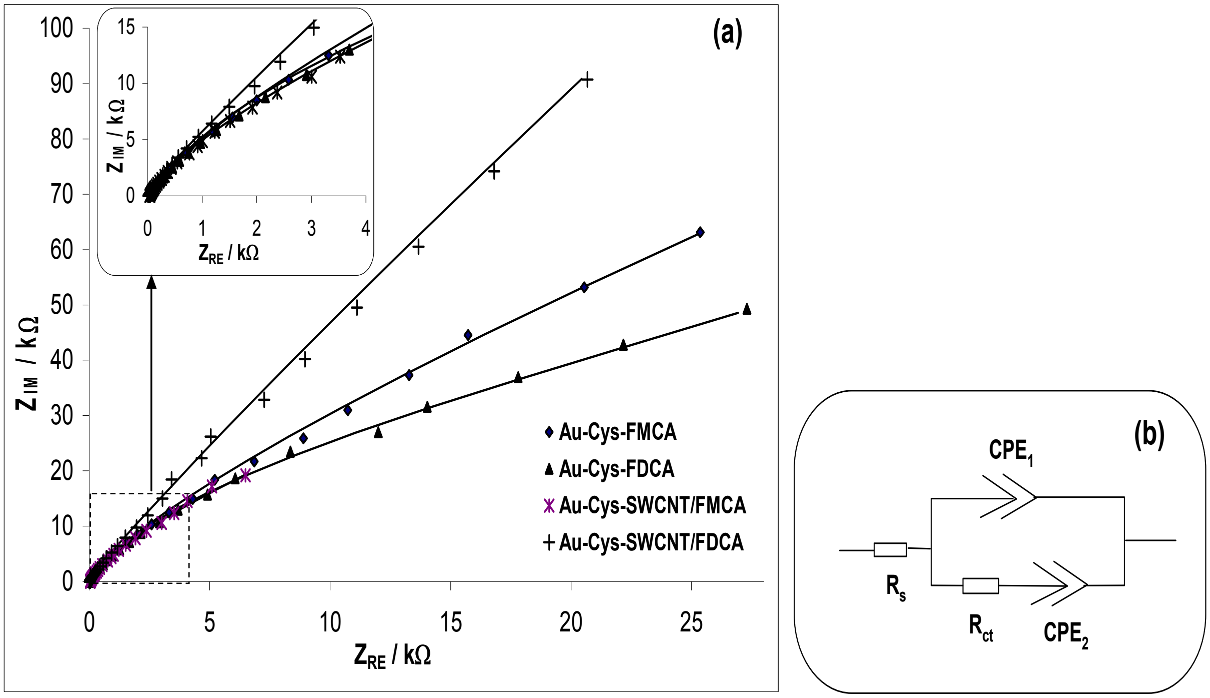

Figure 5.4 Nyquist plots (a) of the modified electrodes in the H_2SO_4 solution and (b) Equivalent circuit used in fitting (a).

It is interesting to observe how the neighbouring SWCNTs impact on the HET of the two different types of ferrocenes, SWCNTs improve the HET of ferrocene with exposed –COOH groups (FDCA) but decrease the HET of the ferrocene containing no pendant –COOH groups (FMCA).

The impedance of a CPE (Z_{CPE}) is defined as [23,24]:

$$Z_{CPE} = \frac{1}{[Q(j\omega)^n]} \tag{5.3}$$

where Q is the frequency-independent constant relating to the surface electroactive properties, ω is the radial frequency, the exponent n arises from the slope of log Z vs log f (and has values $-1 \leq n \leq 1$). If $n = 0$, the CPE behaves as a pure resistor; $n = 1$, CPE behaves as a pure capacitor, $n = -1$ CPE behaves as an inductor; while $n = 0.5$ corresponds to Warburg impedance (Z_W) which is associated with the domain of mass transport control arising from the diffusion of ions to and from the electrode|solution interface. In general terms, CPE arises from such factors as (i) the nature of the electrode (e.g., roughness and polycrystallinity), (ii) distribution of the relaxation times due to heterogeneities existing at the electrode/electrolyte interface, (iii) porosity and (iv) dynamic disorder associated with diffusion [25].

Table 5.2: Summary of estimated EIS parameters obtained in 0.5 M H_2SO_4

Electrodes	Electrochemical Impedemetric parameters[1]						
	R1 /Ω	Q1 /μF	n_1	R2 /kΩ	Q2 /μF	n_2	k_{et} / s^{-1}
Au-Cys-FMCA	49.50 (0.72)	2.20(3.57)	0.97 (0.44)	11.56 (27.61)	3.66 (1.59)	0.56 (1.09)	11.80
Au-Cys-FDCA	40.20 (0.66)	5.07 (1.08)	0.93 (0.18)	76.31 (6.20)	8.38 (2.40)	0.66 (3.46)	0.78
Au-Cys-SWCNT/FMCA	41.50(1.50)	8.00(1.86)	0.92 (0.36)	116.2(6.36)	16.19 (5.23)	0.77 (2.76)	0.27
Au-Cys-SWCNT/FDCA	18.90 (1.16)	4.32 (2.81)	0.94 (0..71)	24.16 (29.22)	2.16 (5.02)	0.66 (1.27)	9.56

[1] The value in brackets are the estimated error percentages.

Thus, the n_1 values in Table 5.2 are approximately close to 1.0 for an ideal capacitive behaviour, while the n_2 (that replaced the Warburg diffusion) are in the range between 0.56 and 0.77, describing the porous nature of the adsorbed film on the gold electrode.

The phase angles seen on the Bode plots (i.e., –phase angle (ϕ) vs log f, Figure 5.4(a)) are in the range of 75 - 80^{o}, which are less than the 90^{o} expected of an ideal capacitive behaviour. Figure 5.4(b) illustrates the relationship between the logarithm of impedance and frequency. The slopes of the Bode plots (log Z vs log f) are approximately similar (*ca*. –0.82, r^2 = 0.992) at the mid frequency region, indicative of pseudocapacitive behaviour. At high frequency regions, the slopes are almost zero, indicative of resistive behaviour at these high frequency regions.

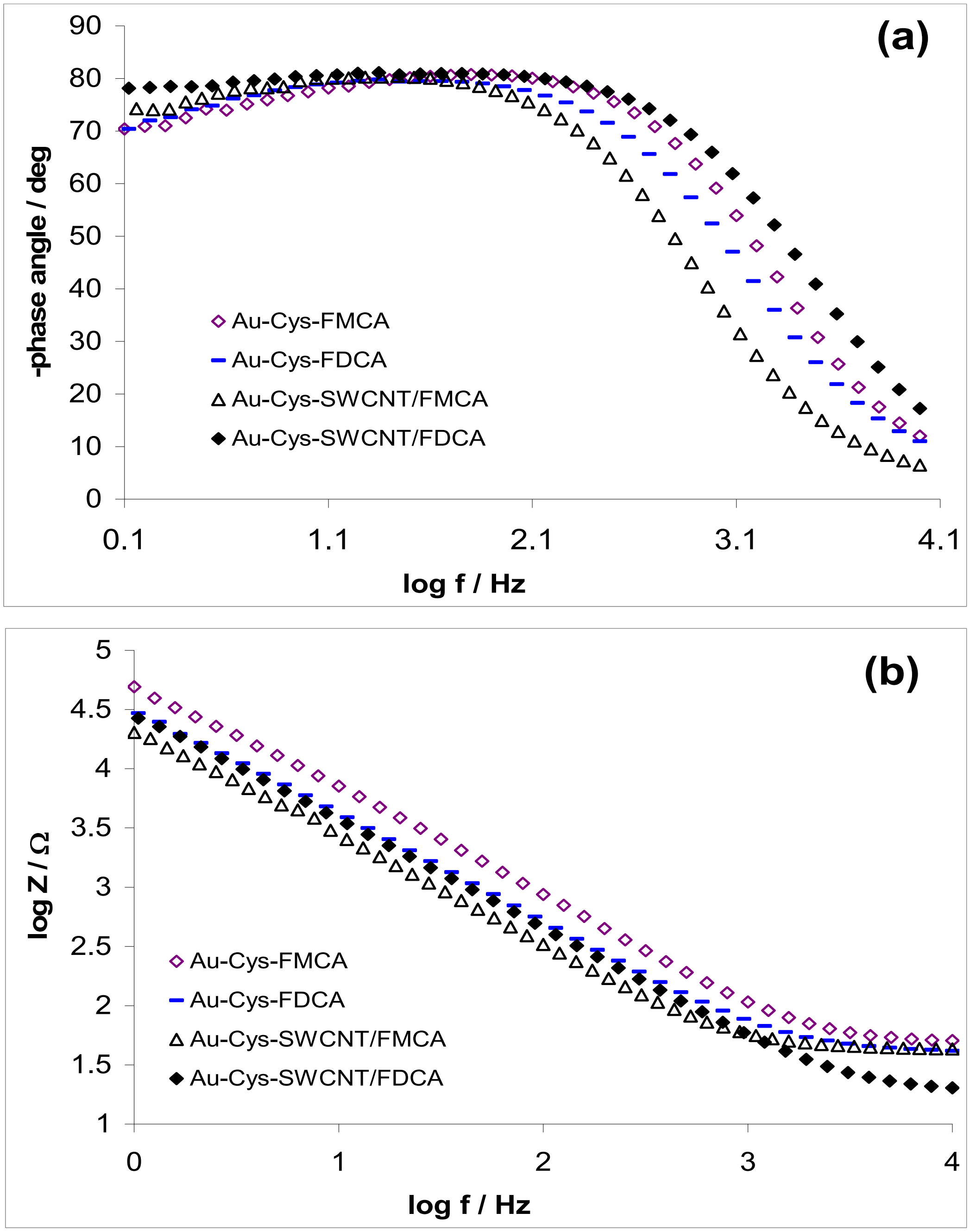

Figure 5.5: Bode plots, phase angle vs log f (a) and log Z vs log f (b),of the logarithm impedance spectra versus frequency of the modified electrodes in 0.5M H_2SO_4.

5.4 Electron transfer dynamics in a redox probe, $[Fe(CN)_6]^{4-}$ / $[Fe(CN)_6]^{3-}$

5.4.1 Cyclic voltammetric characterization

Electron transport properties of the electrodes were studied in PBS solution containing the outer-sphere redox probe, $[Fe(CN)_6]^{4-}$/ $[Fe(CN)_6]^{3-}$ (pH 7.2).

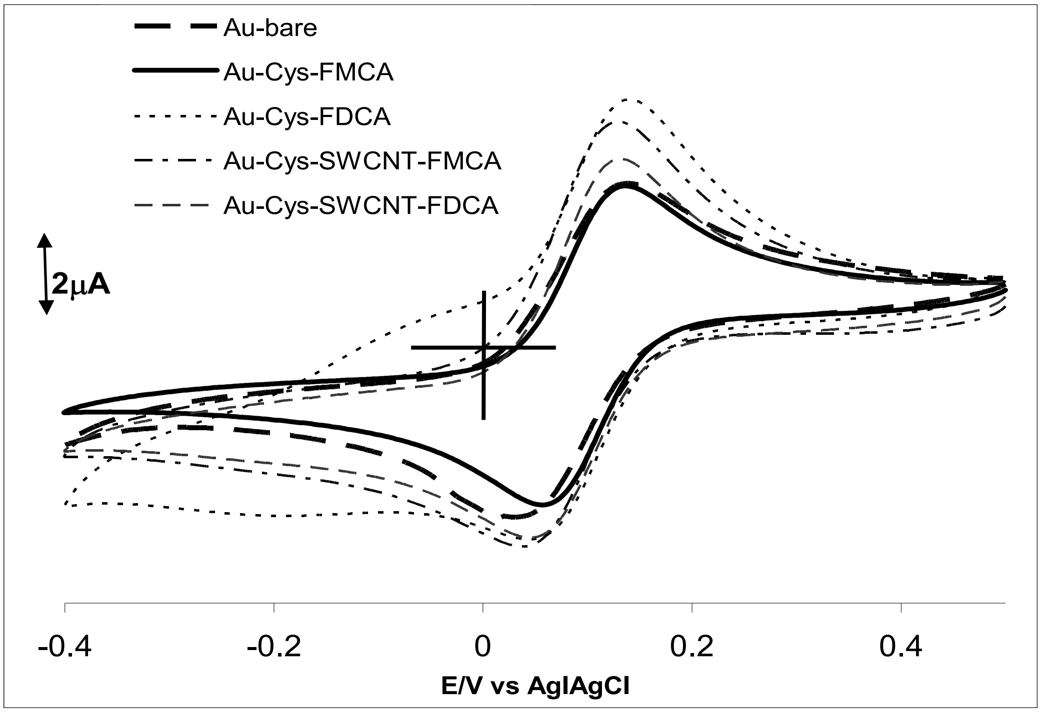

Figure 5.6: Comparative cyclic voltammetric evolutions of the bare and modified gold electrodes obtained in 0.1 M $[Fe(CN)_6]^{4-}$/$[Fe(CN)_6]^{3-}$ PBS, pH 7.2); bare Au, Au-Cys-FDCA, Au-Cys-FMCA, Au-Cys-SWCNT/FDCA and Au-Cys-SWCNT/FMCA. Scan rate = 25 mVs^{-1}.

Typical comparative cyclic voltammograms are exemplified in Figure 5.6. The ΔE_p value for all the electrodes are essentially the same (~ 110 mV) with same equilibrium potential ($E_{1/2} \approx 100$ mV).

5.4.2 Electrochemical impedimetric characterization

Since electrochemical impedance spectroscopy (EIS) provides a more detailed description of an electrochemical system [26] than cyclic voltammetry does, EIS was used to follow the electron transfer kinetics occurring at these electrodes. The EIS measurements were performed at the formal potential ($E_{1/2} \approx 100$ mV). Figure 5.7(a) shows examples of the Nyquist plots obtained for the electrodes in the $[Fe(CN)_6]^{4-}/[Fe(CN)_6]^{3-}$ solution (pH 7.2). The symbols in figure 5.7(a) represent the experimental data, while solid lines are the fitted curves fitted with the modified Randles equivalent circuit model (Figure 5.7(b)).

The EIS data together with the relative % errors is tabulated in Table 5.3 wherein the true capacitance is replaced by the constant phase element (CPE). In this model the R_s is the solution/electrolyte resistance, R_{ct} represents the electron-transfer resistance, while the Z_w is the Warburg impedance.

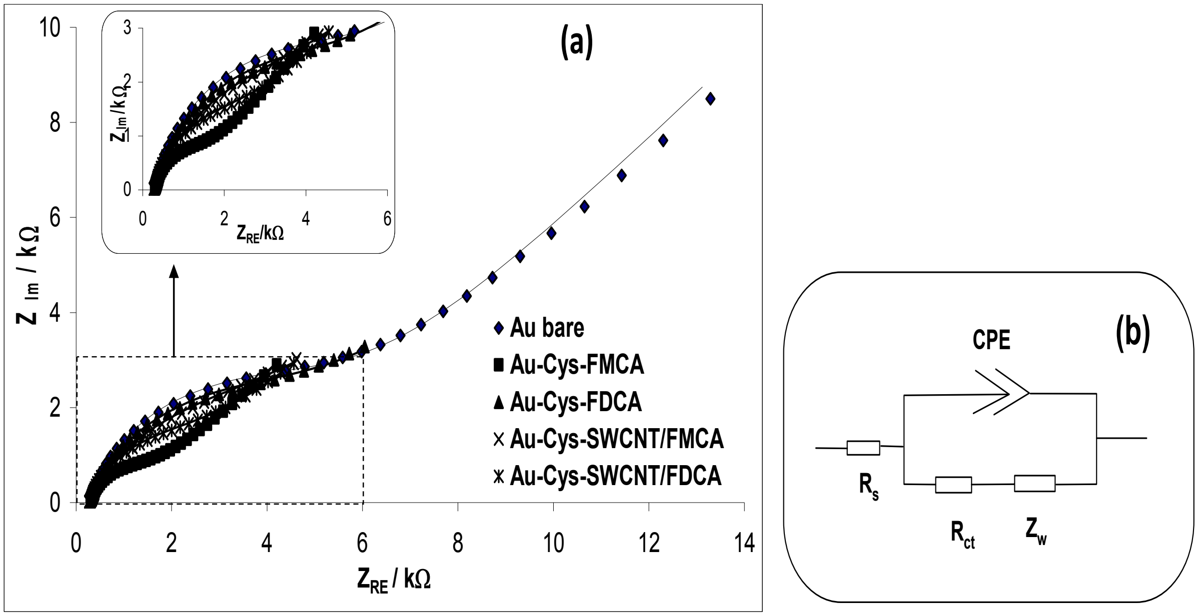

Figure 5.7: Nyquist plot (a) and the electrical equivalent circuit (b) used to fit the impedance spectra of bare Au and the modified electrodes obtained in 0.1 M $[Fe(CN)_6]^{4-}$/ $[Fe(CN)_6]^{3-}$ (PBS, pH 7.2).

The apparent electron transfer rate constant (k_{app}) of each of the electrodes was obtained from:

$$\mathbf{k}_{app} = \frac{RT}{n^2F^2AR_{ct}C} \qquad (5.4)$$

where n is the number of electron transfered (n=1), F is the Faraday constant, R is the ideal gas constant, T is the Kelvin temperature, A is the experimentally-determined area of the electrode, R_{ct} value is obtained from the fitted Nyquist plots, C is the concentration of the $[Fe(CN)_6]^{3-}$ (in mol cm^{-3}, the concentration of $[Fe(CN)_6]^{3-}$ and $[Fe(CN)_6]^{4-}$ are equal).

Table 5.3: Summary of estimated EIS parameters obtained in 0.1 M $[Fe(CN)_6]^{4-}$/ $[Fe(CN)_6]^{3-}$ (PBS, pH 7.0)

	Electrochemical impedance spectroscopic parameters[a]					
Electrodes	R_s /Ω	CPE /μF	n	Rct /kΩ	Z_W /μΩ	10^3 k_{app}/cm s^{-1}
Au	305.8(0.43)	5.32(2.02)	0.86(0.37)	5.12(1.15)	104.0(0.90)	1.93±0.02
Au-Cys-FMCA	300.9(0.40)	0.44(4.16)	0.86(0.58)	1.41(1.64)	98.3(0.68)	6.98±0.11
Au-Cys-FDCA	310.0(0.63)	0.63(5.56)	0.82(0.69)	4.93(3.03)	118.7(4.52)	2.00±0.06
Au-Cys-SWCNT/FMCA	271.7(0.53)	0.52(5.59)	0.76(0.68)	4.65(3.87)	126.6(4.67)	2.12±0.08
Au-Cys-SWCNT/FDCA	280.1(0.33)	0.98(3.22)	0.86(0.45)	2.58(1.83)	107.6(1.28)	3.82±0.07

[a] The value in brackets are the estimated error percentages.

From Table 5.3, the k_{app} values increases as follows: Au-Cys-FMCA > Au-Cys-SWCNT/FDCA > Au-Cys-SWCNT/FMCA ≈ Au-Cys-FDCA > bare Au. Within the limits of experimental errors, the trend in the electron transport kinetics seen in the redox probe ($[Fe(CN)_6]^{3-}$/$[Fe(CN)_6]^{4-}$ solution are somewhat comparable with those observed with the H_2SO_4 solution. However, we should not expect them to necessarily follow the same trend. This is because, first, the experiments were performed at different electrolyte conditions. Second, unlike the experiment in the H_2SO_4 that provides insight into the redox processes (Fe^{3+}/Fe^{2+}) of the electrode-confined ferrocene species, the experiment with the $[Fe(CN)_6]^{3-}$/$[Fe(CN)_6]^{4-}$ solution essentially interrogates the extent to which the immobilized ferrocene species permit the permeation of the redox probe and/or enhance faradaic response of the $[Fe(CN)_6]^{3-}$ and $[Fe(CN)_6]^{4-}$ species. The n values (Table 5.3) are in the range 0.76 and 0.86, indicative of pseudocapacitive behaviour. The values of the phase angles of less than 90° confirm the pseudocapacitive behaviour as well as the slopes of the log Z vs log f plot (*ca*. –0.57) as illustrated in figures 5.8(a) and 5.8(b), respectively. Figure 5.8(b) also illustrates high frequency which approximate high rate of reaction, thus this bode plot agrees with Table 5.3.

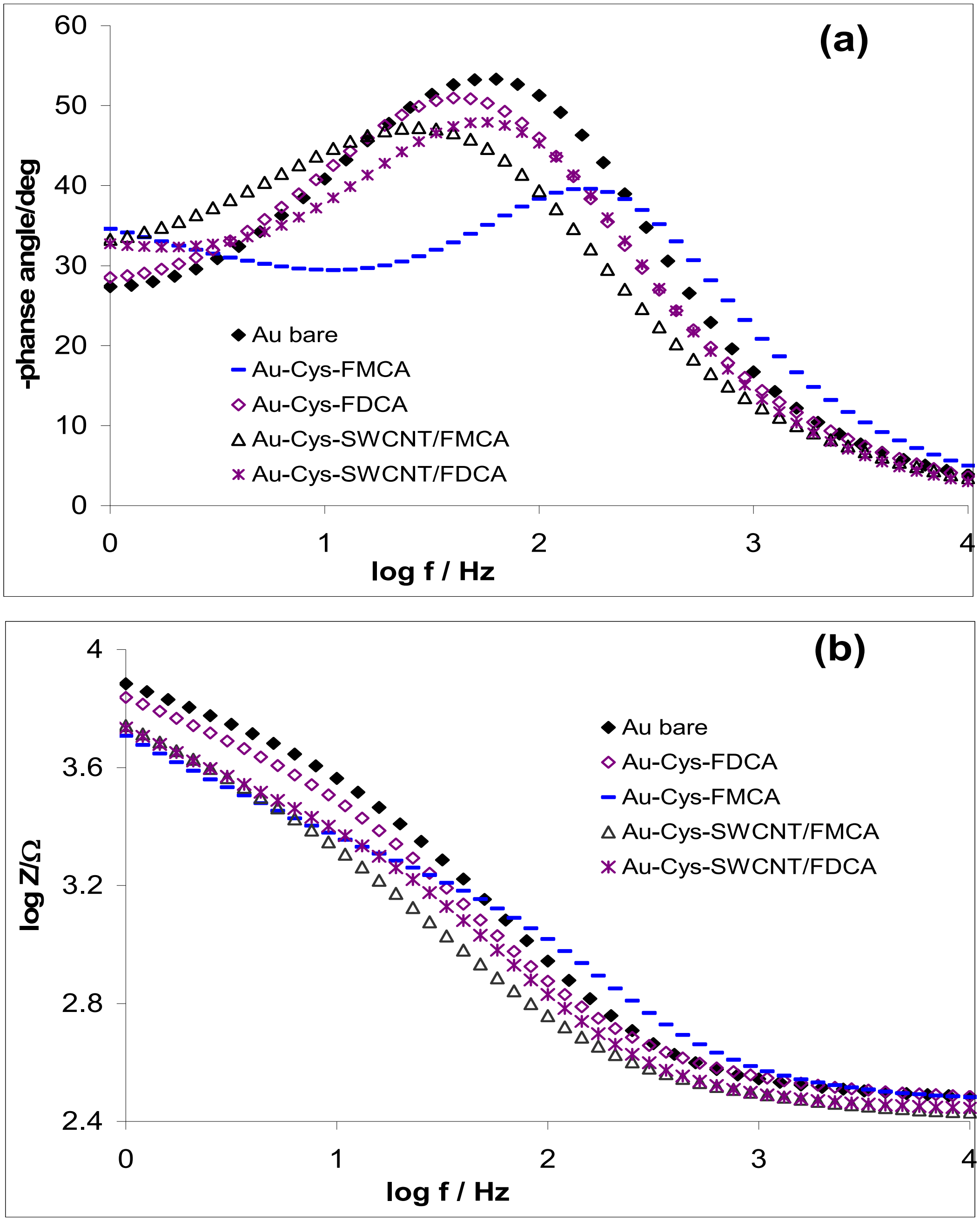

Figure 5.8: Bode plots, phase angle vs log f (a) and log Z vs log f (b) of the impedance spectra of the modified electrodes in redox probe ($[Fe(CN)_6]^{4-}/[Fe(CN)_6]^{3-}$) PBS solution (pH 7.2).

REFERENCES

1. J. Yu, J. G. Shapter, J. S. Quinton, M. R. Johnston and D. A. Beattie, Phys. Chem. Chem. Phys. 9 (2007) 510.
2. J. J. Gooding, R. Wibowo, J. Liu, W. Yang, D. Losic, S.Orbons, F.J. Meams, J.G. Shapter and D.B. Hibbert, *J. Am. Chem. Soc.*125 (2003) 9006.
3. J. J. Gooding, *Electrochim. Acta* 50 (2005) 3049.
4. J. J. Gooding, A. Chou, J. Liu, D. Losic, J. G. Shapter,; Hibbert, D. B. *Electrochem. Commun.* 9 (2007) 1677.
5. K. O. Ozoemena, T. Nyonkong *Electrochim. Acta* 47 (2002) 4035.
6. K. O. Ozoemena, T. Nyonkong, P. Westbroek, *Electroanalysis* 14 (2003) 1762.
7. H. O. Finklea, In: A. J. Bard, I. Rubinstein, (Eds.), *Electroanalytical Chemistry*, Marcel Dekker, New York, 19 (1996) 109.
8. H. O. Finklea, *J. Am. Chem. Soc.* 114 (1992) 3173.
9. H. O. Finklea, M. S. Ravenscroft, and D. A. Snider, *Langmuir* 9 (1993) 223.
10. B. S. Flavel, J. Yu, A. V. Ellis, J. G. Shapter, *Electrochim. Acta* 54 (2009) 3191.

11. G. K. Rowe, M. T. Carter, J. N. Richardson, and R. W. Murray, *Langmuir* 11 (1995) 1797.

12. S. Chen, R. W. Murray *J. Phys. Chem*. B 103 (1999) 9996.

13. S. Chen, *J. Phys. Chem. B*, 104 (2000) 663.

14. C. E. D. Chidsey, C. R. Bertozzi, T. M. Putvinski, A. M. Mujsce, *J. Am. Chem. Soc.* 112 (1990) 4301.

15. C. E. D. Chidsey, *Science* 251 (1991) 919.

16. R. W. Murray, In *Electroanalytical Chemistry*; Bard, A. J., Ed.; Marcel Dekker: New York, 13 (1984) 191.

17. R. C. Chambers, C. E. Inman, J. E. Hutchinson, *Langmuir* 21 (2005) 4615.

18. H. O. Finklea In *Electroanalytical Chemistry*; A. J. Bard, Ed.; Marcel Dekker: New York, Vol. 19 (1996) p 109.

19. S. E. Creager, T. T. Wooster, *Anal. Chem*. 70 (1998) 4257.

20. L. V. Protsailo, W. R. Fawcett, *Electrochim. Acta*. 45 (2000) 3497.

21. M. I. Prodromidis, *Electrochim. Acta*. doi:10.1016/j.electacta.2009.01.081 (2009).

22. N. S. Mathebula, J. Pillay, G. Toschi, J. A. Verschoor, K. I. Ozoemena, *Chem. Commun*. (2009)3345.

23. E. Barsoukov, J. R. Macdonald, *Impedance Spectroscopy: Theory Experiment, and Applications*; 2nd ed.; Wiley: Hoboken, New Jersey, 2005; chapters 1 – 4.

24. M. E. Orazem, B. Tribollet, *Electrochemical Impedance Spectroscopy*; John Wiley & Sons Inc: Hoboken, NJ. 2008; Chapter 13.

25. V. Ganesh, S.Pitchumani, V. Lakshminarayanan, *J. Power Sources* 158 (2006) 1523.

26. B. –Y. Chang, S. -Y.Hong, J. -S. Yoo and S. -M. Park, *J. Phys. Chem. B* 110 (2006) 19385.

CHAPTER 6

ELECTROCATALYTIC PROPERTIES OF FERROCENE SINGLE-WALLED CARBON NANOTUBES BASED ELECTRODES: THIOCYANATE AS A MODEL ANALYTE

6.1 Square wave voltammetric detection of SCN^-

Having established that the neighbouring SWCNTs impact on the electron transfer of the ferrocene molecular assemblies (chapter 5), it was necessary to establish the extent to which these SWCNTs could impact on the electrocatalytic behaviour of the ferrocenes. For this study, thiocyanate (SCN^-) was chosen as a model analyte. Figure 6.1 is a comparative square wave voltammetric (SWV) evolutions obtained at constant concentration (1 mM) of SCN^- at the various electrodes in PBS (pH 4.8). This pH condition was chosen for this experiment as it is well known for enhanced detection of SCN^- [1-2]. The catalytic behaviour (in terms of onset potential) follows this trend: Bare Au (0.64 V) > Au-Cys-SWCNT (0.62 V) > Au-Cys-FMCA ≈ Au-Cys-FDCA (0.48 V) > Au-Cys-SWCNT/FMCA (0.50 V) > Au-Cys-SWCNT/FDCA (0.42 V).

The Au-Cys-SWCNT/FDCA and Au-Cys-SWCNT/FMCA gave the highest current response with less positive onset potential (0.3 V) compared to other electrodes. However, Au-Cys-SWCNT/FDCA recorded the least peak potential for the oxidation of SCN^- at 0.48 V, possibly due to the repulsive interaction between the negatively charged SCN^- and high number of surface –COOH species at the FDCA.

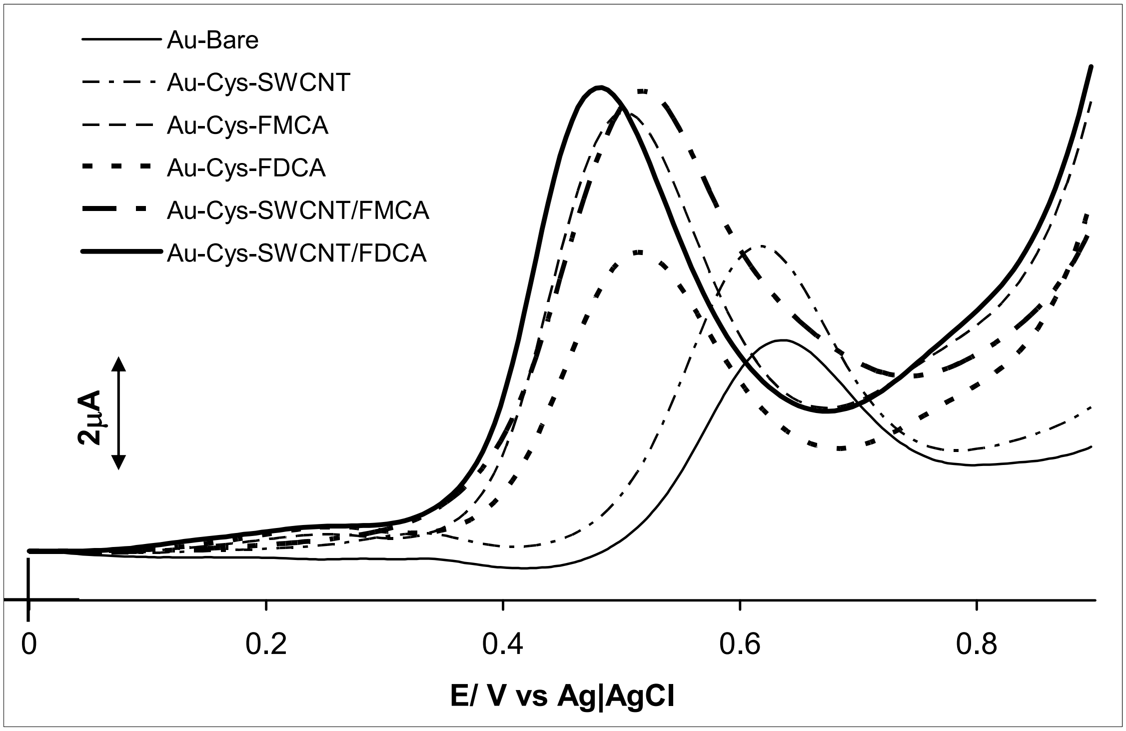

Figure 6.1: Comparative square wave voltammograms of the bare gold and modified gold electrodes obtained in PBS solution (pH 4.7) containing 1 mM SCN$^-$.

Second, the ferrocene-based electrode without the SWCNTs (i.e., Au-Cys-FDCA and Au-Cys-FMCA) exhibited more positive onset potential (~ 0.35 V) for the oxidation of SCN$^-$ compared to the ones containing SWCNTs (Au-Cys-SWCNT/FDCA and Au-Cys-SWCNT/FMCA) at 0.3 V. This improved response towards the detection of SCN- species is due to the combined synergistic activities of good electrocatalysts (FCDA or FMCA) and the efficient electronic conducting nanowires (SWCNTs). This finding is quite remarkable especially when compared to data previously obtained at the FePc and SWCNT-FeOHETPc SAM modified electrodes where the oxidation of SCN^- occurred at peak potentials ≥ 0.60 V [2]. Also, the current responses recorded in this present work for the Au-Cys-SWCNT/FDCA and Au-Cys-SWCNT/FMCA for the same concentration of SCN^- (1 mM) is approximately twice than reported for the FeOHETPc and FePc-SAM modified electrodes [2].

6.2 Influence of scan rates on electrocatalysis of SCN^-

Oxidation of SCN^- using cyclic voltammetric experiments were carried out with a view to establishing the impact of scan rates (ν) at constant concentration (1 mM) of the SCN^-. The study was carried out with Au-Cys-SWCNT/FDCA electrodes as illustrated in figure 6.2. The increase in the peak current was observed with increasing scan rates (scan rates ranging 25 - 900 mV/s). Also, a broad reduction peak (in the 0.1 to 0.5 V regions) appeared only at higher scan rates, > 100 mVs^{-1}. A similar behaviour of the electrode was observed for the electrode modified with FeOHETPc as discussed in chapter 4. The insert in figure 6.2 indicate a plot of I_p vs ν, which is not linear proving that neither the oxidized SCN^- nor its intermediate product(s) adsorbed on the modified electrode.

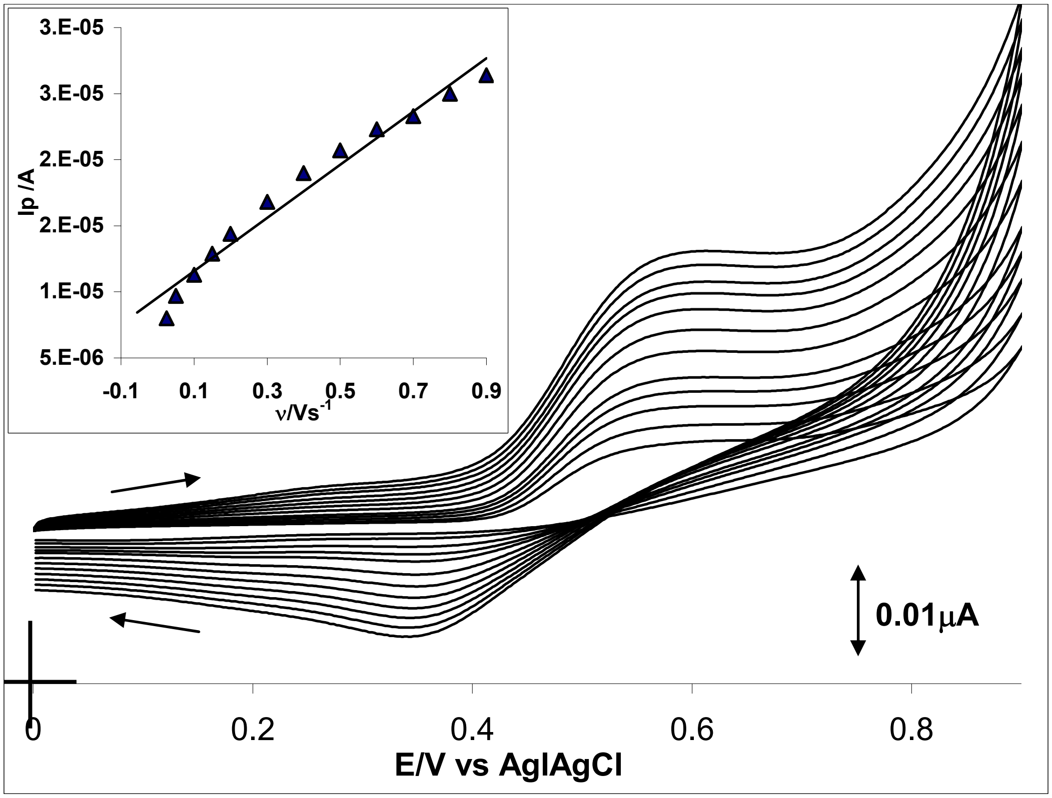

Figure 6.2: Cyclic voltammetric evolutions at varying scan rates and insert is the plot of current (I_p) versus scan rate (ν) ranging from 25 to 900 mVs^{-1}. [SCN$^-$] = 1 mM

Figure 6.3(a) illustrates the relationship between peak current (I_p) with the square root of scan rate ($\nu^{1/2}$) of the SCN$^-$ oxidation which gave a linear relationship (R^2 = 0.9989), indicating a diffusion-controlled reaction. Tafel plot (see equation 4.1) is given in figure 6.3(b) where two slopes can be seen [3]. The first slope for lower potential, i.e between 555 and 578 mV vs AgIAgCl leads to a value of 30 mV / decade and the second slope for higher potential between 600 and 620 mV which lead to a value of 66 mV / decade. This is an indication of the two mechanisms that are involved as a function of potential for Au-Cys-SWCNT/FDCA electrode.

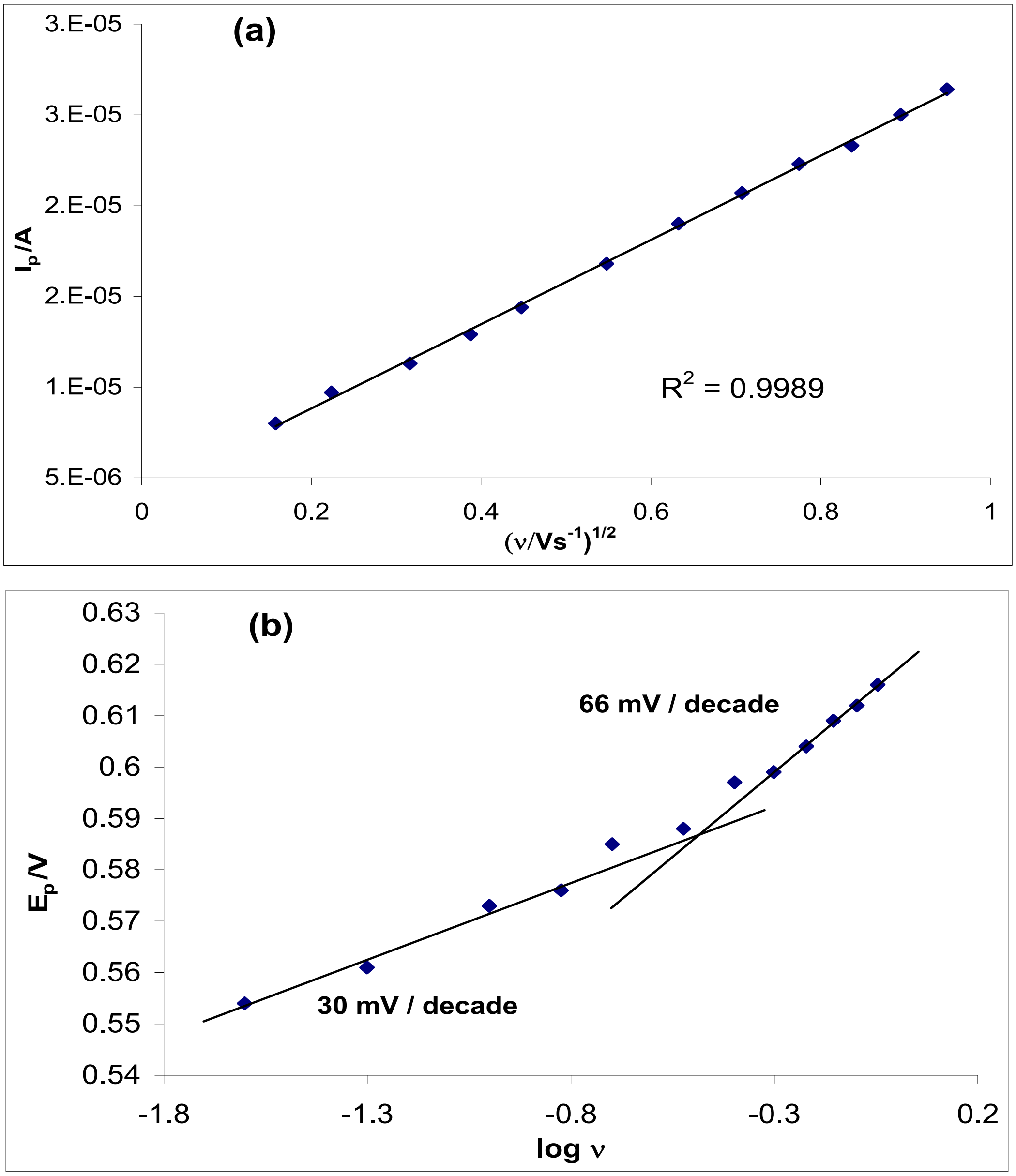

Figure 6.3: The plots of (a) peak current against the square root of the scan rate and (b) peak potential against log of scan rate for the Au-Cys-SWCNT/FDCA electrode in 1 mM SCN$^-$.

6.3 Rotating gold disk electrode experiments

The rotating disk electrode (RDE) voltammetric evolutions of constant concentration (1 mM SCN^-) at different rotating speed of the electrodes are shown in Figure 6.4. The Koutecky-Levich plot (Figure 6.4 inset) was obtained from the conventional Koutecky-Levich theory. The numbers 1 to 12 in the figure correspond to 250, 500, 750, 1000, 1250, 1500, 1750, 2000, 2250, 2500, 2750 and 3000 rpm, respectively.

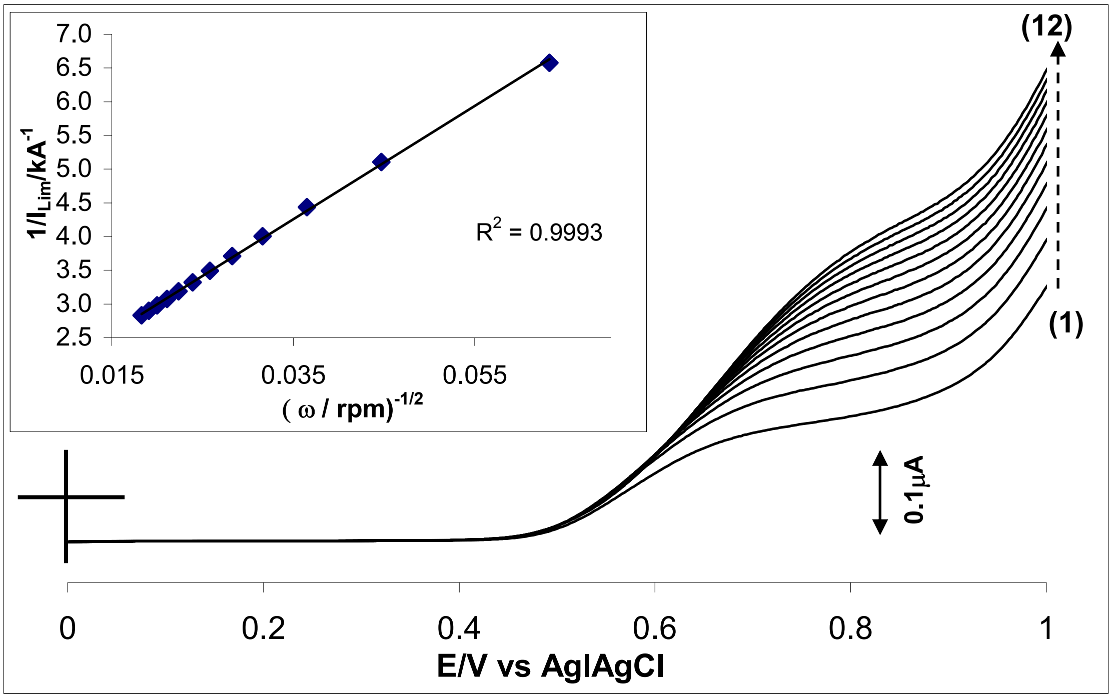

Figure 6.4: Linear sweep voltammetric evolutic evolutions of the rotating disk electrode experiments obtained at Au-Cys-SWCNT/FDCA in PBS solution (pH 4.8) containing 1 mM SCN^- at 50 mVs^{-1}. (Inset is Koutecky-Levich plot).

The results showed that the catalytic current increased linearly with increasing $\omega^{-1/2}$ with a positive intercept, indicating that the electrode reactions were controlled by both kinetics and the mass transport of SCN^- species at the electrode surfaces. From the intercept and the slope of the plot, the diffusion coefficient value of *ca*.1.10 x 10^{-5} cm^2s^{-1} was obtained. This value is of same magnitude as the phthalocyanine based electrode (chapter 4) with similar experimental conditions. The surface coverage of the Au-Cys-SWCNT/FDCA electrode was calculated as 1.4 x 10^{-9} mol cm^{-2} (see table 4.1). This value suggests that the material on the gold electrode is not a monolayer which confirms the conclusion made in chapter 4 that it is possible that the high surface coverages obtained in our experiments could be due to the long exposure time of cysteamine to gold electrode leading to more binding sites for the ferrocenes. Using the Koutečky-Levich equation, the k value was obtained *ca*. 2.0 x 10^{-2} cm^3 mol s^{-1}.

6.4 Chronoamperometric investigations

A well resolved double-step chronoamperometric evolutions obtained at the Au-Cys-SWCNT/FDCA electrode in the absence (buffer alone) and presence of consecutive addition of 32.3 µM thiocyanate in phosphate buffer solution (pH 4.8) is shown in figure 6.5. The figure illustrates the double potential step chronoamperometric experiments recorded by polarizing the working electrode potentials to 0.62 and 0.20 V. It shows that at the conditions employed for this work, the SCN^- was irreversible. Figure 6.5 (inset) depicts linearity with slope of 7474.3 between I_p versus $[SCN^-]$. The linear concentration range of up to 0.21 mM was obtained for the Au-Cys-SWCT/FDCA electrode with a sensitivity of ca. 7.5×10^{-3} AM^{-1}, and limit of detection ~ 28 µM (LoD = 3.3 s/m [4], where s is the relative standard deviation of the intercept and m the slope of the linear peak current vs the concentration of SCN^-). The Cottrell equation (Equation 6.1) was used to determine both diffusion coefficient (D) and catalytic rate constant of SCN^- from the chronoamperometric data.

$$I = \frac{nFAD^{1/2}C}{\pi^{1/2}t^{1/2}} \qquad (6.1)$$

where n = number of electrons involved in the reaction, F is the Faraday constant F (96485 C mol^{-1}), and A is the experimentally determined area of the electrode, C is the bulk concentration of the thiocyanate (mol/L)), while t is time (s).

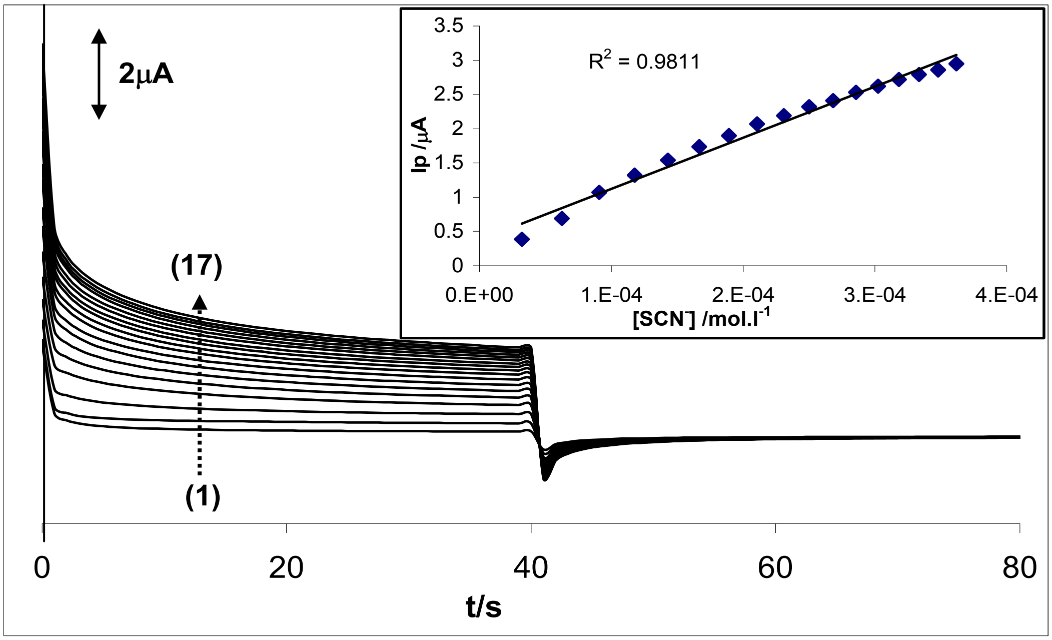

Figure 6.5: Typical double potential step chronoamperometric transients at Au-Cys-SWCNT/FDCA in PBS solution (pH 4.8) following addition of SCN⁻ Inset is the plot of chronoamperometric current at t = 10 sec vs [SCN⁻].

Figure 6.6 shows the linear plots of I_p vs $t^{-1/2}$ at different thiocyanate concentrations, and from the plot of slopes vs [SCN⁻], and taking n = 2, the D value for SCN⁻ was estimated to be *ca.* 10.4 x 10^{-10} cm^2s^{-1}, which is lower than that obtained for the FeOHETPc based electrode (~ 10^{-6} cm^2s^{-1}). Despite this low D value, the catalytic properties of ferrocene based electrode is still more enhanced than that of the FePc. The catalytic rate constant for the oxidation of SCN^- was also estimated from the chronoamperometry experiments using the relationship [5,6] (Equation 6.2):

$$\frac{I_{cat}}{I_{buff}} = \pi^{\frac{1}{2}}(kCt)^{\frac{1}{2}} \qquad (6.2)$$

where I_{cat} and I_{buff} are the currents in the presence and absence of thiocyanate, respectively; k is the catalytic rate constant and t is the time in seconds. From the plots of I_{cat}/I_{buff} vs $t^{1/2}$ at different thiocyanate concentrations (Figure 6.7), and a plot of the slopes vs $[SCN^-]$, k was estimated as 1.26×10^4 cm^3 mol s^{-1}.

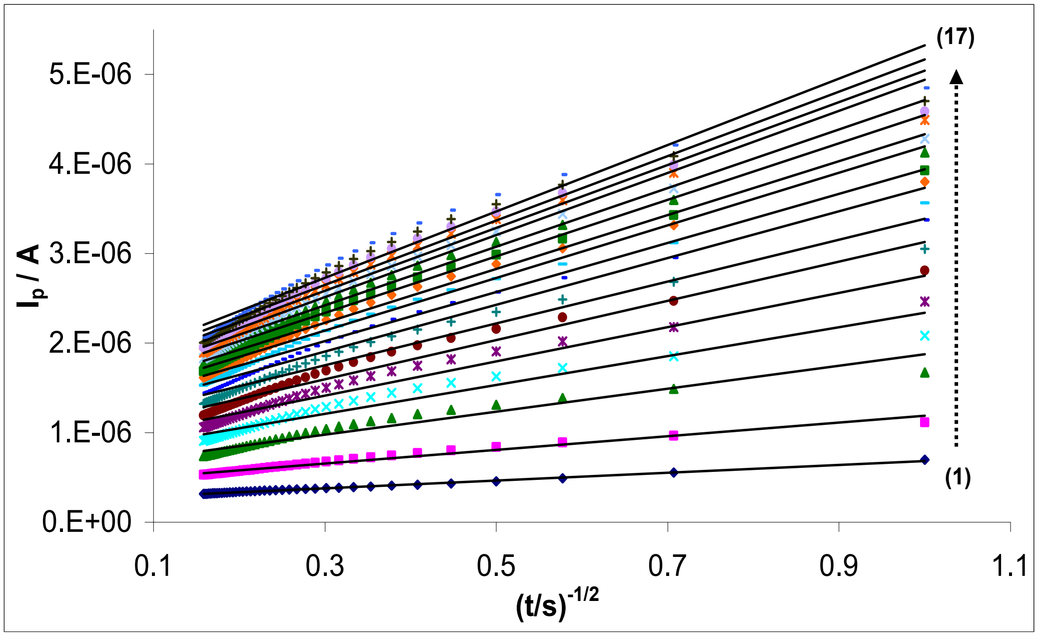

Figure 6.6: Typical Cottrell equation plots obtained from the chronoamperometric evolution at Au-Cys-SWCNT/FDCA in PBS solution (pH 4.7) following addition of SCN^-.

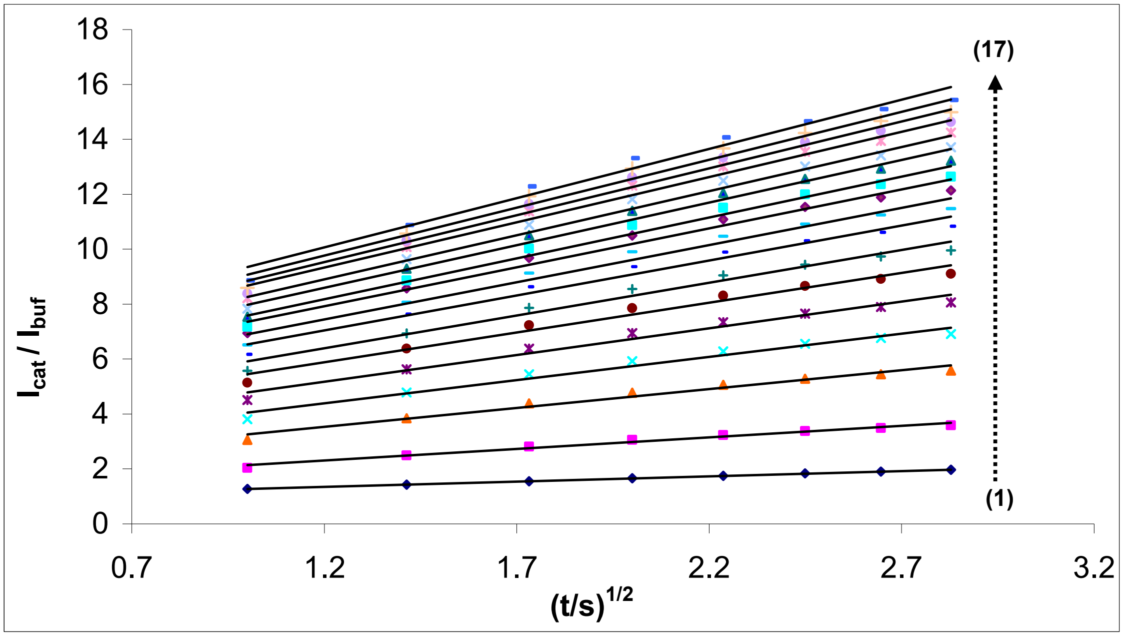

Figure 6.7: Plots of I_{cat}/I_{buff} vs $t^{1/2}$ obtained from the chronoamperometric evolution at Au-Cys-SWCNT/FDCA in PBS solution (pH 4.7) following addition of SCN^-.

6.5 Gold nanoparticle-modified indium tin oxide electrode experiment

The suitability of the ITO-nanoAu-Cys-SWCNT/FDCA for a possible application as a disposable, one-shot electrode system for a quick chronoamperometric detection of SCN$^-$ was also tested (Figure 6.8). With this electrode, a chronoamperometric sensitivity of 7.3 x10^{-3} and a limit of detection of ~13 nM for the SCN^{-1} were obtained. The values are comparable to the data obtained at the modified bulk gold electrode.

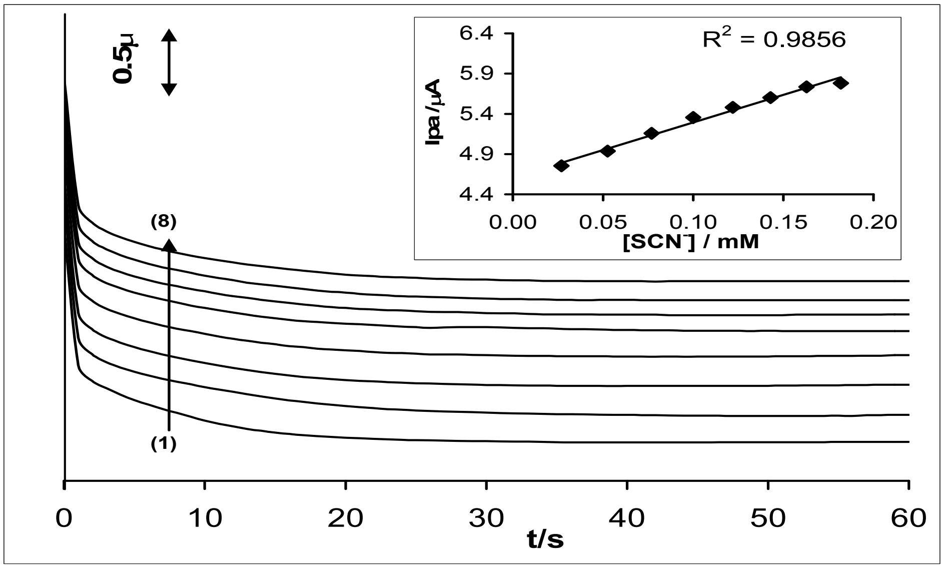

Figure 6.8: Chronoamperometric evolutions at ITO-nanoAu-Cys-SWCNT/FDCA electrode in PBS solution pH 4.7 containing 1mM SCN$^-$. **inset**: Plot of peak current vs concentration obtained from chronoamperometric evolutions for the ITO-nanoAu-Cys-SWCNT/FDCA electrode.

REFERENCES

1. S. Adak, A. Mazumdar, R. K.Banerjee, *J. Biol. Chem.* 272 (1997) 11049.
2. K. I. Ozoemena, T. Nyokong, *J. Electroanal. Chem.* 579 (2005) 283.
3. S. Baranton, C. Coutanceau, E. Garnier and J. –M. Leger, *J. Electroanal. Chem.* 590 (2006) 100.
4. G. D. Christian, Analytical Chemistry, 6th ed. John Wiley and Sons, New York, 2004, p.113.
5. M. H. Pournaghi-Azar, R. Sabzi, *J. Electroanal. Chem.* 543(2003) 115.
6. K. M. Manesh, P. Santosh, A. I. Gopalan, K. -P. Lee, *Electroanalysis* 18 (2006) 894.

CONCLUSIONS AND FUTURE PERSPECTIVE

The remarkable electrochemical and electrocatalytic activities of the studied organometallic complexes (FePc and Fc complexes) has been described in this work. The construction by sequential self-assembly process of a reproducible and stable redox-active nanostructured arrays of single-walled carbon nanotube (SWCNT) coordinated to organometallic complexes on a gold surface was successfully developed.

A number or remarkable findings in this work should be emphasized; first, this represents the first report on the coordination by self-assembly of a redox-active iron phthalocyanine complex to surface-confined SWCNT via ester bond formation. Second, the redox properties of the SAMs exhibit strong dependence on the reaction of the head groups and the pH of the working electrolytes. Third, Au-Cys-SWCNT-FeOHETPc electrode showed much faster electron transfer kinetics compared to the Au-Cys-SWCNT-CoTAPc electrode. Fourthly, the high electron transfer capability of the Au-Cys-SWCNT-FeOHETPc electrode over the Au-Cys-SWCNT or the Au-Cys-FeOHETPc or the Au-FeOHETPc electrodes confirms that SWCNT greatly improves the electronic communication between FeOHETPc and the bare gold electrode. Finally, our results clearly showed that aligned SWCNT-FeOHETPc arrays exhibit much faster electron transfer kinetics to redox-active species in solutions compared to the randomly dispersed (drop-dried) SWCNT electrode. The advantageous electron transfer properties of the Au-Cys-SWCNT-FeOHETPc electrode, coupled with its ease of fabrication and chemical stability, could be found useful in electrochemical sensing and catalysis, and such possibilities would form the main subjects of future studies. These findings could also apply to iron phthalocyanine related complexes, notably the iron porphyrins and Schiff bases. This implies the impact of peripheral substituents has on the phthalocyanine core towards electrocatalytic behaviour.

The electrocatalytic activity of a coordination self-assembled SWCNT-FeOHETPc hybrid on gold electrode show that this hybrid exhibit greater senstivity towards the detection of thiocyanate compared to electrodes containing SWCNT or FeTAPc or FeOHETPc only, confirming the ability of the SWCNTs to function as effective conductive nanowires.

Cyclic voltammetric and impedance spectroscopic characteristics of the redox-active SAMs revealed reversible electrochemistry in aqueous solutions with different electron-transfer rates. Preliminary electrocatalytic investigation proved that both SAMs exhibit comparable electrocatalytic responses towards the detection of dopamine in pH 7.4 PBS. This proposed electrode fabrication technique is unique; it can be used for fundamental studies of the electron transfer processes of surface confined metalloporphyrin and metallophthalocyanimne complexes and, importantly, it promises to provide an opportunity for controlled fabrication of stable organometallic sensing platforms. For example, further studies to explore other electrocatalytic properties (e.g., influence of surface charges to electron transfer) and sensing capabilities of this type of MPc-SAM to organic analytes will constitute the some of the subjects of future investigations.

The electrochemistry of electron transfer dynamics of ferrocene-terminated self-assembled monolayers (SAMs), co-adsorbed with SWCNTs on gold electrode, have been interrogated for the first time. Factors influencing electron transport within organized molecular assemblies are crucial for the potential applications of such platforms in many areas such as in molecular electronics, chemical and biological sensings. The important findings in this work should be emphasized. First, the neighbouring SWCNTs in the ferrocene molecular assemblies exert distinct impacts on the global electron transport and electroacatalytic behaviour of the ferrocenes. Second, that the presence of SWCNTs in the ferrocene assembly synergistically enhances the electrocatalytic detection of thiocyanate compared to the ferrocene or SWCNTs alone. In a nutshell, this work has provided some useful physical insights into the impact of local SWCNTs microenvironment surrounding a redox-active and electocatalytic molecule (not only ferrocene but other related organometallic species) on the dynamics of electron transport between solution species and electrode. We envisage that these insights have provided some thoughts on the factors that must be considered when designing molecular-scale electronics or electrocatalytic devices that employ CNT and ferrocenes (or related species). Future work on these newly developed findings should include the application as electrocatalysts for sensing biological molecules such as dopamine and epinephrine.

APPENDIX A

Publications in peer-reviewed journals form this Thesis

1. **D. Nkosi**, K. I. Ozoemena, "Self-assembled nano-arrays of single-walled carbon nanotubes octa(hydroxyethylthio) phthalocyaninatoiron(II) on gold surfaces: Impacts of SWCNT and solution pH on electron transfer kinetics" *Electrochim. Acta,* 53, 2008, 2782-2793.

2. **D. Nkosi**, K. I. Ozoemena, "Interrogating the electrocatalytic properties of coordination self-assembled nanostructures of single-walled carbon nanotube–octa(hydroxyethylthio) phthalocyaninatoiron(II) using thiocyanate as an analytical probe" *J. Electroanal. chem.*, 621,2008,304-313.

3. K.I. Ozoemena, **D. Nkosi**, J. Pillay, "Influence of solution pH on the electron transport of the self-assembled nanoarrays of single-walled carbon nanotube-Cobalt tetraaminophthalocyanine on gold electrodes: Electrocatalytic detection of epinephrine" *Electrochim. Acta,* 53, 2008, 2844-2851.

4. K.I. Ozoemena, T. Nyokong, **D. Nkosi**, I. Chambrier, and M.J. Cook, "Insights into the Surface and Redox Properties of Single-Walled Carbon Nanotube–Cobalt(II) tetra-aminophthalocyanine Self-Assembled on Gold Electrode", *Electrochim. Acta* 2007, 52, 4132-4143.

5. **D. Nkosi**, J. Pillay, K. I. Ozoemena, K. Nouneh, M. Oyama, Heterogeneous electron transfer kinetics and electrocatalytic behaviour of mixed self-assembled ferrocenes and SWCNTs layers Phys. Chem. Chem. Phys. 2010, 12, 604-613.

APPENDIX B

List of Conference Presentations from this Thesis

1. *"Self-Assembled Nanostructures of Iron-Phthalocyanines and Mixed Monolayers of Single-Walled Carbon Nanotubes."* **Duduzile Nkosi** and Kenneth I. Ozoemena CSIR International Convention Centre, Pretoria, South Africa february 1-4, 2009 (Oral presentation)

2. *"Electrochemical Activity of Self-Assembled Mixed Monolayers of Single-Walled Carbon Nanotubes and Ferrocenes on Gold Electrode".* **Duduzile Nkosi** and Kenneth I. Ozoemena, Nanometerial Conference, Playa del Carmen, Cancun, Mexico, December 3-8, 2008 (poster presentation)

3. *"Catalytic Activities of Self-Assembled Nanostructures of Iron-phthalocyanines and Ferrocene-Single-Walled Carbon Nanotubes"* **Duduzile Nkosi** and Kenneth I. Ozoemena, ECSA, 1st international symposium on electrochemistry, Bellville, Cape Town, July 8-11, 2008. (Oral presentation)

4. *"Self-Assembled Nanostructures of Iron- Phthalocyanines and Ferrocenes as Sensing platforms"* **Dudu Nkosi** and Kenneth I. Ozoemena International (SA-UK Research Network) workshop on electrochemistry for nanothechnology, CSIR, Pretoria, April 9-10, 2008. (Oral presentation)

5. *"Electron transfer at Gold Electrodes Modified with Self-Assembled Monolayers of Carbon Nanotube-Iron Phthalocyanine Complex"*, **Dudu Nkosi** and Kenneth I. Ozoemena, 38th Convention of the South African Chemical Institute, Durban, SOUTH AFRICA, December 3-8, 2006. (Award winning poster presented by D. Nkosi)